Développement de Revêtements Radiopaques Biohydroxyapatite / Bioglass Déposés par Projection Thermique pour des Applications Biomédicales

Germán Andrés Clavijo Mejía

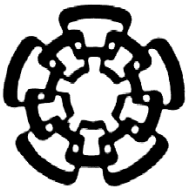

CENTRO DE INVESTIGACIÓN Y DE ESTUDIOS AVANZADOS DEL INSTITUTO POLITÉCNICO NACIONAL

THESIS IN JOINT-SUPERVISION
with

CENTRO DE INVESTIGACIÓN Y DE ESTUDIOS AVANZADOS DEL I.P.N
UNIDAD QUERÉTARO
PhD school in Sciences Materials Specialty
Thesis director: Juan MUÑOZ SALDAÑA

and

UNIVERSITY OF LIMOGES
PhD school of Materials, Mechanics and Energetics (ED 609)
Thesis co-director: Hélène AGEORGES

presented by

Germán Andrés CLAVIJO MEJÍA
in fulfillment of the requirements for the degrees of

DOCTOR OF PHILOSOPHY
in:
Sciences Materials Specialty
and
DOCTOR OF PHILOSOPHY
in:
Sciences and Engineer of Materials Mechanics and Energetics

DEVELOPMENT OF RADIOPAQUE BIOHYDROXYAPATITE/BIOGLASS COATINGS DEPOSITED BY THERMAL SPRAY FOR BIOMEDICAL APPLICATIONS

Santiago de Querétaro, Qro. December 2019

TABLE OF CONTENTS

LIST OF FIGURES AND TABLES

FIGURES

Chapter 2

Chapter 3

Chapter 4

TABLES

Chapter 2

Chapter 3

Chapter 4

ABSTRACT

Hydroxyapatite (HAp) and bioactive glass (BG45S5) are widely employed as precursors of thermally sprayed coatings to enhance the biocompatibility of biomedical implants. This, due to the similar structure of HAp with the bone tissue and the high reactivity of BG with biological media allowing the rapid bone tissue ingrowth on its surface. The combined deposition of both materials leads to build-up highly bioactive coatings with proper stability in comparison with single coatings. Furthermore, the HAp bioactivity and the BG45S5 radiopacity can be improved by obtaining the first from natural sources, as bovine-derived HAp (BHAp), and the second through the addition of radio-opacifiers as Bi_2O_3 to the BG structure. Consequently, coatings with augmented both, biocompatibility and x-rays opacity that allow improving the bioactivity and facilitate the use of non-invasive diagnostic methods, can be achieved.

This research presents the development of biocompatible and opacified thick coatings deposited by High-Velocity Oxygen Fuel (HVOF) and Atmospheric Plasma Spray (APS) techniques. The chemical composition, structure, and microstructure of radiopaque BHAp/BG45S5+Bi_2O_3 coatings were studied, as well as the properties of raw materials were also analyzed. Afterward, the bioactivity of several coatings' architecture, i.e., monolayers, graded, and multilayers, were assessed. The experimental results show that BHAp feedstock powder is mainly carbonated B-type apatite with a high purity HAp phase. The lab-made BG45S5 powders exhibit the chemical composition and physical properties with a substantial similarity compared to commercial BG45S5. The weight percent of 1 up to 20 of Bi_2O_3 was added to the bioactive glass to modify its radiopacity. Radiographic images of BG45S5+Bi_2O_3 show that 10 wt.% of the opacified material allows increasing the opacity of the BG mixture homogeneously by 3.6 times with no considerable effects on its structural and thermal properties. Regarding the thermally sprayed coatings, CO_3^{2-} and the Mg contents on BHAp lead to the formation of dolomite in the crystalline phase of the surface of single HVOF BHAp coating. Single BHAp APS coating does not exhibit any secondary phases in its surface crystalline content. A typical apatite layer is evidenced after 3 days of immersion in simulated body fluid (SBF) in the surface of both coatings and single BHAp HVOF coating show delamination after 5 days of immersion. Thus, APS was chosen to spray and analyze single BG45S5, BG45S5+10 wt.% Bi_2O_3 and gradual BHAp/BG45S5+10 wt.% Bi_2O_3 coatings. Single BG45S5+10 wt.% Bi_2O_3 coating shows similar microstructure and amorphous structure in comparison with the plasma-sprayed single coating using commercial BG45S5 feedstock powder without Bi_2O_3. However, delamination and a reduced rate of apatite layer formation are observed. Graded BHAp/BG45S5+10 wt. %

Bi_2O_3 coating shows a similar rate of apatite layer growth compared to single BG45S5+10 wt. % Bi_2O_3 coating. Nevertheless, the apatite formation after 10 days of immersion in SBF and no delamination are observed on the surface of the coating due to the graded deposition of BG45S5+10 wt. % Bi_2O_3 combined with BHAp.

RÉSUMÉ

L'hydroxyapatite (HAp) et le verre bioactif (BG) 45S5 sont largement utilisés comme précurseurs des revêtements fabriqués par projection thermique pour améliorer la biocompatibilité des implants biomédicaux. Ceci, en raison de la structure similaire de l'HAp avec le tissu osseux et la haute réactivité de ce BG en milieu biologique, ce qui permet la croissance rapide du tissu osseux à sa surface. La projection combinée des deux matériaux permet d'obtenirdes revêtements hautement bioactifs et stables par rapport aux revêtements individuels. De plus, la bioactivité de l'HAp et la radio-opacité de BG45S5 peuvent être améliorées en utilisant comme matières premières des sources naturelles, telles que l'HAp issue d'os de bovins (BHAp) et en ajoutant des radiopacifiants tels que l'oxyde de bismuth (Bi_2O_3) à la structure du BG. Par conséquent, des revêtements combinés avec une bioactivité et une opacité accrues vis-à-vis des rayons X peuvent être obtenus pour améliorer le diagnostic non invasif par radiographie des implants biomédicaux revêtus.

Cette recherche présente le développement de couches épaisses biocompatibles et opacifiées réalisées par projection thermique, flamme haute vitesse (High-Velocity Oxygen Fuel, HVOF) et plasma (Atmospheric Plasma Spray, APS). La composition chimique, la structure, la microstructure et la bioactivité des couches radio-opaques de BHAp/BG45S5+Bi_2O_3 obtenues sont étudiées ainsi que les propriétés des matériaux de départ. ainsi que la projection gradient du revêtement combiné. En particulier, la bioactivité de différentes architectures de revêtements (monocouches, couches à gradient de matériaux et multicouches) a été évaluée. Les résultats expérimentaux montrent que la poudre de départ de BHAp est principalement constituée d'apatite carbonée de type B avec une pureté élevée de la phase HAp. Les poudres de bioverre BG45S5 fabriquées en laboratoire présentent une composition chimique et des propriétés physiques très similaires à celles du BG45S5 commercial.Un pourcentage en poids de 1 à 20 % d'oxyde de bismuth Bi_2O_3 a été ajouté au verre bioactif pour modifier sa radio-opacité. Les images radiographiques des composés BG45S5 + x% Bi_2O_3 montrent que le bioverre avec 10% en poids d'oxyde de bismuth permet d'augmenter de 3,6 fois l'opacité du bioverre de manière homogène sans affecter de manière notable ses propriétés structurales et thermiques. En ce qui concerne les revêtements réalisés par projection thermique, la teneur en CO_3^{2-} et en Mg dans la poudre de BHAp conduit à la formation de dolomite dans la phase cristalline de la surface du revêtement monocouche de BHAp réalisé par HVOF alors que celui réalisé par APS ne montre aucune phase secondaire cristalline à sa surface. Une couche d'apatite typique est mise en évidence à la surface des deux revêtements après 3 jours d'immersion dans

un fluide corporel simulé (SBF), cependantle revêtement monocouche de BHAp réalisé par HVOF montre une délamination après 5 jours d'immersion. Par conséquent, la projection plasma APS a été choisie pour élaborer les revêtements monocouches de BHAp, BG45S5, BG45S5+10wt.% Bi_2O_3 et le revêtement à gradient de composition de BHAp/BG45S5+10wt. % Bi_2O_3. Le revêtement monocouche de BG45S5 + 10wt.% Bi_2O_3 a une microstructure et une structure amorphe similaires à celles du revêtement monocouche de BG45S5 sans Bi_2O_3 réalisé par projection plasma de la poudre commerciale . Cependant, une délamination et une vitesse réduite de formation de la couche d'apatite ont été observées. Le revêtement à gradient de composition de BHAp/BG45S5+10 wt. % Bi_2O_3 montre un taux de croissance de la couche d'apatite similaire à celui du revêtement monocouche de BG45S5+10wt. % Bi_2O_3. La formation d'apatite observée après 10 jours d'immersion dans un fluide corporel simulé ne présente pas de délaminage à la surface du revêtement grâce au gradient de composition du BG45S5 10 wt. % Bi_2O_3 combiné au BHAp.

RESUMEN

La hidroxiapatita (HAp) y el vidrio bioactivo (BG) 45S5 se emplean ampliamente como precursores de recubrimientos fabricados por proyección térmica para mejorar la biocompatibilidad de implantes biomédicos. Esto, debido a la estructura similar de la HAp y el tejido óseo y la alta reactividad del BG en medio biológico, lo que permite el rápido crecimiento del tejido óseo en su superficie. La proyección combinada de ambos materiales permite fabricar recubrimientos altamente bioactivos y estables en comparación con los recubrimientos individuales. Además, la bioactividad de la HAp y la radio-opacidad del BG45S5 pueden mejorarse obteniendo el primero a partir de fuentes naturales, como la HAp derivada de hueso bovino (BHAp) y la adición de radio-opacificadores como el Bi_2O_3 a la estructura del BG. En consecuencia, se pueden obtener recubrimientos combinados con bioactividad aumentada y opacidad a los rayos X para mejorar el diagnóstico no invasivo mediante imágenes radiográficas de implantes biomédicos recubiertos.

Esta investigación presenta el análisis de la estructura, microestructura y bioactividad de recubrimientos radiopacos de BHAp/BG45S5+Bi_2O_3 obtenidos por proyección térmica siguiendo la fabricación y las propiedades de los materiales y la proyección gradual del recubrimiento combinado. Los resultados experimentales muestran que la materia prima de BHAp es principalmente apatita carbonatada de tipo B con una alta pureza de fase de HAp de. Los polvos BG45S5 fabricados en laboratorio muestran la composición química y propiedades físicas con una similitud sustancial en comparación al BG45S5 comercial. El porcentaje en peso de 1 a 20 de Bi_2O_3 se añadió al vidrio bioactivo para modificar su radio-opacidad. Las imágenes radiográficas del BG45S5+Bi_2O_3 muestran que el 10% en peso del material opacificador permite aumentar la opacidad de la mezcla de BG de manera homogénea en 3.6 veces sin efectos considerables en sus propiedades estructurales y térmicas.

Con respecto a los recubrimientos fabricados por proyección térmica, el contenido de CO_3^{2-} y Mg en la BHAp, conducen a la formación de dolomita en la fase cristalina de la superficie del recubrimiento individual de BHAp por HVOF. El recubrimiento individual de BHAp por APS no muestra ninguna fase secundaria en el contenido cristalino de su superficie. Una típica capa de apatita es evidente en la superficie de ambos recubrimientos después de 3 días de inmersión en fluido corporal simulado (SBF) y el recubrimiento individual de BHAp por HVOF muestra una delaminación después de 5 días de inmersión. Por lo tanto, se eligió APS para depositar y analizar recubrimientos individuales de BHAp, BG45S5, BG45S5+10 wt. % Bi_2O_3 y el recubrimiento gradual de BHAp/BG45S5+10wt. % Bi_2O_3. El recubrimiento individual de

BG45S5+10wt. % Bi_2O_3 tiene una estructura amorfa y microestructura similares en comparación con el recubrimiento individual proyectado por plasma usando polvo de BG45S5 comercial sin Bi_2O_3. Sin embargo, se observó delaminación y una tasa reducida de formación de la capa de apatita. El recubrimiento gradual de BHAp/BG45S5+10 wt. % Bi_2O_3 muestra una tasa similar de crecimiento de la capa de apatita en comparación con el recubrimiento individual de BG45S5+10 wt. % Bi_2O_3. No obstante, se observa la formación de apatita después de 10 días de inmersión en SBF y la no delaminación en la superficie del recubrimiento debido a la proyección gradual del BG45S5 10 wt. % Bi_2O_3 combinado con la BHAp.

CHAPTER 1: PRELIMINARIES

1. INTRODUCTION

Joint replacements are considered as one of the most successful surgical interventions in health care systems [1]. The large market around the biomedical industry related to orthopedic technologies and joint replacement has allowed achieving considerable development in techniques and technologies to the community of interest. In 2011, this market represented revenues of up to USD 13.8 billion around the world. USD 12.71 billion from these incomes were invested in the acquisition of hip and knee implants [2]. In 2022 hip prostheses' incomes will be increased by 3.6% [3]. The demographic increase of the world population and of those over 60 years of age have increased the demand for these types of implants. In addition, pathologies such as osteoarthritis (56%), osteoporosis (75%), and hip fractures (86%) are the most common among this population [2]. Thus, age has to be added to other risk factors in diseases related to the skeletal muscle system such as overweight, physical inactivity, diabetes, and excess alcohol which are factors that also represent increasing trends. Particularly for Mexico, an increase of approximately 4 times the amount of hip fractures in women and approximately 3 times in men has projected to 2022 according to the Secretariat of Health of Mexico. These predictions are not different from those in other countries. For instance, in 2010 hip fractures represent 61% of total fractures and 20-24% morbidity and mortality rates in France and 148500 interventions were performed to replace fractured hips according to the OECD. Therefore, having high-quality procedures, technology, and materials will set the tone for those governmental, research or health entities that can offer the best solution to the population's problems, at local and global levels. Research in materials science has played a leading in role working with governments, medical specialists, patients, research centers, and private entities seeking to improve the performance of the materials used in the treatments of these public health diseases.

The treatment of diseases related to functional or reduced joint loss has exponentially improved the quality of life of patients in the last 60 years. Particularly, the development of metal load implants (Ti, TiAlV, Cr, stainless steel, and other alloys prosthesis) to support the musculoskeletal system has proven to be one of the main goals in the biomedical industry.

The biocompatibility of metallic implants has been enhanced, increasing the quality of medical devices with better immunological responses, the longer residence time of implantation, and

reducing postoperative interventions. This has been achieved, among different technologies development, thanks to the addition of ceramic coatings in metal devices allowing to maintain the mechanical properties of implants exposed to high loads and improving the interaction of the implants with the biological environment. The ceramics used in these applications can be bioinert metal oxides such as TiO_2, Al_2O_3, or bioactive such as glass or certain calcium phosphates. The biomedical industry that works on implants coated with high-tech materials, has begun to focus its interest on ceramics that increase mechanical stability and demonstrate to enhance the positive response of the surrounding tissue. This is the case bioactive glasses (BG) or hydroxyapatite (HAp) which are materials that allow a proper cell the differentiation and adhesion increasing the biocompatibility of metallic or other materials when are used as coatings [4–7].

BG and HAp are reference materials in biomedical coatings thanks to their high reactivity and adequate physical-chemical interaction with bone or muscle tissues. It is worth mentioning the interest in BG's, part of which represents greater bioactivity and adhesion with bone tissue compared to HAp [8]. However, the chemical stability of BG does not reach that of HAp when used as part of a coated surface [9]. On the other hand, it is difficult to preserve most properties of the raw materials and desired coating characteristics in the manufacture of BG or HAp coatings [10–19]. Thermal spray is a versatile technique that has a wide range of processes to overcome this disadvantage. From these processes, plasma spray (PS), including vacuum plasma spray (VPS), atmospheric plasma spray (APS), controlled atmospher plasma spray (CAPS), and suspension plasma spray (SPS), is a standardized and one of the most common methods used to deposit HAp and BG on metallic implants, being APS the most used compared to others [20–24]. Despite the good performance of these coatings, plasma-sprayed HAp shows (ACP) and calcium oxide (CaO) reducing the coating stability and mechanical performance [25–30]. Therefore, using projection techniques that allow working under lower temperatures (i.e. HVOF, HVAF, Cold Spray), is an alternative to avoid the HAp decomposition improving the HAp performance in single or combined coatings with high bioactive materials as BG [31,32]. In addition, BG thermal spray coatings have also shown remarkable bioactive properties using either plasma or high-velocity processes [24,33,34]. Hence, is expected that combined coatings of these materials obtained by thermal spray show enhanced bioactivity and stability compared to single HAp or BG deposits. In fact, while BG increases the growth rate of apatite crystals on their surface faster than HAp, thermally sprayed HAp improves the stability of HAp/BG coatings due to its low dissolution rate in comparison with single BG

deposit [35,36]. Furthermore, the architecture of HAp/BG coatings is another variable that impacts the coating performance. Regarding this, it has been showed that the gradual composition of multilayers from 100 % of HAp to 100 % of BG present promising performance in comparison with other architectures [37].

On the other hand, the source of feedstock powders, either commercial or in-lab prepared is an essential factor to obtain high quality thermally sprayed HAp or BG coatings [38–41]. These two choices present considerable costs in the fabrication of thermally sprayed deposits. However, the in-lab preparation of BG and HAp powders allows change the composition or doping these materials with different ions, such as Ag^{+}, Zn^{2+}, Si, Sr^{2+}, F^{-}, Fe^{2+} CO_3^{2-} and Mg^{2+}, among others, enhancing mechanical performance bioactivity, biocompatibility or antibacterial activity of the material [42–51] [52–56].

An alternative methodology to obtain doped carbonated apatites is to extract biological HAp from natural sources such as bones from fish, porcine, bovine, among others, where favorable quantities of ions such as Mg^{2+} and CO_3^{2-} are found [57–59]. Additionally, chemical routes to obtain HAp and doped HAp either increases the operational costs or is biologically unsafe than other routes [60]. Bovine bone is an attractive source to obtain biological HAp given its availability, bioactivity, and low cost [61–63]. Bovine derived HAp (BHAp) is a Ca-deficient HAp and contains several structural substitutions (i.e. monovalent and divalent substitutions like CO_3^{2-}, Sr^{2+}, Ba^{2+}, Mg^{2+}, Na^{+}, K^{+} or vacancies in Ca sites), which play a crucial role in the bone mechanical and bioactive performance [64] and confers biomimetic properties to the BHAp compared to HAp [65]. BHAp has been barely used as a feedstock material in thermal spray processing. Thus, there is a lack of information about its behavior in thermal spray deposition due to the variable composition of BHAp, its structural deformations, making the analysis in coatings rather complex [66,67]. As mentioned before, HVOF is an alternative to solve the HAp decomposition in the coating build-up [68–70]. To the authors' knowledge there are no contributions in the use of BHAp as feedstock either in the fabrication of HVOF coatings, the analysis of its bioactivity response, the role of the structural and elemental differences with HAp coatings and it uses in additions to other ceramics to fabricate composites, topcoat bond coat or gradual coatings.

Regarding BG, silicates and more specific, the 45S5 composition (45 wt. % SiO_2, 24.5 wt. % CaO, 24.5 wt. % Na_2O and 6 wt. % P_2O_5) is a promising bioactive glass due to its osteoconduction bioactivity and mechanical properties in comparison with other type of BG (i.e. borates, phosphate or doped glasses) [71]. Certain variants of lab-made BG45S5 have been

studied considering the versatility of the melt and fast quenching method to fabricate bioactive glasses. For instance, the addition of K_2O instead of the Na_2O oxide, increments on the CaO content [37,72] or the addition of ions such as Sr^{2+}, Cu^{2+}, B^{3+}, Fe^{2+}, Ti^{2+} among others [73–75]. The main objective of these types of investigations is to improve the biocompatibility, durability, and performance of the raw materials or coated implants such as those used in the replacement or support bone tissue. A common way to evaluate such performance is to carry out non-invasive studies after surgical implantation by means of x-ray radiology studies [76]. Hence, it is possible to evaluate the integration of the implant in the bone or to detect failures in the interface of these two caused by protective efforts or shielding stresses [77,78]. In this postoperative radiological studies, BG or HAp coated implants represent lower contrast detection in comparison with no coated devices due to the ceramics low radiopacity to X-ray exposure [79,80]. Consequently, the non-invasive radiological evaluation of patients using biomedical devices with this type of bioceramic coatings will be negatively affected by the change in the surface radiopacity. The addition of radiopaque material within a BHAp/BG coating will enhance the deposit contrast. Some researchers have made approaches regarding the study of the bioactivity and radiopacity properties of BG45S5 with Bi_2O_3 and other compounds with dense atoms [81,82]. Nevertheless, these contributions pointed out the application of this alternative material for dentistry purposes and there are no reports concerning no loading baring uses or coatings studies to the authors knowledge. Moreover, these studies analyzed the fabrication of radiopaque BG45S5 through more complicated processes such flame spray pyrolysis in comparison with the traditional melt and fast quenching method. Additionally, low or high ranges in the Bi_2O_3 content have been reported (i.e. 4 – 8 % and 20 – 50%), leaving a lack of information regarding a wide range of possible additions of this oxide and showing low increments in the BG45S5 radiopacity.

The present contributions aim to develop and analyze the structure, microstructure, and bioactivity of radiopaque BHAp/BG45S5+Bi_2O_3 coatings obtained by thermal spray following the fabrication and properties of the feedstock materials and the gradual deposition of the combined coating as an alternative of high scientific and academic interest. Furthermore, this work seeks to promote international collaboration between the National Center for Thermal Projection (CENAPROT) from CINVESTAV and the Ceramic Research Laboratory (IRCER) of the University of Limoges, through the study of this radiopaque coating system obtained by thermal spraying techniques and the combination of the capacities of both laboratories.

2. RESEARCH GOALS

General Objective

To develop a graded coating of biohydroxiapatite/bioactive glass with radiopaque functionalities by thermal spray monitoring its morphology, microstructure and bioactivity properties in the framework of the IRCER-Cenaprot collaborative efforts.

Specific Objectives

- To obtain biohydroxyapatite powder from bovine bone with microstructural characteristics suitable to be used as feedstock for thermal spray processes.
- To synthesize bioactive glass powder 45S5 to be used as feedstock for thermal spray processes.
- To enhance the radiopacity of lab-made bioactive glass 45S5 feedstock powder by the addition of Bi_2O_3.
- To evaluate de bioactivity of single biohydroxyapatite and bioactive glass 45S5+Bi_2O_3 and coatings.
- To evaluate the bioactivity of radiopaque graded biohydroxyapatite/bioactive coatings using *in-vitro* test.

3. NOVELTY STATEMENT OF THE CONTRIBUTION

The objective of this work is part of the actual efforts made by scientists and health care workers seeking to increase the biocompatibility, lifespan, and functionalities of coated biomedical implants. The new generation of smart materials that can be used in biomedical applications opens a wide research field to functionalize surfaces and increase the performance of coated medical devices. This is the case of the novelty contribution from this research were modified and smart ceramics such as biohydroxyapatite (BHAp) and radiopaque bioactive glass 45S5 are used to functionalize metallic surfaces by thermal spray processes.

Firstly, the fabrication of both feedstock powders and their complete analysis gives considerable information to understand the relevance and performance of these materials as thermally sprayed coatings: The difference between stoichiometric HAp and BHAp, and the understanding of the behavior of the second within APS and HVOF processes were described. The analysis leads to explain the formation of a secondary phase on the use of HVOF to prepare BHAp coatings and the disadvantages of the presence of this phase on the coating bioactivity. Moreover, the fabrication of the BG45S5 powder from their oxides and carbonate precursors leads to propose and describe the influence on the addition of a radio-opacifier, as the Bi_2O_3. Following this process, the addition of the radio-opaque oxide leads to obtain a high radio-opaque bioactive glass in a more effective methodology in comparison with those used in previous contributions and patents.

The influence of the structural and elemental changes of these ceramics in comparison with their similars, as HAp and BG45S5, on thermally sprayed coatings was explained. In addition, the combination of these two ceramics in a coating with a gradual configuration and its comparison with a single BG45S5+Bi_2O_3 deposit was also studied.

Finally, it was found that thermally sprayed coating using BHAp and radiopaque BG45S5+Bi_2O_3 shows high bioactivity and stability representing an interesting option to functionalize metallic devices by thermal spray to increase their lifespan, biocompatibility, and radiopacity for postoperative performance evaluations.

REFERENCES

[1] OECD, Hip and knee replacement, Heal. a Glance Eur. 2012. (2012) 86–87. doi:10.1787/9789264183896-37-en.

[2] C. Provines, Strategic insights into the orthopaedic industry, Orthoknow. (2013) 1–8. http://www.valuevantagepartners.com/wp-content/uploads/2013/05/orthoknow1304-Pricing-Pressure_Provines-April-2013.pdf.

[3] D.B.M. Research, Global Hip Replacement Implants Market –Trends and Forecast to 2022, 2016.

[4] Y. Jamie, S. Chye, J. Loo, J. Lee, J. Ma, Investigation of the bioactivity and biocompatibility of different glass interfaces with hydroxyapatite, fluorohydroxyapatite and 58S bioactive glass, BIoFactors 30. 30 (2007) 205–216. doi:10.1002/biof.5520300402.

[5] T. V Thamaraiselvi, S. Rajeswari, Biological Evaluation of Bioceramic Materials - A Review, Trends Biomater. Artif. Organs. 18 (2004) 9–17.

[6] M. Hott, B. Noel, D. Bernache-assolant, C. Rey, P.J. Marie, Proliferation and differentiation of human trabecular osteoblastic cells on hydroxyapatite, J. Biomed. Mater. Res. 37 (1996) 508–5016. doi:10.1002/(sici)1097-4636(19971215)37:4<508::aid-jbm9>3.0.co;2-p.

[7] O. Tsigkou, J.R. Jones, J.M. Polak, M.M. Stevens, Biomaterials Differentiation of fetal osteoblasts and formation of mineralized bone nodules by 45S5 Bioglass conditioned medium in the absence of osteogenic supplements, Biomaterials. 30 (2009) 3542–3550. doi:10.1016/j.biomaterials.2009.03.019.

[8] L.L. Hench, Bioglass and similar materials, in: Encycl. Mater. Sci. Technol., Elsevier Science Ltd, 2001: pp. 563–568. doi:10.1016/B0-08-043152-6/00108-X.

[9] A. Cattini, D. Bellucci, A. Sola, L. Pawłowski, V. Cannillo, Functional bioactive glass topcoats on hydroxyapatite coatings: Analysis of microstructure and in-vitro bioactivity, Surf. Coatings Technol. 240 (2014) 110–117. doi:10.1016/j.surfcoat.2013.12.023.

[10] B. Mavis, A.C. Taş, Dip Coating of Calcium Hydroxyapatite on Ti-6Al-4V Substrates, J. Am. Ceram. Soc. 83 (2000) 989–991. doi:10.1111/j.1151-2916.2000.tb01314.x.

[11] M. Metikoš-Huković, E. Tkalacec, A. Kwokal, J. Piljac, An in vitro study of Ti and Ti-alloys coated with sol-gel derived hydroxyapatite coatings, Surf. Coatings Technol. 165 (2003) 40–50. doi:10.1016/S0257-8972(02)00732-6.

[12] H. Wang, N. Eliaz, Z. Xiang, H.-P. Hsu, M. Spector, L.W. Hobbs, Early bone apposition in vivo on plasma-sprayed and electrochemically deposited hydroxyapatite coatings on titanium alloy., Biomaterials. 27 (2006) 4192–203. doi:10.1016/j.biomaterials.2006.03.034.

[13] T. Onoki, T. Hashida, New method for hydroxyapatite coating of titanium by the hydrothermal hot isostatic pressing technique, Surf. Coatings Technol. 200 (2006) 6801–6807. doi:10.1016/j.surfcoat.2005.10.016.

[14] S.J. Ding, C.P. Ju, J.H.C. Lin, Characterization of hydroxyapatite and titanium coatings sputtered on Ti-6Al-4V substrate, J. Biomed. Mater. Res. 44 (1999) 266–279. doi:10.1002/(SICI)1097-4636(19990305)44:3<266::AID-JBM5>3.0.CO;2-4.

[15] B. Ben-nissan, Advances in Calcium Phosphate Biomaterials, Springer, 2014. doi:10.1007/978-3-642-53980-0.

[16] J.. Gomez-Vega, E. Saiz, a. . Tomsia, G.. Marshall, S.. Marshall, Bioactive glass coatings with hydroxyapatite and Bioglass® particles on Ti-based implants. 1. Processing, Biomaterials. 21 (2000) 105–111. doi:10.1016/S0142-9612(99)00131-3.

[17] R. Comesaña, F. Quintero, F. Lusquiños, M.J. Pascual, M. Boutinguiza, A. Durán, J. Pou, Laser cladding of bioactive glass coatings, Acta Biomater. 6 (2010) 953–961. doi:10.1016/j.actbio.2009.08.010.

[18] a Sola, D. Bellucci, V. Cannillo, a Cattini, Bioactive glass coatings: a review, Surf. Eng. 27 (2011) 560–572. doi:10.1179/1743294410Y.0000000008.

[19] J.N. Oliver, D. Zhu, Y. Su, X. Lu, P. Kuo, J. Du, Bioactive Materials Bioactive glass coatings on metallic implants for biomedical applications, Bioact. Mater. 4 (2019) 261–270. doi:10.1016/j.bioactmat.2019.09.002.

[20] V.F. Shamray, V.P. Sirotinkin, I. V Smirnov, V.I. Kalita, A.Y. Fedotov, S.M. Barinov, Structure of the hydroxyapatite plasma-sprayed coatings deposited on pre- heated titanium substrates, Ceram. Int. 43 (2017) 9105–9109. doi:10.1016/j.ceramint.2017.04.057.

[21] L. Sun, C.C. Berndt, K.A. Gross, A. Kucuk, Material Fundamentals and Clinical Performance of Plasma- Sprayed Hydroxyapatite Coatings : A Review, J. Mater. Res. 58 (2001) 570–592. doi:10.1002/jbm.xxxx.

[22] L. Sun, Thermal Spray Coatings on Orthopedic Devices: When and How the FDA Reviews Your Coatings, J. Therm. Spray Technol. 27 (2018) 1280–1290. doi:10.1007/s11666-018-0759-2.

[23] J. Henao, C. Poblano-Salas, M. Monsalve, J. Corona-Castuera, Bio-active glass coatings manufactured by thermal spray: a status report, J. Mater. Res. Technol. 8 (2019) 4965–4984. doi:10.1016/j.jmrt.2019.07.011.

[24] G. Bolelli, D. Bellucci, V. Cannillo, R. Gadow, A. Killinger, L. Lusvarghi, P. Müller, A. Sola, Comparison between Suspension Plasma Sprayed and High Velocity Suspension Flame Sprayed bioactive coatings, Surf. Coatings Technol. 280 (2015) 232–249. doi:10.1016/j.surfcoat.2015.08.039.

[25] J. Cihlář, A. Buchal, M. Trunec, Kinetics of thermal decomposition of hydroxyapatite bioceramics, J. Mater. Sci. 34 (1999) 6121–6131. doi:10.1023/A:1004769820545.

[26] C.J. Liao, F.H. Lin, K.S. Chen, J.S. Sun, Thermal decomposition and reconstruction of hydroxyapatite in air atmosphere, Biomed. Sci. Instrum. 35 (1999) 99–104.

[27] P. Cheang, K.A. Khor, Addressing processing problems associated with plasma spraying of hydroxyapatite coatings, Biomaterials. 17 (1996) 537–544. doi:10.1016/0142-9612(96)82729-3.

[28] R.B. Heimann, Plasma-Sprayed Hydroxylapatite-Based Coatings: Chemical, Mechanical, Microstructural, and Biomedical Properties, J. Therm. Spray Technol. 25 (2016) 827–850. doi:10.1007/s11666-016-0421-9.

[29] S. Amin, H. Panchal, A Review on Thermal Spray Coating Processes, Int. J. Curr. Trends Eng. Res. Sci. J. Impact Factor. 2 (2016) 556–563. http://www.ijcter.com.

[30] J. Chen, W. Tong, Y. Cao, J. Feng, X. Zhang, Effect of atmosphere on phase transformation in plasma-sprayed hydroxyapatite coatings during heat treatment, J. Biomed. Mater. Res. 34 (1997) 15–20. doi:10.1002/(SICI)1097-4636(199701)34:1<15::AID-JBM3>3.0.CO;2-Q.

[31] H. Li, K.A. Khor, P. Cheang, Effect of the powders' melting state on the properties of

HVOF sprayed hydroxyapatite coatings, Mater. Sci. Eng. A. 293 (2000) 71–80. doi:10.1016/S0921-5093(00)01245-4.

[32] J.L. Ong, M. Appleford, S. Oh, Y. Yang, W. Chen, J.D. Bumgardner, W.O. Haggard, The Characterization and Development of Bioactive Hydroxyapatite Coatings, Surf. Modif. Cation Bioapplications. (2006) 67–69.

[33] G. Bolelli, V. Cannillo, R. Gadow, A. Killinger, L. Lusvarghi, J. Rauch, Microstructural and in vitro characterisation of high-velocity suspension flame sprayed (HVSFS) bioactive glass coatings, J. Eropean Ceram. Soc. 29 (2009) 2249–2257. doi:10.1016/j.jeurceramsoc.2009.01.032.

[34] G. Bolelli, D. Bellucci, V. Cannillo, L. Lusvarghi, A. Sola, N. Stiegler, P. Müller, A. Killinger, R. Gadow, L. Altomare, L. De Nardo, Suspension thermal spraying of hydroxyapatite : Microstructure and in vitro behaviour, Mater. Sci. Eng. C. 34 (2014) 287–303. doi:10.1016/j.msec.2013.09.017.

[35] J.H. Chern Lin, K.S. Chen, C.P. Ju, Biocorrosion behavior of hydroxyapatite/bioactive glass plasma sprayed on Ti6A14V, Mater. Chem. Phys. 41 (1995) 282–289. doi:10.1016/0254-0584(95)80035-2.

[36] J.H.C. Lin, M.L. Liu, C.P. Ju, Structure and properties of hydroxyapatite- bioactive glass composites plasma sprayed on Ti6AI4V, J. Mater. Sci. Mater. Med. 5 (1994) 279–283.

[37] A. Cattini, D. Bellucci, A. Sola, L. Pawłowski, V. Cannillo, Microstructural design of functionally graded coatings composed of suspension plasma sprayed hydroxyapatite and bioactive glass, J. Biomed. Mater. Res. Part B Appl. Biomater. 102 (2014) 551–560. doi:10.1002/jbm.b.33034.

[38] K. Kulpetchdara, A. Limpichaipanit, G. Rujijanagul, Influence of the nano hydroxyapatite powder on thermally sprayed HA coatings onto stainless steel, Surf. Coat. Technol. 306 (2016) 181–186. doi:10.1016/j.surfcoat.2016.05.069.

[39] P. Gkomoza, M. Vardavoulias, D.I. Pantelis, C. Sarafoglou, Comparative study of structure and properties of thermal spray coatings using conventional and nanostructured hydroxyapatite powder, for applications in medical implants, Surf. Coat. Technol. 357 (2019) 748–758. doi:10.1016/j.surfcoat.2018.10.044.

[40] R.S. Lima, K. a. Khor, H. Li, P. Cheang, B.R. Marple, HVOF spraying of nanostructured

hydroxyapatite for biomedical applications, Mater. Sci. Eng. A. 396 (2005) 181–187. doi:10.1016/j.msea.2005.01.037.

[41] E. Cañas, M. Vicent, E. Bannier, P. Carpio, M.J. Orts, E. Sanchéz, Effect of particle size on processing of bioactive glass powder for atmospheric plasma spraying, J. Eur. Ceram. Soc. 36 (216AD) 837–845. doi:10.1016/j.jeurceramsoc.2015.09.039.

[42] M. Roy, G.A. Fielding, H. Beyenal, A. Bandyopadhyay, S. Bose, Mechanical, in vitro antimicrobial, and biological properties of plasma-sprayed silver-doped hydroxyapatite coating, ACS Appl. Mater. Interfaces. 4 (2012) 1341–1349. doi:10.1021/am201610q.

[43] D. Ke, A.A. Vu, A. Bandyopadhyay, S. Bose, Compositionally graded doped hydroxyapatite coating on titanium using laser and plasma spray deposition for bone implants, Acta Biomater. 84 (2019) 414–423. doi:10.1016/j.actbio.2018.11.041.

[44] R. Sasidharan Pillai, Synthesis and Characterization of Calcium Phosphate Powders for Biomedical Applications by Plasma Spray Coating, University of Trento, 2015. http://eprints-phd.biblio.unitn.it/1433/.

[45] R.T. Candidato, C. Thouzellier, L. Pawłowski, Evaluation of the in-vitro behavior of nanostructured hydroxyapatite and zinc doped hydroxyapatite coatings obtained using solution precursor plasma spraying, J. Biomed. Mater. Res. - Part B Appl. Biomater. 106 (2018) 2101–2108. doi:10.1002/jbm.b.34014.

[46] T.J. Webster, E.A. Massa-Schlueter, J.L. Smith, E.B. Slamovich, Osteoblast response to hydroxyapatite doped with divalent and trivalent cations, Biomaterials. 25 (2004) 2111–2121. doi:10.1016/j.biomaterials.2003.09.001.

[47] P. Habibovic, C.M. Van der Valk, K. De Groot, P. Layrolle, Osteo-integration of plasma-spray, biomimetic octacalcium phosphate and carbonate-apatite coatings on titanium implants, Key Eng. Mater. 240–242 (2003) 387–390. doi:10.4028/www.scientific.net/KEM.240-242.387.

[48] A. Gozalian, A. Behnamghader, M. Daliri, A. Moshkforoush, Synthesis and thermal behavior of Mg-doped calcium phosphate nanopowders via the sol gel method, Sci. Iran. 18 (2011) 1614–1622. doi:10.1016/j.scient.2011.11.014.

[49] C.M. Mardziah, I. Sopyan, M. Hamdi, S. Ramesh, Synthesis of strontium-doped hydroxyapatite powder via sol-gel method, Med. J. Malaysia. 63 Suppl A (2008) 79–80.

doi:10.4028/www.scientific.net/AMR.47-50.928.

[50] E.A. Ofudje, A.I. Adeogun, M.A. Idowu, S.O. Kareem, Synthesis and characterization of Zn-Doped hydroxyapatite: scaffold application, antibacterial and bioactivity studies, Heliyon. 5 (2019). doi:10.1016/j.heliyon.2019.e01716.

[51] R.H. Ali, H. Ageorges, S. Nasr, E. Ben Salem, Zinc and strontium co-substituted hydroxyfluorapatite: Synthesis, sintering and mechanical properties, Mater. Res. Bull. 112 (2019) 84–94. doi:10.1016/j.materresbull.2018.11.042.

[52] L. Li, X. Lu, Y. Meng, C.M. Weyant, Comparison study of biomimetic strontium-doped calcium phosphate coatings by electrochemical deposition and air plasma spray: Morphology, composition and bioactive performance, J. Mater. Sci. Mater. Med. 23 (2012) 2359–2368. doi:10.1007/s10856-012-4633-3.

[53] E. Kergourlay, D. Grossin, N. Cinca, C. Josse, S. Dosta, G. Bertrand, I. Garcia, J.M. Guilemany, C. Rey, First Cold Spraying of Carbonated Biomimetic Nanocrystalline Apatite on Ti6Al4V: Physical-Chemical, Microstructural, and Preliminary Mechanical Characterizations, Adv. Eng. Mater. 18 (2016) 496–500. doi:10.1002/adem.201500409.

[54] W.C.A. Vrouwenvelder, C.G. Groat, K. De Groot, Better histology and biochemistry for osteoblasts cultured on titanium- doped bioactive glass: Bioglass 45S5 compared with iron-, titanium-, fluorine-, and boron-containing bioactive glasses, Biomaterials. 15 (1994) 97–106. doi:10.1016/0142-9612(94)90257-7.

[55] J. Pratten, S.N. Nazhat, J.J. Blaker, A.R. Boccaccini, In Vitro Attachment of Staphylococcus Epidermidis to Surgical Sutures with and without Ag-Containing Bioactive Glass Coating, J. Biomater. Appl. 19 (2015) 47–57. doi:10.1177/0885328204043200.

[56] A. Hoppe, R. Meszaros, C. Stahlim, S. Romeris, J. Schmidt, W. Peukert, B. Marelli, S.N. Nazhat, L. Wondraczek, J. Lao, A.R. Boccaccini, In vitro reactivity of Cu doped 45S5 Bioglass® derived scaffolds for bone tissue engineering, J. Mater. Chem. B. 2 (2013) 5659–5674. doi:10.1039/c3tb21007c.

[57] C.Y.M. Maurice, Inductively Coupled Plasmas: Ion Dynamics and Interactions with Bone Tissue, Technische Universiteit Eindhoven, 2003. doi:10.6100/IR563477.

[58] M. Ozawa, S. Suzuki, Microstructural Development of Natural Hydroxyapatite

Originated from Fish-Bone Waste through Heat Treatment, J. Biomed. Mater. Res. 85 (2002) 1315–1317.

[59] T. Aoba, E.C. Moreno, S. Shimoda, Competitive adsorption of magnesium and calcium ions onto synthetic and biological apatites, Calcif. Tissue Int. 51 (1992) 143–150. doi:10.1007/BF00298503.

[60] N.A.M. Barakat, M.S. Khil, A.M. Omaran, F.A. Sheikh, H. Yong, Extraction of pure natural hydroxyapatite from the bovine bones bio waste by three different methods, J. Mater. Process. Technol. 9 (2008) 3408–3415. doi:10.1016/j.jmatprotec.2008.07.040.

[61] J. Lamsihar Manalu, B. Soegijono, D.J. Indrani, Characterization of Hydroxyapatite Derived from Bovine Bone, 2015.

[62] F.A. Sheikh, M.A. Kanjwal, J. Macossay, N.A.M. Barakat, H.Y. Kim, A simple approach for synthesis, characterization and bioactivity of bovine bones to fabricate the polyurethane nanofiber containing hydroxyapatite nanoparticles, Express Polym. Lett. 6 (2012) 1–22. doi:10.3144/expresspolymlett.2012.5.A.

[63] S. Hospital, A. Hospital, Clinical result of sintered bovine hydroxyapatite bone substitute: analysis of the interface reaction between tissue and bone substitute, J. Orthopeadic Sci. 15 (2010) 223–232. doi:10.1007/s00776-009-1441-9.

[64] A. Nather, Bone grafts and bone substitutes: Basic science and clinical applications, 2005. doi:10.1142/5695.

[65] C. Drouet, Apatite formation: Why it may not work as planned, and how to conclusively identify apatite compounds, Biomed Res. Int. 2013 (2013) 12. doi:10.1155/2013/490946.

[66] L.S. Ozyegin, F.N. Oktar, G. Goller, E.S. Kayali, T. Yazici, Plasma-sprayed bovine hydroxyapatite coatings, Mater. Lett. 58 (2004) 2605–2609. doi:10.1016/j.matlet.2004.03.033.

[67] G. Goller, F.N. Oktar, L.S. Ozyegin, E.S. Kayali, E. Demirkesen, Plasma-sprayed human bone-derived hydroxyapatite coatings : effective and reliable, Mater. Lett. 58 (2004) 2599–2604. doi:10.1016/j.matlet.2004.03.032.

[68] H. Li, K. a Khor, P. Cheang, Properties of heat-treated calcium phosphate coatings deposited by high-velocity oxy-fuel (HVOF) spray, Biomaterials. 23 (2002) 2105–12. http://www.ncbi.nlm.nih.gov/pubmed/11962650.

[69] J. Fernández, M. Gaona, J.M. Guilemany, Effect of Heat Treatments on HVOF Hydroxyapatite Coatings, J. Therm. Spray Technol. 16 (2007) 220–228. doi:10.1007/s11666-007-9034-7.

[70] M.G. Latorre, Recubrimientos biocompatibles obtenidos por proyección térmica y estudio in vitro de la función osteoblástica, Universitat de Barcelona, 2007.

[71] G. Kaur, O.P. Pandey, K. Singh, D. Homa, B. Scott, G. Pickrell, A review of bioactive glasses: Their structure, properties, fabrication and apatite formation, J. Biomed. Mater. Res. Part A. 102 (2014) 254–274. doi:10.1002/jbm.a.34690.

[72] D. Bellucci, G. Bolelli, V. Cannillo, R. Gadow, a. Killinger, L. Lusvarghi, a. Sola, N. Stiegler, High velocity suspension flame sprayed (HVSFS) potassium-based bioactive glass coatings with and without TiO2 bond coat, Surf. Coatings Technol. 206 (2012) 3857–3868. doi:10.1016/j.surfcoat.2012.02.041.

[73] L. Milkovic, A. Hoppe, R. Detsch, A.R. Boccaccini, N. Zarkovic, Effects of Cu-doped 45S5 bioactive glass on the lipid peroxidation-associated growth of human osteoblast-like cells in vitro, J. Biomed. Mater. Res. A. 102 (2013) 3556–3561. doi:10.1002/jbm.a.35032.

[74] A.A. Gorustovich, T. Steimetz, R.L. Cabrini, J.M. Porto López, Osteoconductivity of strontium-doped bioactive glass particles: A histomorphometric study in rats, J. Biomed. Mater. Res. A. 92 (2009) 232–237. doi:10.1002/jbm.a.32355.

[75] L.A. Durand, A. Góngora, J.M. Porto López, A.R. Boccaccini, M.P. Zago, A. Baldi, A. Gorustovich, In vitro endothelial cell response to ionic dissolution products from boron-doped bioactive glass in the Si2O-CaO-P2O5-Na2O system, J. Mater. Chem. B. 2 (2014) 7620–7630. doi:10.1039/C4TB01043D.

[76] C. Trevisan, M. Bigoni, R. Cherubini, P. Steiger, G. Randelli, S. Ortolani, S. Mediche, U. Studi, O. Maggiore, V.F. Sforza, Dual X-Ray Absorptiometry for the Evaluation of Bone Density from the Proximal Femur after Total Hip Arthroplasty : Analysis Protocols and Reproducibility, Calcif. Tissue Int. 53 (1993) 158–161. doi:10.1007/BF01321831.

[77] N. Mushtaq, K. To, C. Gooding, W. Khan, Radiological Imaging Evaluation of the Failing Total Hip Replacement, Front. Surg. 6 (2019) 1–13. doi:10.3389/fsurg.2019.00035.

[78] J. Vanrusselt, M. Vansevenant, G. Vanderschueren, Postoperative radiograph of the hip arthroplasty: what the radiologist should know, Insights Imaging. (2015) 591–600. doi:10.1007/s13244-015-0438-5.

[79] M.A.B.F. Francis, J. Annie, P.R.H. Varma, Nano iron oxide – hydroxyapatite composite ceramics with enhanced radiopacity, J. Mater. Sci. Mater. Med. 21 (2010) 1427–1434. doi:10.1007/s10856-010-4005-9.

[80] R. Madanat, N. Moritz, E. Vedel, E. Svedstro, H.T. Aro, Radio-opaque bioactive glass markers for radiostereometric analysis, Acta Biomater. 5 (2009) 3497–3505. doi:10.1016/j.actbio.2009.05.038.

[81] S. Prasad, I. Ratha, T. Adarsh, A. Anand, P.K. Sinha, P. Diwan, K. Annapurna, K. Biswas, In vitro bioactivity and antibacterial properties of bismuth oxide modified bioactive glasses, J. Mater. Res. 33 (2018) 178–190. doi:10.1557/jmr.2017.442.

[82] W.J. Stark, D. Mohn, M. Zehnder, T. Imfeld, Radio-opaque bioactive glass materials, 2012. https://patents.google.com/patent/US20120148646A1/en.

CHAPTER 2: STATE OF ART

The living tissues' performance is the result of millions of years of evolution, while the performance artificial substitutions that humankind used to repair damaged tissues are only a few decades old. The attempts to repair the human body with the use of implant materials are recorded in the early medical writings of the Hindu, Egyptian and Greek civilizations. In the 17th century, a piece of dog skull was successfully transplanted into the damaged skull of a Dutch duke. The Chinese recorded the first use of dental amalgam to repair decayed teeth 659 years AD, while pre-Columbian civilizations used gold sheets to heal cranial cavities following trepanation. Furthermore, in 1970, Amadeo Bobbio discovered Mayan skulls, some of then more than ~4000 years old, in which a missing tooth had been replaced by nacre substitutes. Nevertheless, many implantations failed due to infections, which tended to be increased by the presence of implants, since they provided a region inaccessible cells from the immunological system. Thus, the use of biomaterials did not was a matter of study until the development of the aseptic surgical technique developed by J. Lister in the 1860s. Furthermore, there was a lack of knowledge about the toxicity of the used materials. Years later, the first attempt to treat surgically defects in rabbits was performed in 1920 and the second clinical report was published 30 years later according to bibliographic reports [1].

The aging population has grown significantly while advances have been made in medical sciences. More organs, joints, and other critical body parts are replaced to maintain a good life quality. From these implants, there are some that play a major role in replacing or in the improvement of the function of different body systems (i.e. digestive, skeletal, circulatory, nervous, etc.). The used materials in these replacements are biomaterials. Some of the common implants include orthopedic devices such as total knee, hip, shoulder, and ankle joint replacements, spinal implants, and bone fixators; cardiac implants as artificial heart valves and pacemakers; soft tissue implants, as breast implants and injectable collagen for soft tissue augmentation; and dental implants to replace teeth/root systems and bone tissue [2].

Joint replacement surgery as hip and knee replacement is considered one of the most effective interventions, reducing pain and disability and restoring some patients to near normal function [3]. Metallic materials such as AISI 316L stainless steel (SS), Ti and its alloys and Co-Cr alloys are commonly employed as orthopedic implants considering their high strength and toughness compared to polymers and ceramic materials, respectively. However, metallic materials are susceptible to corrosive attack by body fluid, with subsequent release of metallic ions causing

adverse effects to surrounding tissues. Moreover, metallic surfaces may be bioinert but not completely bioactive and surface treatments are used to increase their bioactivity and biocompatibility[4]. The present work is concerned with orthopedic applications and, therefore, in this chapter, concepts such as bioinert, bioactivity and biocompatibility are defined, as well as the theory on the synthesis of the biomaterials involved in the application of the work, both of the raw material and of the coatings, their properties, and behaviors in biological environment.

1. BIOMATERIALS

Numerous definitions have been proposed to give a definition of biomaterials. However, in a more advanced definition was introduced in September of 2009, proposing the definition of a biomaterial as "a substance that has been engineered to take a form which, alone or as part of a complex system, is used to direct, by control of interactions with components of living systems, the course of any therapeutic or diagnostic procedure, in veterinary or human medicine" [5]. Biomaterials must be distinguished from biological materials because the former are the materials that are accepted by living tissues and, therefore, they might be used for tissue replacements, while the latter are the materials being produced by various biological systems (i.e. wood, cotton, bones, chitin, etc.). In addition, there are biomimetic materials, which are not made by living organisms but have similar composition, structure, and properties to biological materials [1].

Based on their composition, biomaterials can be classified into four major classes: metals, ceramics, polymers, and composites. Each class of materials has peculiar properties. For instance, metals exhibit high toughness and good mechanical properties; ceramics generally offer high wear resistance and hardness, while several polymers present chemical, physical and mechanical properties similar to those of living soft tissues. Additionally, biomaterials can be grouped according to their specific interactions with living tissues. Such classification also reflects the progressive evolution of biomaterials since the 1950s [6]:

- 1st generation: "bioinert" such as alumina and zirconia, Ti and Cr-Co alloys, and ultrahigh molecular weight polyethylene.
- 2nd generation: "bioactive" and "bioresorbable" such as calcium phosphates (hydroxyapatite, and β-tri-calcium phosphates), and bioactive glasses

- 3rd generation: porous 2nd generation biomaterials and composites containing biologically active substances such as cells, growth factors, proteins capable of regenerating new tissue [7].

One should note that these three generations should not be interpreted as the chronological but the conceptual since each generation represents an evolution of the requirements and properties of the biomaterials involved. This means that research and development are still devoted to biomaterials that, according to their properties, could be considered to be of the first or the second generations [1].

1.2.Biocompatibility

One of the most important properties of biomaterials is their so-called biocompatibility. Nonetheless, this is not an individual property and its related to the various interactions of the material with the cell and tissues. Hence, a systems approach is required. According to this, biocompatibility refers to the ability of a material to perform with an appropriate host response, in a specific application. Thus, biocompatibility is a collection of processes involving different but interdependent interaction mechanisms between material and living tissues. In increasing order of biocompatibility the interaction of biomaterials with living tissue can be defined as follows [8]:

- Incompatible materials: are materials that release to the body substances in toxic concentrations and/or trigger the formation of antigens that may cause immune reactions ranging from simple allergies to inflammation to septic rejection with the associated severe health consequences.
- Biocompatible materials, in contrast, are those that also release substances but in non-toxic concentrations that may lead to only benign tissue reactions such as the formation of a fibrous connective tissue capsule or weak immune reactions that cause the formation of giant cells or phagocytes. These materials are often called biotolerant and include austenitic stainless steels or bone cement consisting of polymethylmethacrylate (PMMA).
- Bioinert materials do not release any toxic constituents but also do not show positive interaction with living tissue. As a response of the body to these materials usually, a non-adherent capsule of connective tissue is formed around the bioinert material that in the case of bone remodeling manifests itself by shape-mediated contact osteogenesis. Through the bone-materials interface only compressive forces will be transmitted

("bony on-growth"). Typical bioinert materials are titanium and its alloys, ceramics such as alumina, zirconia, and titania, and some polymers, as well as carbon.

- Bioactive materials show positive interaction with living tissue that includes also differentiation of immature cells towards bone cells. In contrast to bioinert materials, there is chemical bonding to the bone along with the interface, thought to be triggered by the adsorption of bone growth-mediating proteins at the surface of the biomaterial. Hence there will be biochemically mediated strong bonding osteogenesis. In addition to compressive forces, to some degree tensile and shear forces can also be transmitted through the interface ("bony ingrowth"). Typical bioactive materials are calcium phosphates and bioactive glasses [8].

Generally, bioactive materials interact with surrounding bone resulting in the formation of a chemical bond to this tissue (bone-bonding). The bioactivity phenomenon is determined by both chemical factors, such as crystal phases and molecular structures of a biomaterial, and physical factors, such as surface roughness and porosity. A distinction between bioactive and bioresorbable biomaterials might be associated with a structural factor only. For example, bioceramics made from non-porous, dense and highly crystalline hydroxyapatite (HAp) behaves as a bioinert (but a bioactive) material and are retained in an organism for at least 5–7 years without noticeable changes, while highly porous bioceramics of the same composition can be resorbed approximately within a year. Furthermore, submicron-sized HAp powders are biodegraded even faster than the highly porous HAp scaffolds. One must stress that recently the concepts of bioactive and bioresorbable materials have converged and bioactive materials are made bioresorbable, while bioresorbable materials are made bioactive [1].

1.2.1. Bioactivity classification

The formation of an interfacial bond between tissue and implant appears to be the first step towards new tissue formation. The entity and the type of bond are variable according to the type of material used. The time required for the bond formation is another variable depending on the nature of the material and is related to the bioactivity index, defined in equation 1 [9]:

$$I_B = 100/t_{0.5bb} \tag{1}$$

where, $t_{0.5bb}$ is the time required for half of the material surface to establish the bond with the tissue. Given that the final goal is the complete regeneration of the physiological site, there are some important elements that are determinant to establish the host tissue/grafting material bond.

Considering bone tissue, the four characteristics that an ideal graft material should exhibit are [9]:

- Osseointegration, which is the ability to establish a chemical bond with the physiological tissue without the formation of a fibrous layer around the implant.
- Osteo-conduction, which is the ability to support the growth of new bone on the surface of the grafting material by allowing the growth of orientated blood vessels and the creation of new osteons (fundamental functional unit of much compact bone);
- Osteoinduction, which stimulates and activates pluripotent stem cells leading to their differentiation to an osteoblastic phenotype. During this process, which is mediated by a signaling cascade, some extracellular and intracellular receptors are involved.
- Osteogenesis, that involves the synthesis of new bone by osteoblasts that are present within the graft (if cell-seeded biomaterial constructs are used) or have colonized it after implantation [9].

Larry Hench classified materials into two classes of bioactivity on the basis of the level of interaction with the surrounding tissue that they exhibit once implanted [9]:

- Class A: These biomaterials bonds to hard (bone) and soft (cartilage) tissues [10], they undergo rapid surface reactions, resulting in both osteoconductive and osteoinductive effects [11]. Class A BGs are able to promote the colonization of their surface by osteogenic stem cells directly inside the surgery-derived bone defect that results in the rapid formation of osteoid bridges between particles, followed by the mineralization of the matrix and the formation of mature bone structures [9];
- Class B: These biomaterials bonds only to bone [10], they undergo slower surface reactions and insignificant ionic release, conferring only osteoconduction properties [11], determined exclusively by extracellular factors; a typical example is HAp [9].

1.3.Bioceramics

Ceramics are compounds between metallic and non-metallic elements; most frequently oxides, nitrides, and carbides. Ceramics tend to have a low energy state, which means that they tend to be stable and may well be considered the most chemically and biologically inert of all materials. The wide range of materials that fall within this classification includes ceramics that are composed of clay materials, cement and glass. Unlike metals and polymers, ceramics are

difficult to shear plastically due to the nature of the ionic and covalent bonding holding them together and also the minimum number of slip systems [12].

Ceramics in the form of pottery have been used by humans for thousands of years. In the past properties such as their inherent brittleness, susceptibility to notches or microcracks, low tensile strength, and low impact strength have limited their use. However, within the last 100 years, improvements in the techniques used for the fabrication of ceramics have led to their use as 'high tech' materials. More recently it has been recognized that the characteristic properties of hardness, durability and chemical resistance displayed by ceramics mean that many can withstand the hostile environment within the body. Over the past forty years, ceramics have been specifically designed for the repair and reconstruction of diseased and worn-out body parts. These ceramics are termed 'bioceramics' [12].

Bioceramics are non-toxic can be bioinert, bioactive that is durable material which can undergo interfacial interactions with surrounding tissue, they can be also biodegradable, soluble or resorbable. Sugar and proteins can bind to ceramics. Blood vessels, for example, can penetrate some ceramic prosthetics and bone materials can eventually begin to replace them. Bioceramics fulfill a unique function as biomedical materials, they are available as microspheres, thin layers or coatings metallic implants, porous networks, composites with a polymer component, large well-polished surface [13].

1.3.1. Bioceramics classification

The chemical elements used to manufacture bioceramics form just a small set of the Periodic Table. Namely, bioceramics might be prepared from alumina, zirconia, carbon, silica-contained and calcium-contained compounds, as well as some other chemicals [1]. According to their compositions, the major groups of bioceramics are:

- Oxide ceramics: the major types of oxide ceramics are alumina (Al_2O_3)-based ceramics and zirconia (ZrO_2)-based ceramics. Other simple oxides that have been investigated for use in biomedical applications include $CaO.Al_2O_3$, $CaO.TiO_2$ and $CaO.ZrO_2$.
- Carbons: the main types used for biomedical applications are low temperature isotropic pyrolytic carbon, vitreous (glassy) carbon, diamond-like carbons, carbon fibers, and ultra-low temperature isotropic carbon.
- Glasses: the main glasses used for implantation are SiO_2-CaO-Na_2O-P_2O_5 and Li_2O-ZnO-SiO_2 systems. Many glasses are based on a formula called 45S5, signifying 45

wt% SiO_2 and 5 to 1 molar ratios of CaO and P_2O_5. Glasses with lower molar ratios of CaO to P_2O_5 do not bond to the bone.

- Calcium Phosphate Ceramics: calcium phosphate can be crystallized into various calcium phosphate ceramics depending on the Ca:P ratio, presence of water, impurities, and temperature. Examples of phases formed include tricalcium phosphate (TCP), tetra-calcium phosphate (TTCP) and HAp [12].

A comparison of the relative chemical activity of the different types of bioceramics is shown in Figure 1. The rate of formation of an interfacial bond of bioceramics implants with the bone (Figure 1a) correlates very closely with the relative reactivity shown in Figure 1b. In this work, the focus has been placed upon coatings of HAp and BG as medical implants to repair and reconstruct damaged or diseased hard tissues of the body (usually, those of the musculoskeletal system, such as bones or teeth), therefore, these two biomaterials will be deepened in the following.

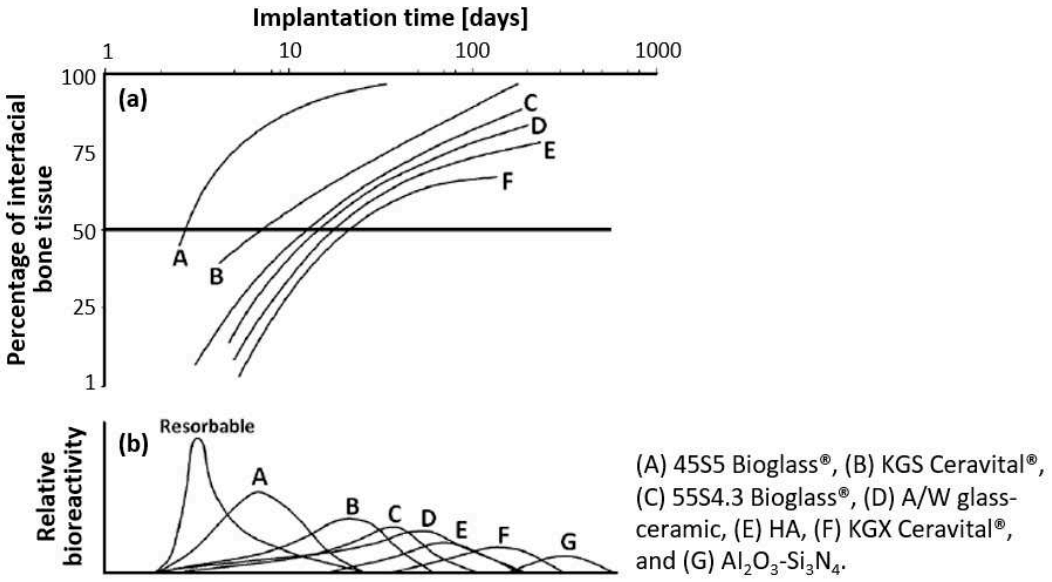

Figure 1. Bioactivity spectrum for various bioceramic implants: (a) time dependence of the formation of bone-bonding at the implant interface, and (b) relative rate of bioreactivity. Adapted from: [14,15].

2. APATITES

Apatite is the generic name, which was first introduced by german geologist A.G. Werner in 1786. These minerals and their synthetic analogs represent a major class of ionic compounds and the most common crystalline form of calcium phosphates. The name "apatite" comes from the Greek spelling "apate" (απαταω) which means deceit. The reason for this was that the mineral appeared in different colors with a variety of crystal habits and was thus often mistaken

for precious minerals such as aquamarine or amethyst. This variation arises from the fact that the apatite structure has a particularly complex solid system. The archetype crystalline structure of apatite is hexagonal with the space group $P6_3/M$ and the unit-cell parameters a = 9.3–9.6 and c = 6.7–6.9 Å. The generic crystal-chemical formula, $M_{10}(ZO_4)_6X_2$, can be also written following equation 2 [16]:

$$^{IX}M(1)_4{}^{VII}M(2)_6[^{IV}ZO(1)O(2)O(3)_2]_6X_2 \quad (2)$$

where left superscripts indicate ideal coordination numbers. M represents large cations, Z represents metal or metalloids and X^- represents anion and each component can be replaced by a large number of different elements or solid states: M = Ca^{2+}, Mg^{2+}, Sr^{2+}, Ba^{2+}, Mn^{2+}, Fe^{2+}, Zn^{2+},Cd^{2+}, Pb^{2+}, Na^+, K^+, Al^{3+}; ZO_4 = PO_4^{3-}, AsO_4^{3-}, VO_4^{3-}, CO_3^{2-}, SO_4^{2-}, SiO_4^{4-}; and X_2 = F^{2-}, Cl^{2-}, Br^{2-}, O^{2-}, $(OH^-)_2$, CO_3^{2-}. M or X may be absent. These minerals have been named fluorapatite, chlorapatite, and hydroxyapatite, depending on the dominant X^- anion or apatite–(CaF), apatite –(CaCl) and apatite –(CaOH) according to the new approved nomenclature scheme by the IMA Commission on New Minerals, Nomenclature, and Classification in 2008 [16,17].

2.2.Apatites classification

The "apatite group" traditionally includes phosphate, arsenate and vanadate minerals. All these minerals and others belonging to different chemical classes with the structural morphology of apatite can be included in the broader apatite supergroup, which can be divided into five groups:

- Apatite group: hexagonal and pseudo-hexagonal phosphates, arsenates and vanadates containing the same prevailing (species-defining) cations at both M(1) and M(2) sites. The most important minerals of the apatite group, with ideal apatite formula $Ca_5(PO_4)_3F$, $Ca_5(PO_4)_3OH$ and $Ca_5(PO_4)_3Cl$, are known as fluorapatite, HAp, and chlorapatite, respectively.
- Hedyphane group: hexagonal and pseudo-hexagonal phosphates, arsenates and sulfates containing different prevailing (species-defining) cations at M(1) and M(2) sites. Some hedyphane minerals are hedyphane, caracolite, and cesanite.
- Belovite group: hexagonal and trigonal phosphates with M(1) site split into the M(1) and M(1′) sites containing different prevailing (species-defining) cations. Some belovite minerals are belovite, deloneite, and fluorcaphite.

- Britholite group: hexagonal and pseudo-hexagonal silicates, typically with partially ordered M(1) and M(2) cations. Some britholite minerals are britholite, melanocerite, and tritomite.
- Ellestadite group: hexagonal and pseudo-hexagonal sulfate-silicates with ideal ratio $[SiO_4]^{4-}$:$[SO_4]^{2-}$ = 1:1. Some ellestadite minerals are ellestadite and mattheddleite.

2.3.Hydroxyapatite (HAp)

The similarity between this calcium phosphate apatite ($Ca_5(PO_4)_3OH$) and the mineral component of bone is reported to have been first suggested in 1788 by Proust and by Klaprota [12]. This was confirmed only after the development and use of x-ray diffraction by Dejong in 1926 [18]. Of the calcium phosphate bioceramics, HAp is the most widely used for orthopedic and dental reconstruction because it is the predominant component of human bone mineral and teeth enamel. It has been used clinically in the form of powders, granules, cement, dense and porous blocks or beads, coatings, and various composites [7].

It was initially used for repair of residual ridge resorption in the 1970s and was first declared as successful implant material in 1988 in the United States [13]. It has been used to form spacers in several shapes e.g. as an iliac bone spacer inserted into the defected iliac bone after an iliac bone is removed as an auto-bone graft. HAp can be filled into bone defects resulting from the removal of bone tumors. It can be used on its own or mixed with autograft bone chips. HAp coatings and HAp composite coatings can be used as coatings on hip and knee replacements. HAp is also used in bioactive bone cement [12].

2.3.1. HAp chemical structure

HAp is generally highly crystalline with the following lattice parameters: (a = 0:942 nm and c = 0:687 nm), it displays a hexagonal symmetry (structural genomics P63/m [16]) with preferred orientation along the c axis and its crystals typically display a needle-like morphology [7]. The HAp calculated density is 3.219 g/cm^3 [12].

The general formula of HAp is $Ca1_4Ca2_6(PO_4)_6(OH)_2$, where Ca1 and Ca2 are two different crystallographic positions for ten calcium atoms. Four of them are situated in the Ca1 position, and they are surrounded by nine oxygen atoms that belong to PO_4 tetrahedra. The other six calcium atoms, which are coordinated by the six O atoms of the PO_4 tetrahedra and by one of the OH^- ions, are placed in the Ca2 site (see Figure 2) [19].

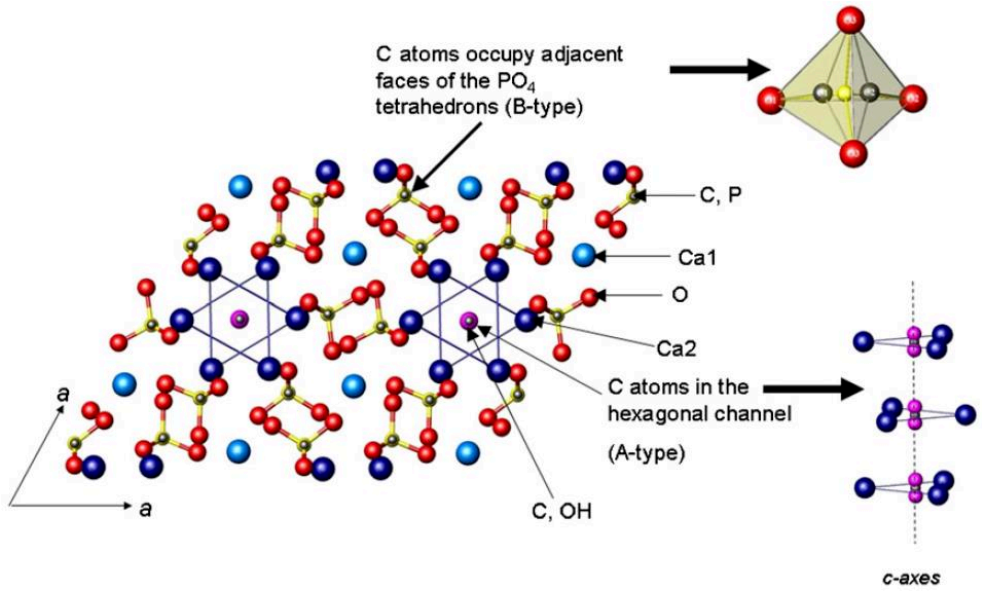

Figure 2. Crystal structure of HAp, showing the possible positions of carbonate ions in the c-direction into the plane of the paper. O—red, Ca1—light blue, Ca2—dark blue, P—yellow, OH^-—pink, C—green. Taken from [19].

The apatite structure is a very hospitable one, allowing the substitutions of many other ions. Substitutions can occur for the (Ca), (PO_4) or (OH) groups. These substitutions result in changes in the properties of the crystal including changes in lattice parameters, morphology, and solubility [12]. Carbonate is the most abundant substitution in bone mineral. According to its crystal position, carbonated apatites are classified as follows: A-type, where CO_3^{2-} ions occupy the OH^- sites; B-type, where CO_3^{2-} ions occupy the PO_4^{3-} sites; and AB-type, where they occupy both OH^- and PO_4^{3-} sites (see Figure 2) [19]. The chemical properties of HAp used for medical applications are regulated by standards. The ISO standard relating to HAp powders, ISO 13779-6: 2015 [20], and ISO standard relating to HAp blocks, ISO 13779-1:2008 [21], state the limits presented in Table 1.

Table 1. Chemical properties required for HAp powders and blocks. Adapted from [20,21].

Requirement	**HAp powder**	**HAp block**	**HAp coating**
Ca/P ratio	1.66-1.71	1.65-1.82	1.67-1.76
Maximum content of heavy metals [mg/kg]	30	50	30
Minimum content of HAp [wt%]	95	50	-
Minimum crystallinity of HAp phase [%]	95	95	-

2.3.2. HAp thermal behavior

There are a number of factors which are believed to control HAp thermal behavior and these include: temperature, hold time, atmosphere (e.g. air, water, vacuum), powder synthesis method, phase purity and Ca/P stoichiometry [7], Figure 3 outlines the processes and reactions involved. At low temperatures (20-200 °C) the first process to occur is de-hydration, absorbed water begins to evaporate and as the temperature is increased the lattice water then starts to evaporate [12]. Between 200 and 800 °C, the heating of unstable species like HPO_4^{2-} and CO_3^{2}, common impurities from the powder synthesis, can lead to several irreversible reactions as shown in Figure 3. At temperatures between 850 and 1000 °C, the formation of mineral phases coexisting with HAp depend only on the Ca/P ratio of the apatite (Figure 3) [22].

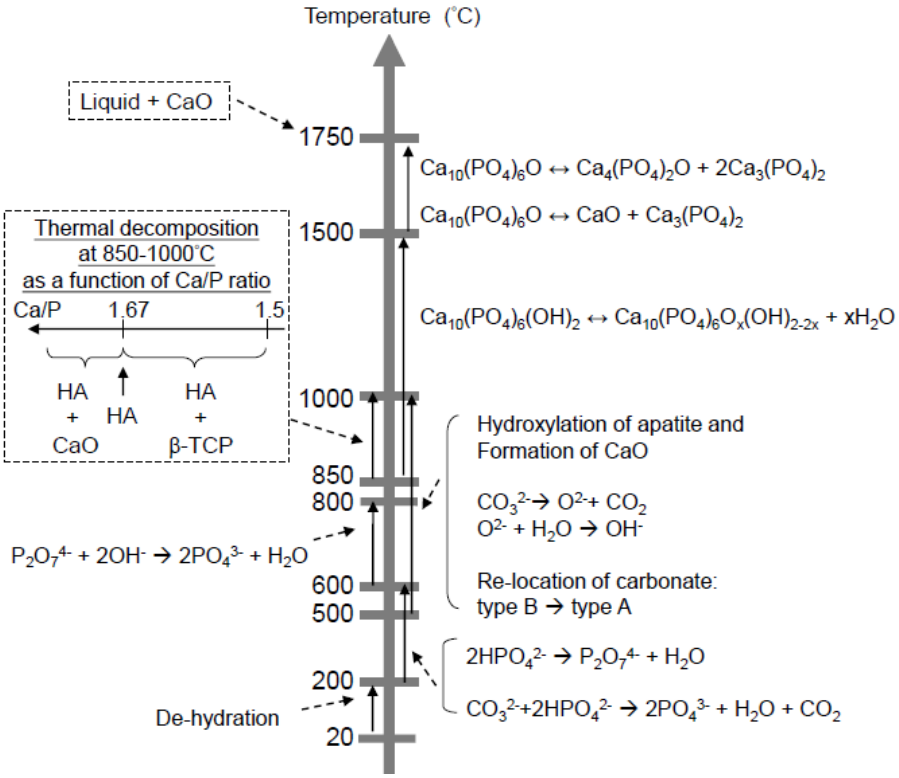

Figure 3. Thermal decomposition of apatite. Reversible and irreversible reactions as functions of temperature. Taken from [22].

Several phase diagrams have been provided for the $CaO-P_2O_5$ system, with water vapor not considered in most cases. However, it is well established that the decomposition of stoichiometric HAp begins with dehydroxylation and the formation of oxyapatite (OAp) related to the loss of water, this reaction is reversible and depends on the water vapor pressure. It seems to begin at about 850 °C in vacuum. Between 1050 °C and 1550 °C, oxy-hydroxyapatite (OHAp) begins to decompose into TCP and TTCP. Various values of this decomposition

temperature, which increases with the water partial pressure, have been reported. At higher temperature (1570 °C), a liquid phase, which is believed to correspond to a eutectic mixture is obtained. However, some reports mention the existence of CaO resulting from the decomposition of HAp within the liquid phase [22].

2.3.3. HAp mechanical properties

The brittle nature of ceramics is attributed to their high strength ionic bonds. Any ceramics, when they fail, tend to do so in a dramatic manner. It is not possible for plastic deformation to happen prior to failure, as a slip cannot occur. From the mechanical point of view, their mechanical properties are governed by crystallinity, grain size, grain boundaries, porosity, and composition. In general, the mechanical properties decrease significantly with increasing content of an amorphous phase, microporosity and grain size, while a high crystallinity, low porosity and small grain size tend to give a higher stiffness, a higher compressive and tensile strength and a greater fracture toughness [1].

HAp is typically sintered to enhance the mechanical properties of HAp bodies. According to ISO 13779-1:2008 (Implants for Surgery – Hydroxyapatite. Part 1: Ceramic Hydroxyapatite [21]), the compressive strength of sintered HAp powder should be not less than 1.5 MPa [12]. Table 2 presents some of the mechanical properties of sintered HAp implants versus natural bone. Only average ranges are given because of the long variations that are often seen amongst data which could be attributed to differences in material properties, as well as the limited sensitivity of the measurements [7].

Table 2. Mechanical properties of bone vs HAp. Adapted from [7].

Material	**Compressive strength [MPa]**	**Tensile strength [MPa]**	**Fracture toughness [MPa/m^2]**	**Elastic modulus [GPa]**	**Vickers Hardness [GPa]**
Dense HAp	120-900	38-300	1	35-120	3-7
Cortical bone	100-230	50-150	2-12	18-22	-

One of the main constraints of HAp is its low fracture toughness compared to the compact cortical bone which means that HAp behaves as a relatively brittle material. The elastic modulus of dense HAp is in a similar range to cortical bone, but dense bulk HAp implants display

mechanical resistance of ~100MPa, which is typically 3x higher for natural bone [7]. Additionally, the Weibull modulus (n) is low in wet environments (n = 5–12) which indicates low reliability of HAp implants [23].

2.3.4. HAp radio-opacity

Bioceramics of poorly dense HAp present incompetently resolved x-ray images, which is a practical problem with respect to immediate and short term post-operative monitoring of bone formation by the clinicians. Hence there is a significant interest in using contrast agents (e.g. bismuth or iodine compounds) having x-ray attenuation capacity to enhance the opacity property of HAp without introducing any secondary changes [24].

One example is the work of M Ageesh et al. [24], where iron oxide nanoparticles were utilized for the fabrication of a phase pure HAp–iron oxide composite with better radio-opacity than pure HAp. The cytotoxicity study unveils that up to 40% of iron oxide (hematite) is not detrimental to the osteoblast cell activity of HAp. Another example is the work of G. Ciobanu et al. [25], where Bi-substituted HAp nano-powder was produced by the co-precipitation method using calcium, phosphorous and bismuth as raw materials. The Bi content close to 10 %. was radio-opaque, being detectable by x-rays and computed tomography. The XPS analysis of the doped sample indicated the Bi presence in the apatite lattice as Bi^{3+}. The XRD results indicate that the Bi substitution did not change the crystal structures.

Table 3 presents the radio-opacity means of enamel, dentine and commercially available calcium hydroxide-based cements with improved radio-opacity. All the cements had radio-opacity greater than dentine ($p < 0.05$) but only Dycal showed a radio-opacity lower than enamel. Hydcal and Liner presented similar or greater radio-opacities than enamel [26].

Table 3. Average radio-opacities (in mmAl) of enamel, dentine and calcium dydroxide cements with 1 mm thickness. Adapted from [26].

Material	**Enamel**	**Dentine**	**Dycal**	**Hydcal**	**Liner**
Radiopacity	2.19 (±0.35)	1.15 (±0.15)	1.55 (±0.13)	2.77 (±0.20)	2.76 (±0.15)

2.3.5. HAp bioactivity

The bioactivity of synthetic HAp is not only suggested by its composition but also by results of in vivo implantation [12]. It belongs to the group of materials that presents a Class B bioactivity

according to the classification made by Hench [9]. In other words, HAp is osteoconductive in a manner similar to that of allograft bone [18]. The biological response to implanted calcium orthophosphates follows a similar cascade observed in fracture healing. This cascade includes hematoma formation, inflammation, neovascularization, osteoclastic resorption and new bone formation [1]. These last interaction processes are deepened in the following sections.

2.3.6. HAp dissolution properties

With few exceptions, dissolution rates of calcium orthophosphates are inversely proportional to the Ca/P ratio, phase purity, and crystalline size, as well as being directly related to the porosity and surface area [1]. The rate of dissolution is also dependent on the type and concentration of the surrounding solution, the pH of the solution, the degree of saturation of the solution, the solid/solution ratio and the length of time for which it is suspended in the solutions. The pH of the solution determines which one is stable [12].

HAp has a low solubility product constant ($K_{sp} = 2.9 \times 10^{-58}$) over a pH range of ~3.5 to ~9.7 [27]. It is the only stable calcium phosphate compound and the least soluble phase under the normal physiologic condition of pH 7.2. This may drop to as low as 5.5 in the region of tissue damage, although this would eventually return to pH 7.2 over a period of time. Even under these conditions, HAp is still the stable phase [13]. Experimental results demonstrated that both the dissolution kinetics and phase transformations to calcium deficient hydroxyapatite (CDHAp) of biologically relevant calcium orthophosphates proceed in the following decreasing order: amorphous calcium phosphate > dicalcium phosphate > TTCP > α-TCP > β-TCP > bovine bone apatite (unsintered) > bovine bone apatite (sintered) > coralline HAp > HAp [1,13].

2.3.7. HAp tissue bonding

It is agreed that the newly formed bone bonds directly to calcium orthophosphates through a carbonated CDHAp layer precipitating at the bone/implant interface when they bond to bone. One hypothesis that briefly describes the bioactivity mechanism of HAp has been proposed recently (Figure 4), which for the first time, describes reasonable surface transformations happening with calcium orthophosphate bioceramics (in that case, HAp) shortly after implantation.

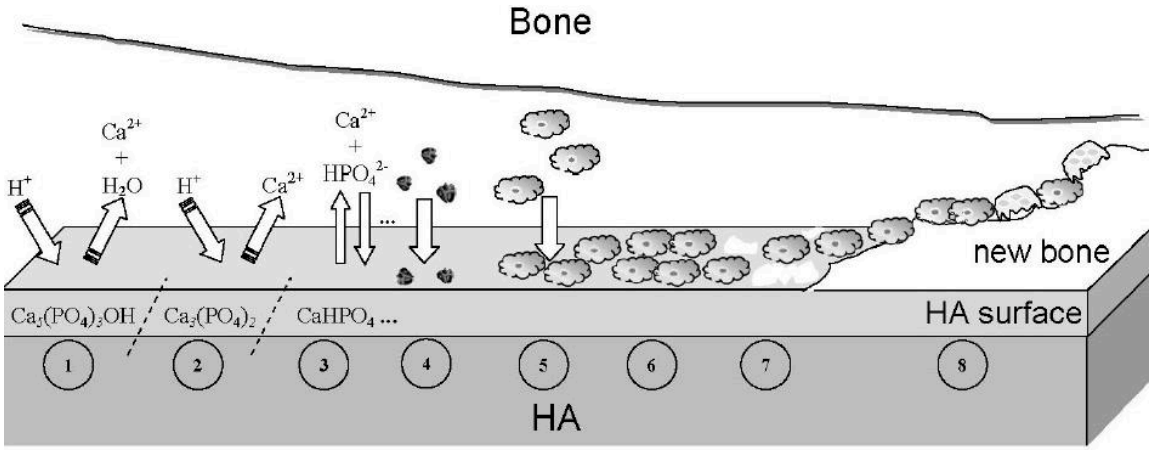

Figure 4. A schematic diagram representing the phenomena that occur on the HAp surface after implantation. Taken from [1].

The bioactive mechanism begins with the implant procedure (1), where solubilization of the HAp surface starts; (2) continuation of the solubilization of the HAp surface; (3) the equilibrium between the physiological solutions and the modified surface of HAp has been achieved (changes in the surface composition of HAp does not mean that a new phase of dicalcium phosphate forms on the surface); (4) adsorption of proteins and/or other bioorganic compounds; (5) cell adhesion; (6) cell proliferation; (7) beginning of a new bone formation; (8) new bone has been formed [1]. Results from plasma spraying of HAp show that bone bonding to HAp coatings is essentially the same as to HAp bulk implants [28].

2.3.8. HAp synthesis methods

The first synthesis of apatite was that of Daubrée in 1851 who obtained HAp by passing phosphorus trichloride vapor over red hot lime [12]. Since then, many diverse methods have claimed to prepare HAp powders with precise control over its chemical, structural and morphological properties. In each method, processing conditions can be varied across a wide range, resulting in several methods [29]. They can be classified into three main pathways [27]:

- Wet chemistry: sources of calcium and phosphate ions are in aqueous solutions in which HAp crystals are congregated by precipitation process. It includes conventional chemical precipitation, sol-gel method, emulsion method, hydrothermal method, hydrolysis method, and sonochemical method. Wet chemistry is advantageous to precisely adjust morphology and size of the particles and it is the most frequently used method for the synthesis of HAp. Particle crystallinity and phase purity, however, are hard to be

controlled in this method and most of the methods are time-consuming because the formation of the HAp phase and the rinsing of unnecessary anions all take time.

- Dry method: the dry method includes solid-state synthesis and a mechanochemical process, which are much less often used than wet chemistry. This method is capable of producing highly crystalline HAp with low-cost raw materials, i.e., eggshells, abalone shells, etc. The size of the synthesized particles could be above the nano-level and the phase purity is even lower than wet chemistry. Heat treatment: this group includes combustion methods (calcination and melting and quenching methods) and pyrolysis method and has the convenience of producing highly crystalline HAp with good chemical homogeneity, at the same time, avoiding an undesirable CaP phase, i.e., octocalcium phosphate. The raw materials are biological waste like bones or shells. However, poor control over the reaction variables and secondary aggregate contamination is usually inevitable [27].

Other methods such as microwave synthesis, spray dry agglomeration route, suspension plasma spraying and high-pressure method or deposition techniques are used much rarely [30–32]. The synthetic HAp has a stoichiometric distribution of its components; for this reason, it does not have the same mineral traces of natural bone. The mineral traces play an important role in the osteointegration process. Therefore, HAp from natural sources, e.g., coral and bovine bone is more similar to human bone tissue. Synthetic HAp, unlike HAp from natural sources, does not have the same behaviors in different applications [33].

2.3.9. HAp natural sources

There are many natural sources for HAp which include extraction of minerals from biowastes, synthesis from eggshells, synthesis from the exoskeleton of marine organisms, synthesis with the aid of natural biomolecules, and synthesis using bio-membranes. The extraction of biominerals from biowastes (mainly bovine bones, fish-scales, and fish bones) is the most well-known method for the preparation of HAp using biogenic sources [29].

One of the most important procedures to obtain pure HAp from biological sources is the biowaste cleaning, which aims to remove organic compounds such as fat and protein and to prevent infections, disease transfer, and immunological defensive reactions. These procedures are calcination, chemical, or thermal treatments. In the case of bovine bones are used as HAp source, the first step in all cases is to cut the bone into smaller pieces and manually remove adhering soft tissue. Thereafter, the fluids in bone, marrow, and any remaining soft tissue are

eliminated by boiling these small pieces of bone in deionized water. The bone is then subjected to drying and a milling process until the powder was fine enough. After that, the fat from the bone is removed with solvents, dried and calcined to eliminate the organic materials without promoting the generation of carbonate phases and to obtain the desirable HAp quality [33].

2.3.10. Biological hydroxyapatite (BHAp)

Bone is a living tissue, which is basically composed of an organic phase (20-30 wt%), an inorganic phase (60-70 wt%) and around 5 wt% of water. The organic matrix is composed mainly of collagen, but there are other compounds in small concentrations, such as lipids and non-collagenous proteins [33]. On the other hand, the main component of the inorganic matrix can be described as calcium phosphates with an apatitic structure and a composition close to HAp [$Ca_{10}(PO_4)_6(OH)_2$, Ca/P=1.67]. Those calcium phosphates also occur as the major crystalline component in pathological calcification such as dental and urinary calculi and stones [12].

Biological apatites are known to be calcium-deficient, about 2 kg of HAp is present in an average-sized person and the stoichiometry of the HAp varies with its location in the human body. Bone apatites contain carbonate (3-8 w/t%), whereas dental enamel contains substantial amounts of fluoride [34]. There are other ions associated with biological apatites that form the minor components of the inorganic matrix such as magnesium, (Mg^{2+}), carbonate, (CO_3^{2-}), sodium, (Na^+), chloride, (Cl^-), potassium (K^+), fluoride (F^-), and acid phosphate, (HPO_4^{2-}). Trace elements include strontium, (Sr^{2+}), barium, (Ba^{2+}), and lead, (Pb^{2+}) [12].

To date, the exact structure of biological apatites remains undefined [12]. But, It may be tentatively represented by that of a Ca-deficient apatite: $Ca_{8.3}(PO_4)_{4.3}(CO_3)_1(HPO_4)_{0.7}(OH,CO_3)_{0.3}$. The main differences with HAp are carbonate and hydrogen phosphate substitution for phosphate and the important amount of cationic and anionic vacancies [35]. When CO_3^{2-} and HPO_4^{2-} ions are added, the Ca/P ratio varies between 1.50 to 1.70, depending on the age and bone site. When bone ages, the Ca/P ratio increases, suggesting that the carbonate species increases [7]. Based on the crystal position of this carbonates, the bone mineral apatite is generally considered to be the B-type and mixed AB-type with an increase of A-type substituted apatite in the old bone; hence, B-type HAp is the most abundant apatite in bones of young people [19].

3. BIOACTIVE GLASSES (BG)

The word "glass" has been traditionally associated with inorganic products of fusion that have been cooled to a rigid condition without crystallizing, a definition that is used in several procedures in glass technology, such as the DIN, ISO, and ASTM standards [36]. In terms of compositional flexibility, glasses have great advantages in comparison to crystalline substances. While crystalline phases possess well-defined and constant stoichiometry, glasses can be synthesized into a virtually unlimited range of compositions, which can be designed to adjust to a specific necessity [11].

Another important difference between glasses and crystalline materials is the existence of the glass transition temperature (T_g) in the former, at which the solid glass becomes a viscous liquid glass. More correctly, T_g is an interval of temperatures that depends significantly on the composition and thermal history of the material (e.g., melting temperature, cooling rate, and the subsequent heat-treatment schedules). Unlike crystalline solids, glasses do not show any long-range order or any significant symmetry in their atomic arrangement. Instead, the atoms constituting the glass are organized in a short-range order that depends on the glass composition, i.e., glass seems to be a liquid, but behaves similar to a solid in human time scales [11]

Among the numerous possibilities of cataloging glasses, natural such as obsidian and amber and synthetic oxide glasses such as bioactive glasses, they can be classified according to their compositional system [11]:

- Silicate glasses: the basic building unit of silicate glasses is the SiO_4 Tetrahedron, which can be connected to up to a maximum of four other tetrahedra through covalent bonds (≡Si–O–Si≡) via its corners.
- Phosphate glasses consist of an inorganic phosphate network of PO_4^{3-} tetrahedral units, with each one connected to a maximum of three other phosphate tetrahedral units through covalent ≡P–O–P≡ bonds.
- Borate glasses: vitreous B_2O_3 consists of planar $BØ_3$ trigonal groups (with Ø corresponding to BO atoms) predominantly grouped in six-membered boroxol rings. B_2O_3 is one of the most important glass-forming oxides due to its higher field strength, lower cation size, small heat of fusion, and trivalent nature of B.
- Mixed glass former systems: many glass compositions are based on more than one former oxide, such as borosilicates, borophosphates, or phosphosilicates, for instance. The

combination of several network formers permits obtaining glasses with specific medleys of physical properties [11].

Some silicate glasses contain B_2O_3 or P_2O_5 in their compositions, but they are not usually considered to be mixed-glass former systems, because the amounts of these oxides are small, or they do not participate as oxide formers in the glass network. That is the case of 45S5 Bioglass®, which is a synthetic silicate-based bioactive glass with components Na_2O, CaO, and P_2O5 [11].

3.1.BG45S5

Some ceramics containing calcium and phosphate ions contain other oxides and form glasses; these ceramics are referred to as bioactive glasses or glass-ceramics but should not be confused with bioactive glasses or with the specific patented ceramic composition known as 45S5 Bioglass® (BG) [28]. BG has been used in more than a million patients to repair bone defects in the jaw and in orthopedics. Used in this way, it dissolves and stimulates natural bone repair (bone regeneration). Its major commercial success is as an active repair agent in tooth-paste, under the name NovaMin® (GlaxoSmithKline, UK). Clinical studies show that the dentifrice can mineralize tiny holes in dentine, reducing tooth sensitivity [37].

The discovery of BG in 1969 at the University of Florida by Professor Larry Hench began after a bus ride conversation with a US Army colonel in 1967 [11]. The colonel challenged Hench with the following: hundreds of limbs a week in Vietnam were being amputated because the body was found to reject the bioinert materials used to repair the body [38], and asked him if materials could be developed that could survive the aggressive environment of the human body [37]. The initial idea of Hench was to combine elements that are abundant in the human body in proportions that favor the rapid initial dissolution of alkalis in aqueous solutions, followed by the precipitation of a Ca-rich and P-rich layer at the inner alkali-depleted silica layer. The Na_2O–CaO–SiO_2 system was selected, with a constant 6 wt%. P_2O_5 content [11]. This work is summarized in the ternary diagram shown in Figure 5. All compositions in region A have a constant 6 wt% of P_2O_5 and A/W glass-ceramic has higher P_2O_5 content [39].

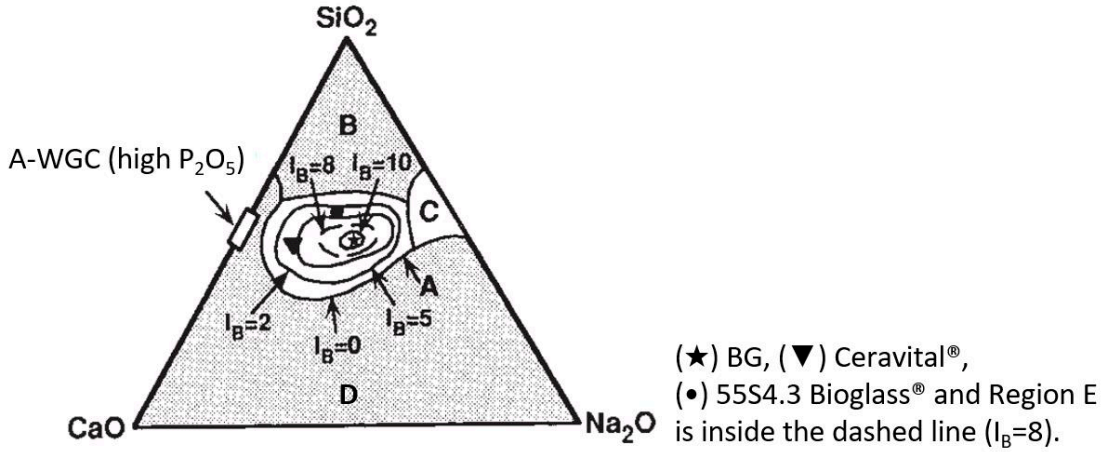

Figure 5. Compositional dependence of bone and soft tissue bonding of bioactive glasses and glass-ceramics. Reproduced from [39].

In region A the glasses are bioactive and bond to the bone. In the middle of this area a smaller region is indicated (region E), within which soft tissue bonding also occurs. Glasses in region B behave as nearly inert materials and are encapsulated by non-adherent fibrous tissue when implanted. Compositions in C region are resorbed within 10 to 30 days in tissue. In region D the compositions are not technically practical and have not been implanted [39]. The main discovery was that a glass of the composition 46.1 mol.% SiO_2, 24.4 mol.% Na_2O, 26.9 mol.% CaO and 2.6 mol.% P_2O_5 ($45SiO_2$–$24.5Na_2O$–$24.5CaO$–$6P_2O_5$ wt. %), termed BG, formed a bond with bone so strong that it could not be removed without breaking the bone [37]. BG was born, and with the first composition studied! [38]. These bioactive glass materials were the first man-made materials that formed a chemical bond with bone [40].

Its discovery changed the paradigm in the biomaterials field, shifting the interest from bioinert to bioactive materials. Such an important finding stimulated interest in pushing this bioactive glass towards the market. Such endeavors culminated with the approval by the Food and Drug Administration (FDA) of the United States of the first BG implant (MEP® implant for middle ear ossicular repair) in 1985 [11]. And launched the field of bioactive ceramics, with many new materials and products being formed from variations on bioactive glasses and also glass–ceramics and ceramics such as synthetic HAp and other calcium phosphates [37]

3.1.1. *BG45S5 chemical structure*

Silicate glasses are a collection of silica tetrahedra connected by –Si–O–Si– bridging oxygen (BO) bonds (see Figure 6). Silicon is, therefore, the glass network-forming atom. Sodium and calcium are network modifiers that disrupt the network by forming non-bridging oxygen (NBO)

bonds such as Si–O^{-} $^{+}$Na bonds. Figure 6 shows a snapshot of a molecular dynamics model of BG. The silica tetrahedron and its associated bonds can be described by Q^n notation, where n is the number of bridging oxygen bonds.

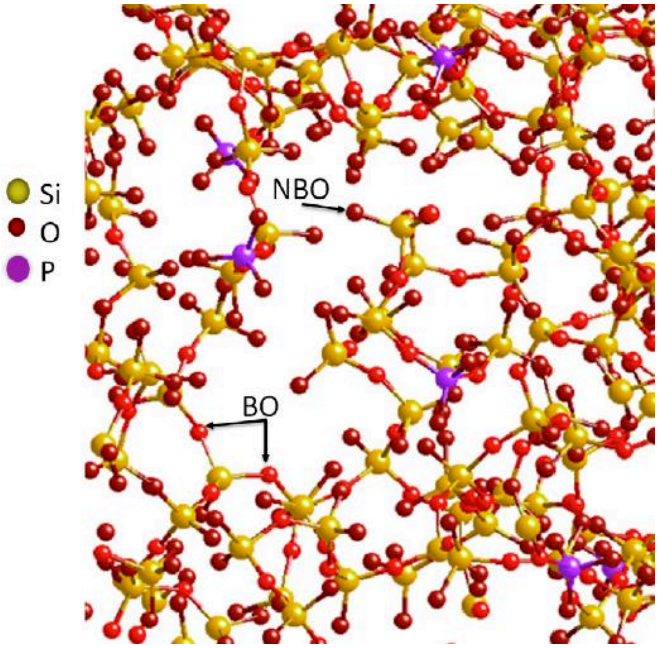

Figure 6. Section of a model of BG, with the Na and Ca ions removed for clarity. Taken from [37].

According to a solid-state NMR study, the phosphorus is present in an orthophosphate environment (Q^0), with charge-balanced by sodium and/or calcium without any P–O–Si bonds. The phosphorus is therefore isolated from the silica network and removes sodium and calcium cations from their network-modifying role. This explains why phosphate is rapidly lost from the glass on exposure to aqueous environments. Molecular dynamics models and XRD data suggest that the distribution of Ca in the glass is non-uniform and suggest the presence of calcium-rich Ca–O regions. The BG calculated density is 2.7 g/cm^3 [37].

Glass network expands when Na_2O is increased and this results in a decrease in density of the glass. Because of this property, Na_2O is referred to as network disrupter. The addition of Na_2O has an effect on T_g because T_g is an expression of network disruption of glass; therefore, T_g is reduced when Na_2O content is increased [41].

3.1.2. BG45S5 thermal behavior

Glass transition temperature (T_g) is a range of transformation when an amorphous solid is changed into a supercooled liquid on heating. Properties like the dissolution rate and strength of different glasses can be compared with the help of T_g. T_g and peak crystallization temperature are two very important properties of glass. A big processing window between these two makes

sure that the glass sinters without crystallization. If a bioactive glass crystallizes, it becomes less bioactive because the ion exchange between the glass and aqueous solution is resisted by the crystalline phase [41]. Table 4 summarizes some thermal properties of BG.

Table 4. Selected properties of melt-derived BG. Adapted from [37,42].

Property	Value
Glass transition temperature [K]	811
The onset of crystallization [K]	950
Crystallization peak [K]	981
Melting point [K]	1450
Thermal expansion coefficient [$°C^{-1}$]	15.1 x 10^{-6}

One reason why BG lacks full commercial success compared to other bioactive ceramics like HAp or TCP is its difficulty to be processed to foams or fibers. This is because BG tends to crystallize during high-temperature treatment above 1000 °C. This leads to poor densification of 45S5 solid bodies and to the formation of microcracks resulting in low mechanical strength of BG-ceramic. Overall the workability of BG is quite poor [42].

3.1.3. BG45S5 mechanical properties

Table 5. Mechanical properties of trabecular and cortical bone compared to BG composition. Adapted from [7,9,10,42].

Property	Cortical bone	BG
Compressive strength [MPa]	100-230	500
Flexural strength [MPa]	-	30-60
Fracture toughness [MPa $m^{1/2}$]	2-12;	0.7-1.1
Tensile strength [MPa]	50-150	42
Elastic modulus [GPa]	7-30	35
Vickers Hardness [HV]	-	600

A linear relationship exists between T_g and hardness of bioactive glass. A decreased T_g of a bioactive glass predicts that the glass has reduced hardness [41]. From an engineering point of view, it is desirable to select the biomaterial taking into account the mechanical parameters of the tissue of concern. Table 5 summarizes the mechanical properties of human cortical bone comparing them to dense BG [9]. The limits in mechanical performances of bulk BG are related to the intrinsic brittleness of glasses and the interconnected and porous structure required in biomedical applications. Mechanical failure could occur both during the surgical implantation of the device and during the post-operatory phase, since the dissolution of the material may lead to the formation of cracks responsible for the breaking of the structure even in under-loading conditions [9].

3.1.4. BG45S5 radio-opacity

The main shortcoming of bioactive glasses is that they have radio-opacity similar to that of cortical bone [43]. Therefore, it is suggested to combine BG with a radio-opacifier to identify it on a radiographic image. In the patent of W. Jan et al.[44], particles of bioactive glass are combined with particles of $BaSO_4$ and melted together to obtain shaped implants. However, it was found that the materials produced according to this method show reduced bioactivity [44]. Table 6 presents the radio-opacity means of enamel, dentine and commercially available glass ionomer cements with improved radio-opacity. Considering all the evaluated thicknesses, Ionomaster and Bioglass F presented radio-opacity lower ($p < 0.05$) or similar to dentine. Riva Sure Cure was more radio-opaque than enamel for all thicknesses ($p < 0.05$) [26].

Table 6. Average radio-opacities in millimeters of aluminium (mmAl) of enamel, dentine and glass ionomer cements with 1 mm, 2 mm and 3 mm thickness. Adapted from [26].

Material	**1 mm**	**2 mm**	**3 mm**
Enamel	2.19 (±0.35)	4.40 (±0.34)	6.55 (±1.34)
Dentine	1.15 (±0.15)	2.33 (±0.41)	3.77 (±1.34)
Ionomaster	0.27 (± 0.04)	1.00 (± 0.00)	1.96 (± 0.26)
Bioglass F	0.66 (±0.14)	2.18 (±0.58)	3.56 (±1.00)
Riva Sure Cure	3.46 (±0.35)	6.65 (±0.42)	9.12 (±0.37)

3.1.5. BG45S5 bioactivity

The biocompatibility of BG powders was deduced from studies carried out both *in-vivo* and *in-vitro* [35]. BG feature remarkable osteoconductive and osteoinductive properties, including the ability to promote angiogenesis and bond to both hard and soft tissues. Due to these interesting features, BG is considered third-generation biomaterials and presents a Class A bioactivity according to the classification made by Hench [11].

All the components of glass composition play specific roles, and their contents have significant effects not only on glass-forming ability but on its biocompatibility. Na_2O acts as an effective fluxing agent, lowering the glass melting temperature and Tg, and increases the dissolution from the glass surface, promoting the formation of a silica-rich layer that is necessary to the deposition of Ca^{2+} and P^{5+} ionic species that lead to the crystallization of the bonding apatite layer. Increasing the content of SiO_2 results in an increase in network connectivity and a decrease in network dissolution and bioactivity. P_2O_5 increased surface reactivity, bioactivity and degradation rate but high concentrations result in adverse effects. For many years, it was assumed that the presence of P_2O_5 in glass compositions was crucial for bioactivity. However, it is now known that some phosphate-free glasses are bioactive [10,11]. Similarly, sol-gel derived bioactive glasses that do not contain Na_2O were more bioactive than melt derived bioactive glasses with the same composition. This, considering that bioactivity is also dependent on the size and volume of the pores in the biomaterial [41].

BG45S5 dissolution properties

The dissolution and the ion release kinetics depend on the glass network structure and the type of ions present in the glass. Glass networks with larger network connectivity (N_c) are slow to dissolve, and vice versa. In the field of bioactive glass research, a parameter called network connectivity is used to study the dependence between the network structure and its dissolution behavior [11]. Network connectivity can be quantified, mean number of bridging oxygen bonds per silicon atom) and used to predict the bioactivity of a glass. In melt-derived glasses, the composition can be used to calculate N_c. The knowledge that the phosphate is in the form of orthophosphate (Q^0 $[PO_4]^{3-}$ units) and not part of the silica network (i.e. no Si–O–P bonds are present) was important for accurate derivation of the equation 3 [37]:

$$N_c = \frac{4[SiO_2] - 2[M_2^I O + M^{II} O] + 6[P_2O_5]}{[SiO_2]} \quad (3)$$

This calculates BG to have an N_c of 2.12. Glasses that have N_c greater than 2.6 are likely not to be bioactive due to their resistance to dissolution [37]. For the optimal balance between the dissolution and degradation of bioactive glasses, $N_c = 2$ is preferred [11].

BG45S5 tissue bonding

The bioactivity mechanism first proposed by Hench and still accepted for silicate BGs is based on 11 reaction stages [9]: (1) rapid cation exchange of Na^+ and/or $Ca2^+$ with H^+ from solution, creating silanol bonds (Si-OH) on the glass surface. The pH of the solution increases and a silica-rich (cation-depleted) region forms near the glass surface. Phosphate is also lost from the glass; (2) high local pH leads to the attack of the silica glass network by OH^-, breaking Si–O–Si bonds. Soluble silica is lost in the form of $Si(OH)_4$ to the solution, leaving more Si–OH (silanols) at the glass–solution interface; (3) condensation of Si–OH groups near the glass surface: repolymerization of the silica-rich layer; (4) migration of $Ca2^+$ and PO_4^{3-} groups to the surface through the silica-rich layer and from the solution, forming a film rich in amorphous $CaO–P_2O_5$ on the silica-rich layer; (5) incorporation of hydroxyls and carbonate from solution and crystallization of the $CaO–P_2O_5$ film to HCA [37]; (6) reaction layers enhance adsorption and desorption of biological moeties, growth factors, proteins, etc.; (7) macrophages prepare the implant site for tissue repair; (8) attachment of stem cells; (9) synchronized proliferation and differentiation of cells rapidly occurs on the surface of BG (several weeks are required for similar cellular events to occur on the surface of bio-inert and Class B bioactive materials); (10) attachment of osteoprogenitor cells, cells colonize the surface of BG within 24-48 hours and begin production of various growth factors which stimulate cell division, mitosis, and production of extracellular matrix proteins (this stage only occurs on Class A biomaterials); and (11) mineralization of the matrix follows soon thereafter and mature osteocytes, encased in a collagen-CDHAp matrix, are the final product after 6-12 days in vitro and in vivo [10].

The thickness of the bonding zone between a bioactive implant and bone is proportional to its bioactivity index (I_B) [10]. This strong bonding layer is 100–200 µm thick in BG, which is roughly 100 times the thickness of a comparable layer formed by HAp [13].

3.1.6. BG45S5 synthesis methods

Glasses are usually processed through two principal methods: melt-quenching and sol-gel processes. In the melt-quenching process, the batch is heated at high temperatures (usually >1300 °C), e.g. in a furnace or in a spray process, and quenched to freeze the disordered atomic structure of the melt to get an amorphous glass. In most cases, the glass is heat-treated at lower

temperatures in order to relax the thermomechanical stresses in the structure induced by rapid cooling. The sol-gel process uses inorganic or organic precursors, which are subjected to different processes of hydrolysis and condensation, followed by drying and thermal stabilization heat treatments; through this process, glass can be shaped into powder, nanoparticles, fibers, coatings, etc. [11].

The main advantages of the gel-derived glasses over melt-derived glasses are: lower temperatures are required for their synthesis, easy powder technology production, improved homogeneity, and purity of the powder, wider range of bioactive compositions with increased bioactivity of compositions up to 90 mol % SiO2 due to their structure, they exhibit mesoporosity and ability to form macroporous structures (scaffolds) [45]. Despite these drawbacks mentioned above the melting route was chosen for glass fabrication used in this study which exhibits advantages like easily controllable chemistry of the glass, low costs of the precursor materials, short processing times, large outcome (amounts) and shorter processing times [42].

Melting and fast quenching method

Currently, the US Food and Drug Administration (FDA) approved melt-derived glass compositions 45S5. As the final application is clinical usage, a careful standardization of the process is needed, and high-purity reagents must be used in order to avoid contamination. The melting process of components is carried out at elevated temperatures (typically 1200 °C < T < 1550 °C) using electrical furnaces. Platinum-covered crucibles are often used for limiting the loss of boron, phosphorous, and fluorine that tend to vaporize during high-temperature thermal treatments. The time required for the melting (T_m) varies according to the size of the batches and generally, in laboratory experimental practice, 1 h < T_m < 24 h.

The available forming routes, according to the final product, are direct forming via casting into molds, quenching into water, or drawing into continuous fiber; or thermally treating the glass above T_g in order to allow the sintering of particles into a porous architecture, drawing of fibers from a pre-form, or sealing particles to obtain coatings on a surface. For the annealing, the thermal treatment is carried out in order to eliminate residual stresses originated by the cooling process after forming.

The homogeneous size of powders and granules is obtained by grinding and sifting the glass. During this procedure, it is possible to have some equipment-derived contamination. Crystallization is a critical aspect when considering the compositional range of BGs as thermal

treatments. However, it is possible to opportunely design the process parameters by studying accurately the crystallization dynamics of the system in order to obtain bioactive glass-ceramic materials with specific properties.

The nature of the process means that it is possible the incorporation of doping oxides in trace amounts (e.g., Cu, Sr, Ag, Co, Zn, Bi, etc.). The incorporation of low concentrations of different ions is important to produce new functional materials with specific physical and functional properties, e.g. with radio-opacity properties [11,37].

4. RADIO-OPAQUE MATERIALS

X-rays Since the discovery of the by Wilhelm C. Röntgen in 1895 has been used extensively in both medical and nonmedical applications [46]. Medical radiographic imaging uses x-rays to obtain an image of a particular structure or function of the human body [47]. A radio-opaque material is a material with a high radio-opacity, which prevents the passage of electromagnetic radiation, is a strong absorber of x-rays and causes a radiographic image to be light [48]. As a rule, materials possessing high densities (ρ) and high atomic numbers (Z) absorb x-rays better. The x-ray absorption coefficient (μ) (see equation 4) expresses the relationship between the x-ray absorption phenomenon and atomic number [49],

$$\mu = \frac{\rho Z^4}{AE^3} \tag{4}$$

where A is the atomic mass of the element and E is the incident x-ray energy. Because Z is raised to the fourth power, a small increase in Z will result in a significant increase in μ. Thus, materials containing heavier elements have greater μ, which allows for greater x-ray attenuation, improves the quality of the radiographic images and facilitates the process of distinguishing regions of interest [49]. While, soft tissues (such as fatty tissues, muscles, and neoplastic tissues) or soft materials consisting of hydrocarbon structures are not very sensitive to x-rays and it is difficult to obtain high-quality images of soft tissues and soft structures [46]. Materials with low densities are weak absorbers and are referred to as radio-lucent [48].

Darkening of the radiographic image occurs at points that correspond with interactions with x-rays. The image appears lighter at points associated with fewer collisions. Darker aspects are radio-lucent, and lighter aspects are radio-opaque. Variations of radio-lucency and radio-opacity create image contrast [47].

The ideal radio-opacity for base and liner materials has been discussed by several authors. Studies of radio-opacity are usually evaluated and compared with enamel, dentine or aluminum

(Al). The International Standards Organization (ISO) has developed standards for the radio-opacity of dental materials. According to ISO 99177 (glass ionomer cements), if a manufacturer claims their product to be radio-opaque, its radio-opacity must be equal to or greater than that of Al with the same thickness and should not be less than 0.5 mm of any value claimed by the manufacturer [26,50]. The ISO 6876:200116 (endodontic cements) establishes 3 mm Al as the minimum radio-opacity value [51]. On the other hand, some research, suggests that the radio-opacity of material should be moderate, slightly exceeding that of the enamel, the latter due to the fact that the detection of secondary caries lesions excessively radio-opaque materials could be difficult due to a masking effect [52].

In dental and orthopedic applications, radio-opaque materials may be used as fillers in the composition of the bio-cement paste in order to enhance the absorption of x-rays, and therefore for improving the visibility of the cement under x-ray examination [25]. In vertebroplasty, the non-resorbable acrylic bone cements contain barium sulfate [53].

4.1. Radiopacity

The term “Radio-opacity' (or “radio-opacity') is described in the ISO 6876:200116 as the relative inability of electromagnetism, such as x-rays, to pass through a given material. Thus, the term refers to the relative opaque white appearance in radiographic imaging, when passing electromagnetic radiation, such as x-rays, through matter [44]. This is mainly due to factors of the material such as thickness, density or the atomic number of its constituent elements and factors of radiographic equipment such as X-rays powers [52].

When x-rays pass through an object, the beam is absorbed or deflected by the object. Such a mechanism is called x-ray attenuation [46]. The following three outcomes can occur for each photon [47]:

- The photoelectric effect occurs when an x-ray photon of higher energy than the k-/l-edge energy of the target transfers all of its energy to an inter-shell electron, causing the photon to cease to exist [54]. The excited atom ejects an electron (photoelectron) and is left in an ionized state, but the photoelectron is not able to emerge from the target.
- Compton scattering: a portion of the incident photon’s energy is absorbed by an electron, a lower-energy photon continues via a deflected path (i.e., scatters), and the electron is ejected from the atom (ionization) but is not able to emerge from the target.

- No interaction: the photon completely penetrates the target without deviation of energy or trajectory [47].

In general, the contrast in medical radiographic imaging improves as the ratio of photoelectric to Compton interactions increases. Most important for the radio-opaque material, therefore, is the close accordance of its K-edge with the mean x-ray photon energy to maximize the photoelectric attenuation of x-ray photons and the radio-opaque effect. Although the typical x-ray beam comprises a spectrum of photon energies (poly-chromatic), it can be adjusted to maximize photon energy near or just above the K-edge of the radio-opaque material. The K-edge value of 37 keV for barium and 33 keV for iodine accords well with the range of x-ray photon energies used in radiography [47].

4.2.Radiopaque materials classification

Typically, radio-opacifiers are selected from the group consisting of metals, metal oxides or metal salts, such as W, TaO_2 or Ta_2O_5, Ag or AgO, Bi_2O_3, Ho or Ho_2O_3, Nb_2O_5, Fe or FeO or Fe_2O_3 or Fe_3O_4, Ti or TiO_2, BaO or $BaSO_4$, Al_2O_3, SrO and ZrO_2 [44]. Among them, barium sulfate suspensions (Z_{Ba} = 56, for gastrointestinal tract imaging) and small, water-soluble iodinated molecules (Z_I = 53, for vascular imaging) are approved for human use in small doses [49]. The use of barium and iodine as x-ray radio-opaque agents is mostly based on historical reasons [49], however, there are reports in the literature about the negative biological response of some of the radio-opacifiers mentioned above. Iodinated molecules, $BaSO_4$ and ZrO_2 have been shown to evoke a significant pathological response both in vitro and in vivo compared to the one without any of these agents [24,55]. Whereby, for example, $BaSO_4$ can only be used in pre-clinical studies and in particular, in angiography of small animals, due to its toxicity [56]. Another disadvantage associated with the addition of $BaSO_4$ suspensions and water-soluble iodinated molecules is that its x-ray attenuation is far from optimal [49].

Gold (Au), platinum (Pt), thallium (Ta), and bismuth (Bi) have been recently used as contrast agents instead of traditional agents that lead to adverse effects in patients Among these elements, Bi possesses the largest x-ray attenuation coefficient (Bi: 5.74, Au: 5.16, Pt: 4.99, and Ta: 4.3 $cm^2\ g^{-1}$ at 100 keV) and highest atom number (Bi: 83, Au: 79, Pt: 78, Ta: 72), making it an ideal element as contrast agent [55]. Bi-based radio-opacifiers, such as BiOI, BiOCl, Bi_2Se_3, Bi_2S_3, Bi_2O_3, and Cu_3BiS_3, have exhibited radiographic imaging ability. However, pure Bi radio-opacifiers are a better choice to maximize the efficiency in x-ray absorption due to the 100% content of Bi element compared with other Bi-based materials

(56.8% for BiOI, 63.8% for Bi_2Se_3, 81.3% for Bi_2S_3, and 89.7% for Bi_2O_3). However, free Bi^{3+} has presented some cytotoxicity compared with Bi-based materials at the same doses [55].

Besides having a high atomic number, Bi-based materials have been used for a number of drugs and cosmetic formulation, and its safety has been extensively evaluated and verified [49]. The work presented by S. Baroth et al. [53] evidence the advantages of using Bi-based radio-opacifiers. Implants were obtained by sintering mixtures of Bi_2O_3, Lu_2O_3 or $GdPO_4$ (20 wt. %) with Ca-deficient apatite (80 wt. %). The composites with Bi_2O_3 presented the best radiographic contrast intensity when comparing to the bone environment. Other results of the work are crystallographic, histological and surface observations about the crystal shape, crystal size and micro-porosity of the composites [53]:

- XRD diagrams show some new crystalline phases when comparing radio-pacifiers and apatites alone and the composite sintered. Possible element substitutions as Ba, Bi, Lu, Gd/Ca or SO_4/PO_4 could be expected.
- Composites implanted with $GdPO_4$ have the most important bone ingrowth when comparing to composites with Bi_2O_3 and Lu_2O_3.
- With the addition of Bi_2O_3, crystals grow in needle shape with an important micro-porosity. With Lu_2O_3 and $GdPO_4$, the micro-porosity is important with small crystals and numbers of fragments are present on the matrix of the composite with Lu_2O_3 [53].

The amount of radio-opacifier may be varied in a broad range and may be determined by routine experiments. For the uses as outlined below, an effective amount of radio-opacifier must be included in the primary particle; typically, such amount is 50 wt. % or less of the primary particle. Suitable are, for example, 5-50 wt. %, even an amount as low as 25-40 wt. % provides a high degree of radio-opacity. In the work of W. Stark et al. [44], it was surprisingly found that mixing mechanically 50 wt. % of a radio-opacifier (such as Bi_2O_3) into bioactive glass shows less radio-opacity than adding 50 wt. % of Bi_2O_3 by the flame spray synthesis. Further, the homogeneity is improved [44].

4.3.Bismuth oxide

Bismuth oxide (Bi_2O_3), an important metal oxide semiconductor has been receiving considerable attention because it exhibits excellent optical and electrical properties such as wide band-gap, high refractive index, high dielectric permittivity and good photocatalytic activity [57], after the pioneering era of titania (TiO_2) [58]. Moreover, due to its radio-opacity and unusual properties of good biocompatibility, despite being a heavy element, bismuth

compounds are object of intense investigations in diagnostic medicine as radiolabeled nanoparticles for cancer therapy, target organ imaging and x-ray computed tomography, for its better performances with respect to iodine, and are added to various bone and dental implants, catheters and surgical instruments in order to make them detectable by x-rays [25,58].

Bismuth and its compounds have a relatively low cost and ease of supply [58]. Bi_2O_3 is commercially made from bismuth subnitrate. The latter is produced by dissolving bismuth in hot nitric acid. The addition of excess sodium hydroxide followed by continuous heating of the mixture precipitates Bi_2O_3 as a heavy yellow powder [59].

4.3.1. Bi_2O_3 Crystallography

Bi_2O_3 is a complex system with four main polymorphs: α, δ, β, and γ [57]. Table 7 shows the characteristic data and transformation temperatures for the different phases of Bi_2O_3 (above 824 ° C the system is in a liquid state) [60].

Table 7. Structural data of the Bi_2O_3 phases. Adapted from [60].

Phase	**α**	**δ**	**β**	**γ**
Stability range (°C)	<729	729-824	330-650	500-639
Structure	monoclinic	fcc	tetragonal	bcc
a (nm)	0.58496	0.56595	0.7738	1.0268
b (nm)	0.81648	-	-	-
c (nm)	0.75101	-	0.5731	-
β´ (°)	112.977	-	-	-

4.3.2. Bi_2O_3 Radiopacity

Bi_2O_3 is a necessary radio-opacifier to enable a radiographic assessment of dental materials because the bismuth has a high atomic number (Z = 83) and good x-ray attenuating properties (absorption edge k = 91) [61,62]. Mineral trioxide aggregate (MTA) is a material that was developed at the University of Loma Linda in the 1990s as a root-end filling material [63]. MTA consists of 75 wt. % Portland cement, 20 wt. % Bi_2O_3, and 5 wt. % calcium sulfate as a setting modifier. It received acceptance by the US Food and Drug Administration and became commercially available as ProRoot MTA (Tulsa Dental, Tulsa, OK) [64]. Figure 7 presents the

relative radio-opacity of some materials with improved radio-opacity in comparison with an aluminum step wedge showing the mean and the standard deviation (n = 3) in mm aluminum equivalents (y-axis).

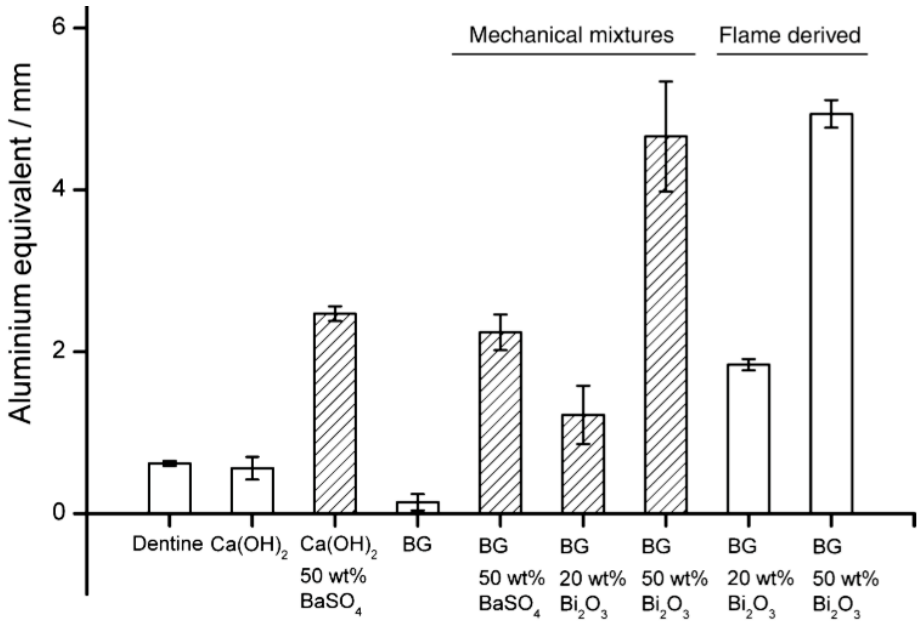

Figure 7. Radio-opacity means of some BG-Bi_2O_3 samples. Adapted from [56].

4.3.3. Bi_2O_3 Biocompatibility

Bi, like heavy metal, is stable to both dry and moist air at ordinary temperatures and has unusually low toxicity. Since the late 18th century, Bi-based compounds, have been used in medicine for the treatment of various gastrointestinal diseases, such as gastritis, dyspepsia, ulcers and H. pylori infection. Moreover, these compounds have been also used as antimicrobial and antileishmanial agents. Recently, inorganic Bi-based materials, as the emerging antitumor agents, have been used for cancer diagnosis and therapy due to their unique physical and chemical properties [55].

For example, as-prepared HA-Bi_2O_3 particles have revealed favorable solubility in water and excellent biocompatibility confirming its series of biological and chemical effects. Furthermore, the heavy metal-based HA-Bi_2O_3 particles could be effectively excreted throughout the renal clearance, reflecting low toxicity [65]. And, suitable physical and biologic properties have been associated with MTA, such as good tolerability in contact with bone and conjunctive tissues, low cytotoxicity and genotoxicity, good sealing ability and antimicrobial action [63]. Nevertheless, it has been shown that modification of bioactive glass showed smaller

and less apparent hydroxyapatite structures compared to the pure bioactive glass after immersion in SBF, which can be an indicator of the slower formation. The bioactive glass containing 50 wt. % bismuth oxide showed considerably less apatite, suggesting that this content is probably the limit for radio-opacifier addition without losing the favored properties [66].

5. THERMAL SPRAY

The coatings contribute to the solution of the needs of different industries, either as thin films (less than 25 μm thick) or thick layers (25 μm to the order of mm), since they offer different functions to those of the coated material (substrate). Broadly speaking, there are four different techniques for depositing coatings. The first allows obtaining thin films, the second both thin films and thick layers and the last two thick layers. Historically speaking, flame spraying has been the first thermal spray technique to be developed, when Maximilian Ulrich Schoop melted metal into a crucible and sprayed it, by means of compressed gas, onto a surface in Switzerland in 1909 [67].

The central part of a thermal spray system is a torch, which converts the supplied energy into a stream of heated gases. The coating material is heated, eventually melted, and accelerated by this high-temperature, high-velocity gas stream toward a substrate, where the particle/ droplet deforms to generate a splat, and where multiple layered splats from the coating [67].

5.2.Thermal spray processes

Currently, a classification of the available techniques responds to the way in which energy or heat is provided to melt the material or give it the plasticity necessary to allow the formation of the coating. The first category corresponds to the techniques in which energy or heat is provided by combustion, the second by the dissipation of electrical energy creating plasma and the third is the case of cold spray where energy is supplied by high-pressure gases. A second level for cataloging the processes is according to the form in which the coating material is introduced, as powder, suspension, solution, wires, or rods [67].

The most commonly used thermal spray techniques are: flame spraying, wire arc spraying, suspension spraying, APS and high-velocity oxy-fuel (HVOF) spraying [68]. Table 8 summarizes the different properties of the major thermal spray techniques.

Table 8. Characteristics of some thermal spray systems. Taken from [69].

System	Process temperature [ºC]	Particle velocity [m/s]	Anchoring force [MPa]	Coating porosity [%]	Oxides content [% wt.]
Combustion	□ 3.800	30 - 70	10 - 30	7 - 15	7 - 10
Arc spraying	4.000	150 - 300	25 - 50	3 - 6	5 - 10
Plasma spraying	□ 10.000	400 - 600	35 - 70	0,5 - 3	0,5 - 3
H.V.O.F./ D-gun	3.100	600 - 1000	50 - □ 70	0,5 - 2	0,5 - 3

The main advantages of APS technique, in which this work is based, are: high particle velocity, resulting in high bond strength and a high density of the coatings; the heat source due to the dissociation and ionization processes is very efficient, which produces an effective heating of the particle; the heat source is inert, minimizing oxidation or carbonation; and the high plasma temperature allows the deposition of materials with high melting points. Some disadvantages of the technique are: the consistency and uniformity of the coating composition over a large surface area may vary; the spraying tends to produce porous coatings, especially when used at high particle velocities; and the coatings may contain oxidation products, together with some porosity due to incomplete fusion [69].

In the following sections, the APS technique will be described, and briefly the HVOF technique, which was used in this work for comparative purposes.

5.3.HVOF Thermal spraying

The technique known as HVOF was developed by Browning and Witfield using rocket engine technologies in the USA in the early 1980s [67]. The principle is the same as explained above, with the particularity that this uses mostly powders as precursor material [70]. To increase the velocity and temperature of the particles to be deposited a combustion process is carried out, in the case of this work, of propane (C_3H_8) with oxygen (O_2) as an oxidizer.

Different values of velocity and temperature can be obtained through the control of the pressures and flows of these two gases that make this process one of the ideal to deposit material by thermal spraying at low temperatures (3100 ° C) and high velocities (up to 2200 m/s), which

is to say about Mach 2 when considering the local pressure and temperature [67]. It is important to know the energy characteristics of the flame generated in the process. The fuel/oxygen ratio (F/O) gives us some information on the temperatures that can be reached, and it is relevant to know if it is rich in fuel or oxidizer to explain the phenomena related to the chemistry of the process. The calculation of the stoichiometric ratio of these reagents in the thermal spray process is presented in equation 5, which takes into account the gases used and the oxygen present in the environment, which represents 21% of the volume of the air [71].

$$\gamma = \frac{Fuel\ flow}{O_2\ flow + 0.21 \times air\ flow} \tag{5}$$

5.4.Plasma spraying

The plasma spray technique had its origin in Germany, in the 20s, however, it was only until the late 50s, when the process began to be widely used. Since 1970, the plasma spray technique has undergone a deep evolution, despite this, the design of the torch used for spraying has hardly undergone modifications [69]. The variations of this technique are based on the environment in which the deposit is carried out (vacuum, low or atmospheric pressure) and the way in which the electric discharge is supplied (direct current or high-frequency RF) [67].

The plasma spraying system consists of a plasma torch that contains a conical cathode inside a cylindrical anode, which extends beyond the cathode forming a nozzle at its end (see Figure 8). In addition to the circulation of water for cooling the electrodes, gases that are involved in the formation of plasma circulate through the gun, primary (usually Ar) and secondary (H_2 or He) gases, which ionize forming the plasma when an electric arc is held between the electrodes with the passage of a current of high intensity and voltage (approximately 50 V); the temperatures and velocities reached by the plasma in the nozzle are up to 15,000 °C and 600 m/s. The feedstock powder is transported by means of carrier gas and injected into the plasma flame, the powder injector may be located inside or outside the nozzle and radial or parallel to the jet axis. The plasma flame accelerates the injected powder particles and melts them due to its high temperature. When a drop of molten material collides with the substrate, the substrate acts as a heat sink; a solidification front then extends towards the outer part of the formed layer, originating a kind of solidified material mound through which the rest of the material flows until all of it hardens, creating a characteristic protuberance. Successive particles join together and cover all irregularities of the substrate with the projected material [69].

The microstructure of the coatings consist of the projected material, which is presented in the form of lamellae or semi-molten particles, and defects in the form of globular and irregular pores, due to the entrapment of air, and cracks by the residual stresses, due to the crystal phase changes and cooling. The surface finish of the thermally sprayed coatings has high roughness (around 10 µm).

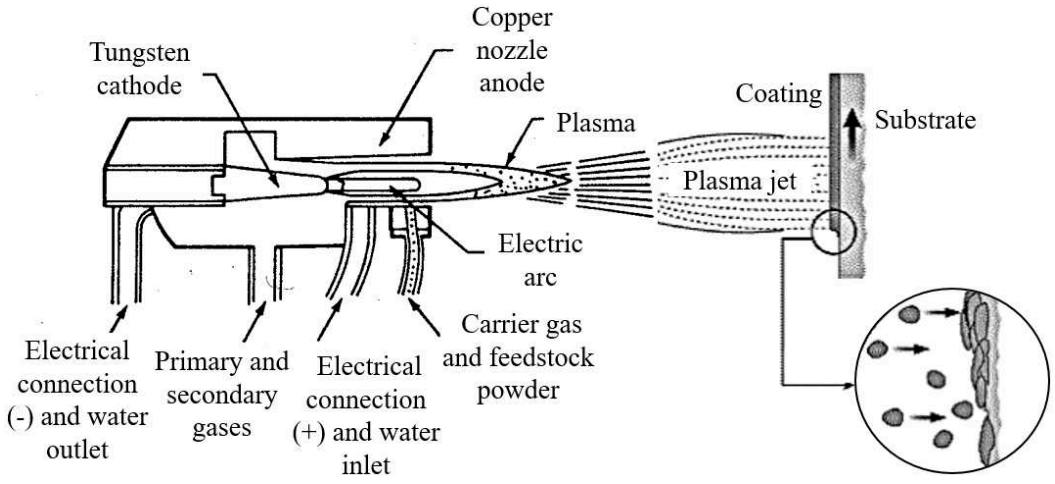

Figure 8. Scheme of an APS process. Adapted from [69,72].

The composition and the structure of the coating are significantly modified from the feedstock powders. Therefore, from a materials-science perspective, the performance of the coating need not necessarily reflect the exact characteristics of the feedstock. When different spray parameters are employed, such as gas combination and flow rate, spray power, and stand-off distance, this modification will be different. Even before it is sprayed, the feedstock powders can be varied in terms of particle morphology, size distribution, microstructure, and density. The substrate type and surface texture are other variables that influence the formation and performance of the coating. Therefore, the overall quality of the HAp coating is a combined outcome of feedstock powders, implant metals, and spray parameters [34]:

- Plasma-forming gases: in practice, argon or nitrogen are the primary gases used, together with additions that vary between 5% and 25%, of a secondary gas, usually hydrogen or helium. These secondary gases such as hydrogen achieve great energy due to the dissociation of their molecules, which, together with the ionization energy, causes the calorific content of the plasma. However, the percentage limitation of these is due to the negative effect they have on the erosion of the electrodes.
- Powder particle size: for each coating material and for each plasma torch there is an adequate size of powder particles, ranging from 5 to 60 µm. A size larger than adequate could cause the particles not to melt, whereby they could separate from the flame or

bounce on the substrate without adhering to it. On the contrary, a smaller than adequate size can cause the vaporization of the particles.

- Powder injection mode: the way in which the particles enter the plasma determines their fusion and subsequent deposition. The pressure of the carrier gas must be conveniently adjusted so that the particles reach the plasma, but they do not go through it. The required gas flow is determined based on the diameter of the transport hose, the density of the powder, the size, and morphology of the particles and the velocity and density of the carrier gas.
- Standoff distance: as the process is at atmospheric pressure, the powder particles will begin to cool and decelerate when they hit the air molecules, once they have left the plasma flame. Therefore, a basic factor to consider is the distance between the torch nozzle and the substrate, which usually ranges between 5 and 10 cm. The effectiveness of the process changes according to the standoff distance [69,73].
- Particle velocity: larger powder particles have a slower response to the acceleration printed by the gas, and once accelerated, those particles lose speed more slowly than the gas itself. The variation of the plasma and particle velocities as a function of the standoff distance is presented in Figure 9 [67].
- Particle-substrate interaction: when molten particles collide with the substrate, such substrate must have been previously subjected to a cleaning and surface finishing process that confers some roughness to increase the adhesion of the coating. These particles solidify and cover all irregularities of the substrate with the sprayed material.
- Protection atmosphere: due to the protective effect of the inert beam of the plasma and the short periods of stay of the particles in the plasma, the possibilities of the reaction of the dust with the air are quite limited [69].

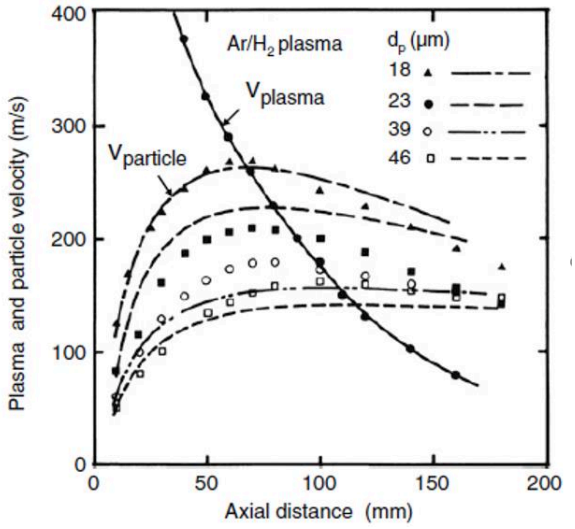

Figure 9. Typical axial plasma and particle velocities for an argon-hydrogen plasma jet. Taken from [67].

5.5.BHAp and BG thermally sprayed coatings by APS and HVOF

It is well known that HAp decomposes at around 1800 K in secondary phases such as amorphous calcium phosphate (ACP), tricalcium phosphate (TCP), tetracalcium phosphate (TTCP) and octacalcium phosphate (OCP) [74,75]. Additionally, the formation of these secondary phases reduces the environmental stability, biocompatibility and mechanical performance of the APS HAp coating [76–79]. Nevertheless, these coatings still represent a favorable biomedical application considering its biocorrosion resistance, fabrication efficiency, and positive clinical performance in weight-bearing or non-weight-bearing implants [34,80,81]. On the other hand, it has been claimed that High-Velocity Oxygen Fuel (HVOF) is an alternative thermal spray technique to overcome high-temperature issues related to HAp deposition by APS [82,83]. In HVOF, the combustion of the fuel with oxygen at high pressure creates a supersonic flame that allows projecting material at high velocity. In contrast to APS, the temperature in HVOF is considerably lower and HAp in-flight particles are deposited between 1480 K and 2172 K [84]. Thus, the obtained coatings have a lower content of secondary phases [85] and enhanced mechanical and biocompatible properties [82,86]. Despite this, HAp coatings deposited by APS still exhibit higher adherence than HVOF coatings [87].
Biological HAp has been barely used as a feedstock material in thermal spray processing. Thus, there is a lack of information about its behavior in thermal spray deposition due to the variable composition of BHAp, its structural deformations, etc. making the analysis in coatings rather complex. For instance, L. S. Ozyegin et al. and G. Goller et al. have already reported the study of bovine and human-derived HAp coatings deposited by thermal spray [88,89]. In their remarks, they evaluated the feasibility of obtaining bovine and human-derived HAp coatings

by APS with adequate bond strength. These coatings showed high decompositions due to the APS deposition temperatures and no bioactivity results were reported. As mentioned before, HVOF is an alternative to solve this issue. See for instance previous contributions in HVOF HAp coatings with enhanced crystallinity, significantly reduced secondary phases and proper response in cell viability, proliferation and differentiation tests [90–92]

Similarly, since 1995, bio-glass (BG) coatings have been studied for biomedical applications manufactured by different thermal spray techniques, taking into account the ability to allow the growth of apatite layers, bone tissue growth start structures, over its surface when in contact with the simulated biological fluid (SBF). Both HAp and BG coatings have been shown to improve the biocompatibility and bioactivity properties of metal surfaces used in different implants. The above occurs because the former increases the growth rate of apatite crystals on their surface and is more durable in humid media than the latter. Similarly, the addition of BG to HAp coatings improves the mechanical properties of the entire layer system, making it more resistant to external mechanical loads that may suffer in the application to be used [93]. A. Cattini et al. 2013 investigated the effect of different combined coatings architectures using Ca-rich BG and stoichiometric HAp deposited by suspension plasma spray (see Figure 10). Among the composite, dual and graded architectures, the last demonstrate the higher biocompatibility, mechanical properties, adherence, and stability.

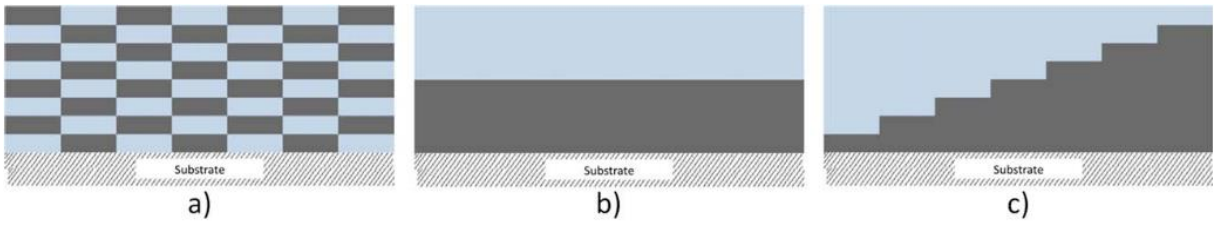

Figure 10. Designed microstructures of the biphasic coatings: (a) composite, (b) duplex, and (c) graded. Light blue: BG_Ca glass; Dark grey: HA. Adapted from [94].

REFERENCES

[1] S. V. Dorozhkin, Calcium Orthophosphates as Bioceramics: State of the Art, J. Funct. Biomater. 1 (2010) 22–107. doi:10.3390/jfb1010022.

[2] H. Liang, B. Shi, A. Fairchild, T. Cale, Applications of plasma coatings in artificial joints: An overview, Vacuum. 73 (2004) 317–326. doi:10.1016/j.vacuum.2003.12.160.

[3] OECD, Hip and knee replacement, Heal. a Glance Eur. 2012. (2012) 86–87. doi:10.1787/9789264183896-37-en.

[4] M. Mittal, S.K. Nath, S. Prakash, Characterization of Plasma Sprayed Hydroxyapatite Coatings on AISI 316L SS and Titanium Substrate and their Corrosion Behavior in Simulated Body Fluid, 10 (2011) 1041–1049.

[5] D.F. Williams, On the nature of biomaterials, Biomaterials. 30 (2009) 5897–5909. doi:10.1016/j.biomaterials.2009.07.027.

[6] a Sola, D. Bellucci, V. Cannillo, a Cattini, Bioactive glass coatings: a review, Surf. Eng. 27 (2011) 560–572. doi:10.1179/1743294410Y.0000000008.

[7] A. Chetty, I. Wepener, M.K. Marei, Y. El Kamary, R.M. Moussa, Synthesis, properties and applications of Hydroxyapatite, in: Hydroxyapatite Synth. Prop. Appl., 1st ed., Nova, 2012: pp. 1–477.

[8] R.B. Heimann, Materials Science of Crystalline Bioceramics : A Review of Basic Properties and Applications, J. C. 1 (2002) 23–46.

[9] E. Fiume, J. Barberi, E. Vern, F. Baino, Bioactive Glasses : From Parent 45S5 Composition to Scaffold-Assisted Tissue-Healing Therapies, (2018). doi:10.3390/jfb9010024.

[10] S. Hampshire, Bioglasses and Bioglass-ceramics, in: Appl. to Bioceram. Bioglasses, Madrid, Spain, 2015: pp. 17–19.

[11] H.R. Fernandes, A. Gaddam, A. Rebelo, D. Brazete, G.E. Stan, J.M.F. Ferreira, Bioactive glasses and glass-ceramics for healthcare applications in bone regeneration and tissue engineering, Materials (Basel). 11 (2018) 1–57. doi:10.3390/ma11122530.

[12] T.J. Levingstone, Ceramics for Medical Applications, in: L. Looney (Ed.), Grad. Lev. Resour. Mater. Eng., Dublin City University, Dublin, 2008: p. 58.

[13] G.P. Jayaswal, S.P. Dange, a N. Khalikar, Bioceramic in dental implants: A review., J. Indian Prosthodont. Soc. 10 (2010) 8–12. doi:10.1007/s13191-010-0002-4.

[14] A. Cattini, Coatings of bioactive glasses and hydroxyapatite and their properties, Univesité de Limoges, 2013.

[15] L.L. Hench, Bioceramics: From Concept to Clinic, J. Am. Ceram. Soc. 74 (1991) 1487–1510. doi:10.1111/j.1151-2916.1991.tb07132.x.

[16] P. Ptacek, Apatites and their Synthetic Analogues, 2016.

[17] Y. Suetsugu, T. Tateishi, Implants and biomaterials (hydroxyapatite), in: Implants, World Scientific Publishing Co Pvt Ltd, Singapore, 2008: pp. 1–10.

[18] W.L. Jaffe, D.F. Scott, Hydroxyapatite-Coated Prostheses Current Concepts Review - Total Hip Arthroplasty with Current Concepts Review Total Hip Arthroplasty with Hydroxyapatite-Coated Prostheses* Basic-Science and Preclinical Studies, J. Bone Jt. Surg. 78 (1996) 1918–34.

[19] S. Marković, L. Veselinović, M.J. Lukić, L. Karanović, I. Bračko, N. Ignjatović, D. Uskoković, Synthetical bone-like and biological hydroxyapatites: a comparative study of crystal structure and morphology., Biomed. Mater. 6 (2011) 045005. doi:10.1088/1748-6041/6/4/045005.

[20] International Organization for Standardization, ISO13779-6 Implants for surgery - Hydroxyapatite: Powders, 1st ed., 2015.

[21] International Organization for Standardization, ISO13779-1: Ceramic hydroxyapatite, 2nd ed., 2008.

[22] I. Demnati, D. Grossin, C. Combes, C. Rey, Plasma-Sprayed apatite Coatings: Review of physical-chemical characteristics and their biological consequences, J. Med. Biol. Eng. 34 (2014) 1–7. doi:10.5405/jmbe.1459.

[23] J.P. Gagne, K.A. Wylliet, Relative effectiveness of three repair strategies on the visual-identification of misperceived words, Ear Hear. 10 (1989) 368–374. doi:10.1097/00003446-198912000-00009.

[24] M. Ajeesh, B.F. Francis, J. Annie, P.R.H. Varma, Nano iron oxide-hydroxyapatite composite ceramics with enhanced radio-opacity, J. Mater. Sci. Mater. Med. 21 (2010)

1427–1434. doi:10.1007/s10856-010-4005-9.

[25] G. Ciobanu, A.M. Bargan, C. Luca, O. Ciobanu, The bi-substituted hydroxyapatite as radio-opaque material, RAD Conf. Proc. 2015-June (2015) 479–482. doi:10.21175/RadJ.2016.02.016.

[26] K.M. Lachowski, S.B. Botta, C.A. Lascala, A.B. Matos, M.A.P. Sobral, Study of the radio-opacity of base and liner dental materials using a digital radiography system, Dentomaxillofacial Radiol. 42 (2013) 8. doi:10.1259/dmfr.20120153.

[27] B. Li, T. Webster, Orthopedic biomaterials: Advances and applications, 2018. doi:10.1007/978-3-319-73664-8.

[28] C. Berndt, G. Haddad, A. Farmar, K. Gross, Thermal spraying for bioceramic applications, Mater. Forum (Rushcutters Bay). 14 (1990) 161–173.

[29] M. Sadat-Shojai, M.T. Khorasani, E. Dinpanah-Khoshdargi, A. Jamshidi, Synthesis methods for nanosized hydroxyapatite with diverse structures, Acta Biomater. 9 (2013) 7591–7621. doi:10.1016/j.actbio.2013.04.012.

[30] P. Ptáček, Synthetic Phase with the Structure of Apatite, Apatites Their Synth. Analog. - Synth. Struct. Prop. Appl. (2016). doi:10.5772/62212.

[31] E. Bouyer, F. Gitzhofer, M.I. Boulos, Suspension plasma spraying for hydroxyapatite powder preparation by RF plasma, IEEE Trans. Plasma Sci. 25 (1997) 1066–1072. doi:10.1109/27.649627.

[32] A. Killinger, P. Müller, R. Gadow, What Do We Know, What are the Current Limitations of Suspension HVOF Spraying?, J. Therm. Spray Technol. 24 (2015) 1130–1142. doi:10.1007/s11666-015-0264-9.

[33] A.L. Giraldo-Betancur, D.G. Espinosa-Arbelaez, A. Del Real-López, B.M. Millan-Malo, E.M. Rivera-Muñoz, E. Gutierrez-Cortez, P. Pineda-Gomez, S. Jimenez-Sandoval, M.E. Rodriguez-García, Comparison of physicochemical properties of bio and commercial hydroxyapatite, Curr. Appl. Phys. 13 (2013) 1383–1390. doi:10.1016/j.cap.2013.04.019.

[34] L. Sun, C.C. Berndt, K.A. Gross, A. Kucuk, Material Fundamentals and Clinical Performance of Plasma- Sprayed Hydroxyapatite Coatings : A Review, J. Mater. Res. 58 (2001) 570–592. doi:10.1002/jbm.xxxx.

[35] T. Thamaraiselvi, S. Rajeswari, Biological evaluation of bioceramic materials-a review, Carbon N. Y. 24 (2004) 172.

[36] E.D. Zanotto, J.C. Mauro, The glassy state of matter: Its definition and ultimate fate, J. Non. Cryst. Solids. 471 (2017) 490–495. doi:10.1016/j.jnoncrysol.2017.05.019.

[37] J.R. Jones, Reprint of: Review of bioactive glass: From Hench to hybrids, Acta Biomater. 23 (2015) S53–S82. doi:10.1016/j.actbio.2015.07.019.

[38] B. Ratner, A. Hoffman, F. Schoen, J. Lemons, Biomaterial Science - An Introduction to Materials in Medicine, 2004.

[39] L.L. Hench, An Introduction to Bioceramics, 2nd ed., Imperial College Press, 2013. doi:10.1142/9781908977168_0004.

[40] L.L. Hench, J. Wilson, Surface-Active Biomaterials, Science (80-.). 226 (1984) 630–636.

[41] Z. Imran, Bioactive Glass: A Material for the Future, World J. Dent. 3 (2012) 199–201. doi:10.5005/jp-journals-10015-1156.

[42] A. Hoppe, Bioactive Glass Derived Scaffolds with Therapeutic Ion Releasing Capability for Bone Tissue Engineering, 201. (2014) 195.

[43] R. Madanat, N. Moritz, E. Vedel, E. Svedstro, H.T. Aro, Radio-opaque bioactive glass markers for radiostereometric analysis, Acta Biomater. 5 (2009) 3497–3505. doi:10.1016/j.actbio.2009.05.038.

[44] W.J. Stark, D. Mohn, M. Zehnder, T. Imfeld, Radio-oupaque bioactive glass materials, US008658188B2, 2014.

[45] M. Montazerian, E. Dutra Zanotto, History and trends of bioactive glass-ceramics, J. Biomed. Mater. Res. - Part A. 104 (2016) 1231–1249. doi:10.1002/jbm.a.35639.

[46] M.M. Koç, N. Aslan, A.P. Kao, A.H. Barber, Evaluation of X-ray tomography contrast agents: A review of production, protocols, and biological applications, Microsc. Res. Tech. 82 (2019) 812–848. doi:10.1002/jemt.23225.

[47] T.J. Barrs, X-rays and radio-opaque drugs, Am. J. Heal. Pharm. 62 (2005) 2026–2030. doi:10.2146/ajhp040321.

[48] G. Sabbagh, J; Vreven, J; Leloup, Radiopacity of resin-based materials measured in film

radiographs and storage phosphor plate, Oper. Dent. 29 (2004) 677–684.

[49] M. Hernández-Rivera, I. Kumar, S.Y. Cho, B.Y. Cheong, M.X. Pulikkathara, S.E. Moghaddam, K.H. Whitmire, L.J. Wilson, High-Performance Hybrid Bismuth-Carbon Nanotube Based Contrast Agent for X-ray CT Imaging, ACS Appl. Mater. Interfaces. 9 (2017) 5709–5716. doi:10.1021/acsami.6b12768.

[50] W. Dukic, B. Delija, D. Derossi, I. Dadic, Radiopacity of composite dental materials using a digital X-ray system, Dent. Mater. J. 31 (2012) 47–53. doi:10.4012/dmj.2011-119.

[51] R.R. Vivan, R. Ordinola-Zapata, C.M. Bramante, N. Bernardineli, R.B. Garcia, M.A. Hungaro Duarte, I.G. de Moraes, Evaluation of the radio-opacity of some commercial and experimental root-end filling materials, Oral Surgery, Oral Med. Oral Pathol. Oral Radiol. Endodontology. 108 (2009) e35–e38. doi:10.1016/j.tripleo.2009.07.037.

[52] V. Vega Flores, Evaluación de la radiopacidad de materiales para provisionalización, Universidad de Chile, 2012.

[53] S. Baroth, X. Bourges, B. Fellah, G. Daculsi, Radiopaque strategy for bone injectable substitute, Key Eng. Mater. 361-363 I (2008) 39–42. doi:10.4028/www.scientific.net/kem.361-363.39.

[54] L. Tian, L. Lu, J. Feng, M.P. Melancon, Radiopaque nano and polymeric materials for atherosclerosis imaging, embolization and other catheterization procedures, Acta Pharm. Sin. B. 8 (2018) 360–370. doi:10.1016/j.apsb.2018.03.002.

[55] Y. Cheng, H. Zhang, Novel Bismuth-Based Nanomaterials Used for Cancer Diagnosis and Therapy, Chem. - A Eur. J. 24 (2018) 17405–17418. doi:10.1002/chem.201801588.

[56] J. Huppert, F. Kiessling, J. Jayapaul, A. Kubelbeck, G. Larbig, X- ray contrast agent based on bismuth oxide-nanoparticles, EP 2 127 682 A1, 2009.

[57] C.M.B. Hincapié, M.J.P. Cárdenas, J.E.A. Orjuela, E.R. Parra, J.J. Olaya Florez, Physical-chemical properties of bismuth and bismuth oxides: Synthesis, characterization and applications, DYNA. 79 (2012) 139–148.

[58] A.P. Reverberi, P.S. Varbanov, M. Vocciante, B. Fabiano, Bismuth oxide-related photocatalysts in green nanotechnology: A critical analysis, Front. Chem. Sci. Eng. 12 (2018) 878–892. doi:10.1007/s11705-018-1744-5.

[59] P. Patnaik, Handbook of Inorganic Chemical Compounds, McGraw-Hill, 2003.

[60] P. Shuk, H.D. Wiemhöfer, U. Guth, W. Göpel, M. Greenblatt, Oxide ion conducting solid electrolytes based on Bi2O3, Solid State Ionics. 89 (1996) 179–196. doi:10.1016/0167-2738(96)00348-7.

[61] Y.C. Hwang, S.H. Lee, I.N. Hwang, I.C. Kang, M.S. Kim, S.H. Kim, H.H. Son, W.M. Oh, Chemical composition, radio-opacity, and biocompatibility of Portland cement with bismuth oxide, Oral Surgery, Oral Med. Oral Pathol. Oral Radiol. Endodontology. 107 (2009) e96–e102. doi:10.1016/j.tripleo.2008.11.015.

[62] H. Lusic, M.W. Grinstaff, X-ray-computed tomography contrast agents, Chem. Rev. 113 (2013) 1641–1666. doi:10.1021/cr200358s.

[63] C.E. da S. Bueno, E.G. Zeferino, L.R.C. Manhães, D.G.P. Rocha, R.S. Cunha, A.S. De Martin, Study of the bismuth oxide concentration required to provide Portland cement with adequate radio-opacity for endodontic use, Oral Surgery, Oral Med. Oral Pathol. Oral Radiol. Endodontology. 107 (2009) e65–e69. doi:10.1016/j.tripleo.2008.09.016.

[64] E.C. Kim, B.C. Lee, H.S. Chang, W. Lee, C.U. Hong, K.S. Min, Evaluation of the radio-opacity and cytotoxicity of Portland cements containing bismuth oxide, Oral Surgery, Oral Med. Oral Pathol. Oral Radiol. Endodontology. 105 (2008) 54–57. doi:10.1016/j.tripleo.2007.08.001.

[65] F. Du, J. Lou, R. Jiang, Z. Fang, X. Zhao, Y. Niu, S. Zou, M. Zhang, A. Gong, C. Wu, Hyaluronic acid-functionalized bismuth oxide nanoparticles for computed tomography imaging-guided radiotherapy of tumor, Int. J. Nanomedicine. 12 (2017) 5973–5992. doi:10.2147/IJN.S130455.

[66] D. Mohn, M. Zehnder, T. Imfeld, W.J. Stark, Radio-opaque nanosized bioactive glass for potential root canal application: Evaluation of radio-opacity, bioactivity and alkaline capacity, Int. Endod. J. 43 (2010) 210–217. doi:10.1111/j.1365-2591.2009.01660.x.

[67] P.L. Fauchais, J.V.R. Heberlein, M.I. Boulos, Thermal Spray Fundamentals, 2014. doi:10.1007/978-0-387-68991-3.

[68] A. Vardelle, C. Moreau, J. Akedo, H. Ashrafizadeh, C.C. Berndt, J.O. Berghaus, M. Boulos, J. Brogan, A.C. Bourtsalas, A. Dolatabadi, M. Dorfman, T.J. Eden, P. Fauchais, G. Fisher, F. Gaertner, M. Gindrat, R. Henne, M. Hyland, E. Irissou, E.H. Jordan, K.A.

Khor, A. Killinger, Y.C. Lau, C.J. Li, L. Li, J. Longtin, N. Markocsan, P.J. Masset, J. Matejicek, G. Mauer, A. McDonald, J. Mostaghimi, S. Sampath, G. Schiller, K. Shinoda, M.F. Smith, A.A. Syed, N.J. Themelis, F.L. Toma, J.P. Trelles, R. Vassen, P. Vuoristo, The 2016 Thermal Spray Roadmap, J. Therm. Spray Technol. 25 (2016) 1376–1440. doi:10.1007/s11666-016-0473-x.

[69] F.E. García Costales, J.M. Cuentos Mejido, Recubrimientos de proyección por plasma, in: Encuentro Tribol. Univ. Oviedo, Repositorio Universidad de Oviedo, 2001: p. 10.

[70] R.S. Lima, B.R. Marple, Superior performance of high-velocity oxyfuel-sprayed nanostructured TiO2 in comparison to air plasma-sprayed conventional Al2O3-13TiO2, J. Therm. Spray Technol. 14 (2005) 397–404. doi:10.1361/105996305X59413.

[71] A. Valarezo, W.B. Choi, W. Chi, A. Gouldstone, S. Sampath, Process control and characterization of NiCr coatings by HVOF-DJ2700 system: A process map approach, J. Therm. Spray Technol. 19 (2010) 852–865. doi:10.1007/s11666-010-9492-1.

[72] S. Hasan, Design of experiment analysis of high velocity oxy-fuel coating of hydroxyapatite, Dublin City University, 2009.

[73] M. Ducos, V. Reitz, Coating properties and characteristics optimization of the operation of a plasma generator for thermal spraying, in: Proc. Elev. Int. Therm. Spray. Conf., Montreal, Canada, 1986: p. 847.

[74] J. Cihlář, A. Buchal, M. Trunec, Kinetics of thermal decomposition of hydroxyapatite bioceramics, J. Mater. Sci. 34 (1999) 6121–6131. doi:10.1023/A:1004769820545.

[75] C.J. Liao, F.H. Lin, K.S. Chen, J.S. Sun, Thermal decomposition and reconstruction of hydroxyapatite in air atmosphere, Biomed. Sci. Instrum. 35 (1999) 99–104.

[76] P. Cheang, K.A. Khor, Addressing processing problems associated with plasma spraying of hydroxyapatite coatings, Biomaterials. 17 (1996) 537–544. doi:10.1016/0142-9612(96)82729-3.

[77] R.B. Heimann, Plasma-Sprayed Hydroxylapatite-Based Coatings: Chemical, Mechanical, Microstructural, and Biomedical Properties, J. Therm. Spray Technol. 25 (2016) 827–850. doi:10.1007/s11666-016-0421-9.

[78] S. Amin, H. Panchal, A Review on Thermal Spray Coating Processes, Int. J. Curr. Trends Eng. Res. Sci. J. Impact Factor. 2 (2016) 556–563. http://www.ijcter.com.

[79] J. Chen, W. Tong, Y. Cao, J. Feng, X. Zhang, Effect of atmosphere on phase transformation in plasma-sprayed hydroxyapatite coatings during heat treatment, J. Biomed. Mater. Res. 34 (1997) 15–20. doi:10.1002/(SICI)1097-4636(199701)34:1<15::AID-JBM3>3.0.CO;2-Q.

[80] R. Bosco, J. V. Van Den Beucken, S. Leeuwenburgh, J. Jansen, Surface engineering for bone implants: A trend from passive to active surfaces, Coatings. 2 (2012) 95–119. doi:10.3390/coatings2030095.

[81] Y.C. Tsui, C. Doyle, T.W. Clyne, Plasma sprayed hydroxyapatite coatings on titanium substrates Part 1: Mechanical properties and residual stress levels, Biomaterials. 19 (1998) 2015–2029. doi:10.1016/S0142-9612(98)00103-3.

[82] H. Li, K.A. Khor, P. Cheang, Effect of the powders' melting state on the properties of HVOF sprayed hydroxyapatite coatings, Mater. Sci. Eng. A. 293 (2000) 71–80. doi:10.1016/S0921-5093(00)01245-4.

[83] J.L. Ong, M. Appleford, S. Oh, Y. Yang, W. Chen, J.D. Bumgardner, W.O. Haggard, The Characterization and Development of Bioactive Hydroxyapatite Coatings, Surf. Modif. Cation Bioapplications. (2006) 67–69.

[84] R.S. Lima, K. a. Khor, H. Li, P. Cheang, B.R. Marple, HVOF spraying of nanostructured hydroxyapatite for biomedical applications, Mater. Sci. Eng. A. 396 (2005) 181–187. doi:10.1016/j.msea.2005.01.037.

[85] H. Li, K. a Khor, P. Cheang, Titanium dioxide reinforced hydroxyapatite coatings deposited by high velocity oxy-fuel (HVOF) spray, Biomaterials. 23 (2002) 85–91. http://www.ncbi.nlm.nih.gov/pubmed/11762858.

[86] I. Bran, M. Popescu, In vitro characterization of hydroxyapatite layers deposited by APS and HVOF thermal spraying methods, (2011) 25–31. doi:10.1016/S0142-9612(02)00431-3.

[87] R. Gadow, A. Killinger, N. Stiegler, Hydroxyapatite coatings for biomedical applications deposited by different thermal spray techniques, Surf. Coat. Technol. 205 (2010) 1157–1164. doi:10.1016/j.surfcoat.2010.03.059.

[88] L.S. Ozyegin, F.N. Oktar, G. Goller, E.S. Kayali, T. Yazici, Plasma-sprayed bovine hydroxyapatite coatings, Mater. Lett. 58 (2004) 2605–2609.

doi:10.1016/j.matlet.2004.03.033.

[89] G. Goller, F.N. Oktar, L.S. Ozyegin, E.S. Kayali, E. Demirkesen, Plasma-sprayed human bone-derived hydroxyapatite coatings : effective and reliable, Mater. Lett. 58 (2004) 2599–2604. doi:10.1016/j.matlet.2004.03.032.

[90] H. Li, K. a Khor, P. Cheang, Properties of heat-treated calcium phosphate coatings deposited by high-velocity oxy-fuel (HVOF) spray, Biomaterials. 23 (2002) 2105–12. http://www.ncbi.nlm.nih.gov/pubmed/11962650.

[91] J. Fernández, M. Gaona, J.M. Guilemany, Effect of Heat Treatments on HVOF Hydroxyapatite Coatings, J. Therm. Spray Technol. 16 (2007) 220–228. doi:10.1007/s11666-007-9034-7.

[92] M.G. Latorre, Recubrimientos biocompatibles obtenidos por proyección térmica y estudio in vitro de la función osteoblástica, Universitat de Barcelona, 2007.

[93] J.H. Chern Lin, K.S. Chen, C.P. Ju, Biocorrosion behavior of hydroxyapatite/bioactive glass plasma sprayed on Ti6A14V, Mater. Chem. Phys. 41 (1995) 282–289. doi:10.1016/0254-0584(95)80035-2.

[94] A. Cattini, D. Bellucci, A. Sola, L. Pawłowski, V. Cannillo, Microstructural design of functionally graded coatings composed of suspension plasma sprayed hydroxyapatite and bioactive glass, J. Biomed. Mater. Res. Part B Appl. Biomater. 102 (2014) 551–560. doi:10.1002/jbm.b.33034.

CHAPTER 3: EXPERIMENTAL DETAILS

1. FABRICATION OF FEEDSTOCK POWDERS

The fabrication process of the BHAp and melt-derived BG45S5 and BG45S5+Bi_2O_3 feedstock powders and their physical, chemical and bioactive properties will directly affect the final characteristics of the thermal spray coatings (i.e. structure, morphology, composition among others. Irregular particles of BHAp and radio-opaque and amorphous BG45S5 and BG45S5+Bi_2O_3 were selected as feedstock characteristics to study their properties, bioactivity and the influence of the thermal spray process on the deposition of these bioactive materials. Two routes were followed to prepare BHAp and bioactive glasses powders, either BG45S5 or BG45S5+Bi_2O_3. Firstly, a methodology that allows obtaining crystalline HAp from bovine biowaste. Secondly, the melt and fast quenching of oxides and carbonate mixture to obtain amorphous BG45S5 and BG45S5+Bi_2O_3. BHAp and bioactive glass powders were modified to obtain a proper final particle size to be thermally sprayed, separately or mixed among them in different ratios to fabricate gradual BHAp/BG+Bi_2O_3 coatings.

1.1.Bovine bone biowaste hydroxyapatite (BHAp) feedstock powder fabrication

Figure 1 presents the used methodology to obtain pure BHAp from bovine bones. This process was divided into different stages, starting from the collection of fresh bone to the obtaining of crystalline BHAp to be used as feedstock in thermal spray.

Figure 1. Procedure to obtain BHAp from bovine bones

Firstly, fresh bovine bones, obtained from a certified butcher shop, were manually cleaned to remove visible organic material (i.e. marrow, meat, and adhered tissue). Then, bones were cleaned again under conditions of high vapor pressure and temperature to remove the major quantity of fat, remain tissue, dry fluids, and other impurities. Subsequently, the bone was crushed using the cutting mill Retsch SM 200 (Retsch GmbH) to reduce the bone to pieces with sizes ≤ 5 mm. The purpose of this pre-milled stage was to reduce the size of the bone to obtain

a greater surface area exposed to subsequent clean stages and increase the efficiency of the process. Afterward, the crushed bones were again milled using a planetary ball mill by placing the pre-milled powder with alumina balls in jars made from the same oxide. This milling was performed in dry conditions and allowed to obtain a desired particle size distribution to be used as feedstock in thermal spray (~ 40µm). After, the recovered bovine bone powder was chemically treated, under temperature and ultrasound conditions. This chemical process was used to break the peptide bonds that bind the carboxyl (-$COOH$) with the amino group (NH_2) from organic molecules that were still present in the powder. The bovine powder was calcinated at different temperature rates to obtain the HAp structure without the coexistence of other additional phases and to remove some proteins from the bovine matrix as collagens. The relevance of assuring the complete protein cleaning lies with the aim of obtaining a feedstock powder that can be used for certified biomedical purposes.

Finally, the inorganic powder was placed in alumina crucibles and thermally treated employing specifically temperatures to avoid powder agglomeration and the desired properties on feedstock to be after thermally sprayed. Detailed information on the BHAp fabrication from bovine bones is found elsewhere [1].

1.2.Melt-derived bioactive glass45S5 (BG45S5) fabrication

A reliable method to fabricate the BG45S5 was proposed in this work based on previous contributions and some modifications according to both laboratory facilities and precursors selection. [2–9] Different precursors had been reported to be used as oxides or carbonates to fabricate BG4S5 by the melt and fast quenching method [9–11]. From the reports, the SiO_2, $CaCO_3$, and Na_2CO_3 powders were the most commonly used precursors. This is explained by two reasons: The silica and carbonates availability and the reachable temperature for decarbonization of calcium and sodium carbonates on the silica-based mixture. On the other hand, the P_2O_5 source to obtain the BG45S5 tends to change among the studied contributions. For instance, $CaHPO_4.2H_2O$ [10] $Na_3PO_4.12H_2O$ [9], $NH_4H_2PO_4$ [11] and Ca_3PO_4 [12] are some used compounds. The purpose of obtaining the P_2O_5 from these compounds is to avoid violent exothermic reactions of the isolated phosphorus pentoxide in high humidity conditions or to avoid weight mistakes given its high hydrophilicity.

Sand acid washed silica (purity ≤100 %) was selected as the silicon oxide base to prepare the bioactive glass. CaO (purity ≤100 %) was used to simplify the oxide weight and mixture step

process despite $CaCO_3$ decarbonization occurs at the range temperature of 635 °C - 865 °C following the reaction in equation 1 [13].

$$CaCO_3 \xrightarrow{\Delta} CaO + CO_{2(g)} \quad (1)$$

Na_2CO_3 was chosen as Na_2O source based on the low availability and high price of the oxide. It is important to note that the decarbonization temperature of Na_2CO_3 is reduced by the presence of SiO_2 and CaO to the range of 460 – 800 °C [14,15]. Table 1 summarizes the relevant information of the selected precursors to prepare the bioactive glass45S5.

Table 1. Selected precursors to fabricate BG45S5

Name	**Formula**	**No. CAS**	**Characteristics**
Silicon Oxide	SiO_2	60676-86-0	Acid washed sand
Calcium Oxide	CaO	1305-78-8	Dry and white powder
Sodium Carbonate	Na_2CO_3	497-19-8	Dry and white powder
Phosphorus Oxide	P_2O_5	1314-56-3	Hydrophilic white powder

Figure 2 shows the weight and mixing procedure of oxides and carbonate to prepare the BG45S5. Precursors bottles and plastic spatulas were labeled before weighting the oxides and carbonate in order to avoid cross-contamination between powders on the weight and mixture step. All powders were weighted in high accuracy balance Precisa 205A SCS (Precisa Instruments AG) using plastic plates. The area of work was protected with detachable paper properly marked to locate each oxide or carbonate. The quantity of Na_2CO_3 was adjusted to obtain 24.5 wt. % of Na_2O in the total oxides mixture weight based on the decarbonization stage and reaction and conversion showed in equation 2 and equation 3. Samples of 10 g were mixed as is presented in Table 2. Regarding P_2O_5, it is was not recommendable to mix it directly with sodium-based compounds as Na_2CO_3 according to the datasheet. Silica was helpful to reduce the rapid water absorption of the P_2O_5 when this oxide was manipulated in environment air conditions. Hence, SiO_2 and P_2O_5 were the first powders to be weighted and after mixed in an agate mortar.

$$Na_2CO_3 \xrightarrow{\Delta} Na_2O + CO_{2(g)} \quad (2)$$

$$2.45\ \text{g}\ Na_2O \times \frac{1mol\ Na_2O}{61.97\ \text{g}\ Na_2O} \times \frac{1mol\ Na_2CO_3}{1mol\ Na_2O} \times \frac{105.98\ g\ Na_2CO_3}{1mol\ Na_2CO_3} = 4.18\ g\ Na_2CO_3 \quad (3)$$

Table 2. Precursors weight to obtain the BG45S5 composition

Precursor	Weight (g)
SiO_2	4.5
CaO	2.45
Na_2CO_3	4.18
P_2O_5	0.6

Afterward, CaO and Na_2CO_3 were weighted and added to the mixture of SiO_2 and P_2O_5. The precursor's mixture was stored in closed propylene bottles before the melting and fast quenching stage.

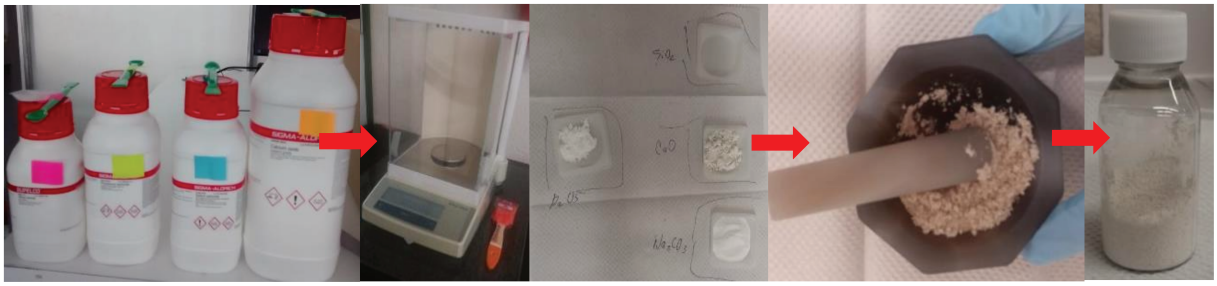

Figure 2. Weight and mixing of precursors procedure used to fabricate BG45S5

Bioactive glass 45S5 prepared by the traditional melt and quenching method has been fabricated under high-temperature conditions, usually above 1300° C [2] until 1500 °C [3]. Within this range some research had successfully employed different temperatures and steady times, for instance, 2 h at 1350 °C [4–6], 2 h [7] and 4h [8] at 1400 °C, 4h [8] and 1 h [9] at 1450 °C and 4h at 1500 °C [8]. The results from these contributions, the decarbonization temperature of Na_2CO_3, the BG45S melting temperature after 1230 °C and the maximum temperature of work of one used ovens (max T= 1250 °C) were considered in the selection of the heat treatment and glass fast quenching. Figure 3 presents the melt and fast quenching used methodology to obtain the BG45S and BG45S+Bi_2O_3. The mixture of oxides and carbonate was placed in a Pt crucible within the chamber of the 230v Nabertherm 60 L Eco top-loader kiln (Nabertherm GmbH). The

precursor's mixture was melted under the heat treatment showed in Figure 4. the proposed melting treatment started at room temperature to 950 °C at a heating rate of 5 °C/min and after to say at 950 °C during 5h. This stage was used to extract CO_2 from the Na_2CO_3. A second stage from 950 °C to 1250 °C at a heating rate of 10 °C/min and a steady time of 4h was used considering the maximum reachable temperature of this electric furnace (1250 °C). The glass was fast quenched in water at room temperature and glass frits were dried for 24 h after heat treatment was finished.

Figure 3. Melt and fast quenching procedure to fabricate BG45S5 using the Nebertherm Eco top-loader kiln

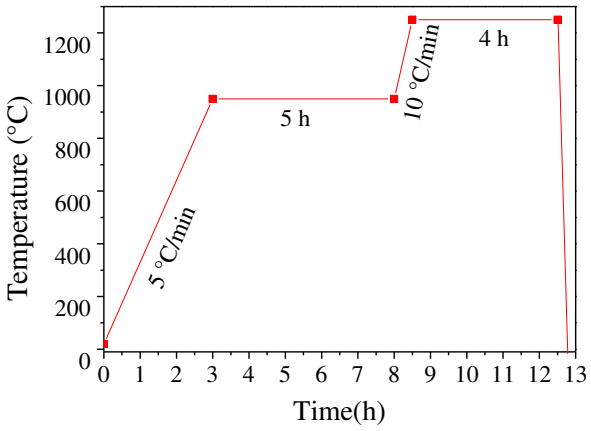

Figure 4. Heat treatment profile used to fabricate BG45S5

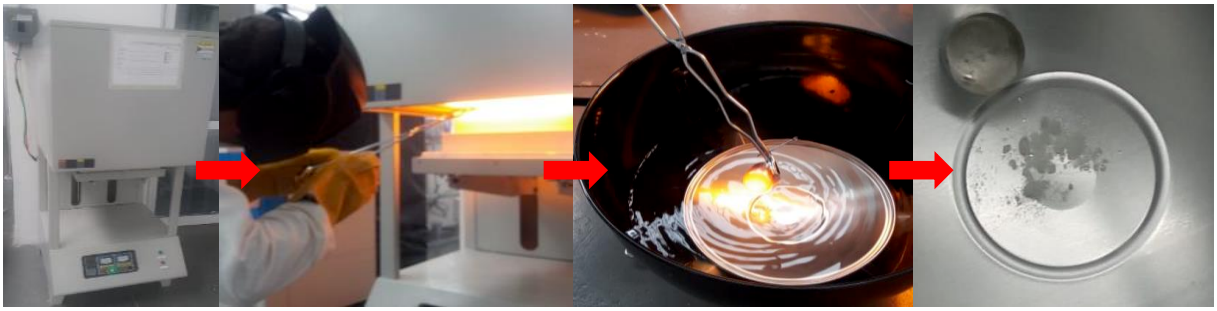

Figure 5. Melt and fast quenching procedure to fabricate BG45S5 using the IITV-1800 electric furnace

The oxides and carbonate mixture were also melted and fast quenched under the same parameters in the Cenaprot laboratory facilities using the electric furnace IITV-1800 (Briteg Instrumentos Cientificos de S.A. de C.V) following the procedure shown in Figure 5. This supports the reproducibility of the proposed methodology.

1.3.Melt-derived radio-opaque bioactive glass45S5 (BG45S5+Bi_2O_3) feedstock powder fabrication

Bi_2O_3 was mixed with the BG45S5 precursors to increase the radio-opacity of the glass by using compositions of 0 %, 1 %, 5 %, 10 %, 15 % and 20 % of Bi_2O_3 from the total weight of the powders mixture. The maximum value of Bi_2O_3 to be studied was selected based on previous findings where nanoparticles of BG 45s5 + 20 wt. % Bi_2O_3 obtained by flame spray synthesis showed a radio-opacity increased by 1.7 times [16].

Table 3. Compositions of the BG45s5+Bi_2O_3 powders to analyze their radio-opacity performance

Bi_2O_3 wt. % of Total wt.	**SiO_2 wt. %**	**CaO wt. %**	**Na_2O wt. %**	**P_2O_5 wt. %**	**Bi_2O_3 wt. %**
0	45	24.5	24.5	6	*0*
1	44.55	24.26	24.26	5.94	*0.99*
5	42.86	23.33	23.33	5.71	*4.76*
10	40.91	22.27	22.27	5.45	*9.09*
15	39.13	21.3	21.3	5.22	*13.04*
20	37.50	20.42	20.42	5	*16.67*

Table 3 shows detailed compositions of the BG45S5+Bi_2O_3 powders to be analyzed and used in the as feedstock for thermal spray. Finally, the selected quantity of Bi_2O_3 to be added to the BG45S5 will be the one that allows to maintain the structural and thermal characteristics of the BG45S5 and to reach the higher radio-opacity, simultaneously.

2. FABRICATION OF GRADED BHAp/BG45S5+Bi_2O_3 COATING BY APS THERMAL SPRAY

BHAp and BG45S5+Bi_2O_3 lab-made powders were used as feedstock to obtain thermal sprayed coatings. Firstly, BHAp was deposited by using APS and HVOF considering that these techniques are the most common methods to obtain thermally sprayed HAp coatings [17–24]. Afterward, BG45S5+Bi_2O_3 was milled, sieved, dried and thermally sprayed under the technique and parameters combination that shows better results in the fabrication of BHAp coatings. This, since structural decomposition of BHAp, is more probable than BG45S5 crystallization or decomposition which is detrimental for the coating stability [25,26]. The deposit of BG45S5+Bi_2O_3 was compared to BG45S5 APS coating obtained by using commercial feedstock powder BG45S5® (Schott AG) and the same plasma spray parameters. Lastly, a coating of both bioactive ceramics was gradually sprayed in different mixture ratios and their microstructure, structure, and bioactivity were compared with BG+Bi_2O_3 coating properties to understand the effect of the coating architecture and the use of BHAp.

2.1.Substrate and BHAp and BG powders preparation for thermal spray

302L Stainless steel substrates of 5 cm in diameter and 0.5 mm in thickness were grit blasted by using F36 Al_2O_3 (mean particle ~ 500 µm) at 6 bars. After, substrates were ultrasonically cleaned in acetone for 20 minutes to clean the remaining Al_2O_3 and other possible contamination sources. As is showed in Figure 3 BG45S5+Bi_2O_3 glass frits were. mixed in an Al_2O_3 jar with Al_2O_3 balls of 1 inch in diameter using a mass ratio of balls and frits of 2:1. The glass frits were crushed and milled in planetary milling at 250 RPM. Since glass is a fragile ceramic and the frits size reduction is not homogeneous, the milling was performed for short periods of time of 5 minutes. Then, the milled glass was sieved and powder with a size < 40 µm was selected for the fabrication of the thermally sprayed coatings, either as single or gradual coatings with BHAp. This milling procedure was repeated several times to obtain enough feedstock powder (~ 200 g) before the coating fabrication. BHAp and BG45S5+Bi_2O_3 feedstock powders were dried during 24 h at 100 °C before being thermally sprayed to avoid clogging in the lines, powder feeder and guns injectors. High purity argon was used as the carrier gas in APS and HVOF deposition techniques. Moreover, substrates were preheated before and during the BHAp and BG deposition to promote the splat formation [27]

2.2.BHAp coatings fabrication by APS and HVOF

BHAp coatings were obtained by APS using the Sulzer-Metco PTF4^{TM} gun using a nozzle of 6 mm in diameter under the parameters listed in Table 4 [28]. Figure 6 shows the APS set up to spray the bioceramics. F4 plasma gun position was fixed, and the surface of the substrate was fully coated by placing it in a rotary cylindrical sample holder (rotation velocity of 124 RPM and horizontal translation velocity of 24 mm /s) [29], (see Figure 6a and Figure 6b). The feedstock powder was externally fed in a radial direction to the plasma using the powder feeder Praxair 1264 and a 1.8 mm injector as is presented in Figure 6c.

BHAp was also sprayed by using the Diamond Jet 2700, Oerlikon-Metco HVOF gun. The spray trajectories were programmed in a KRC2 6-axis robot (KUKA, GmbH) (see Figure 7). The powder was projected at 657 LPM of total gas flow using the parameter combination presented in Table 5 [30]. The powder feeding was internal and axial to the HVOF plume by using the Sulzer 9M feeder.

Table 4. APS thermal spray parameters for BHAp coating deposition.

Parameter	Value
Ar plasma (NLPM)	53
H_2 plasma (NLPM)	7
SOD (mm)	100
PFR (g/min)	10
Current (A)	450
Spray time (min)	2

*Units and abbreviations: Normal Liters per Minute (NLPM), Stand-off Distance (SOD), Powder Feed Rate (PFR).

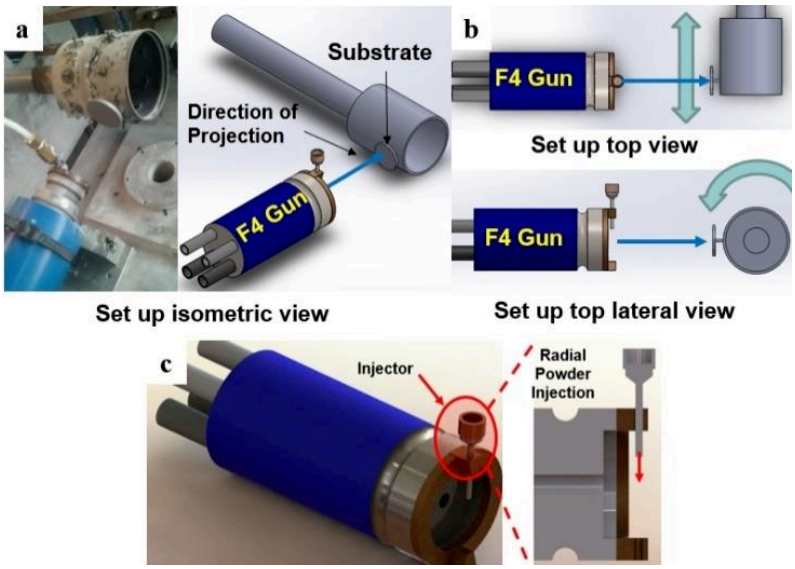

Figure 6. APS set up to spray BHAp and BG

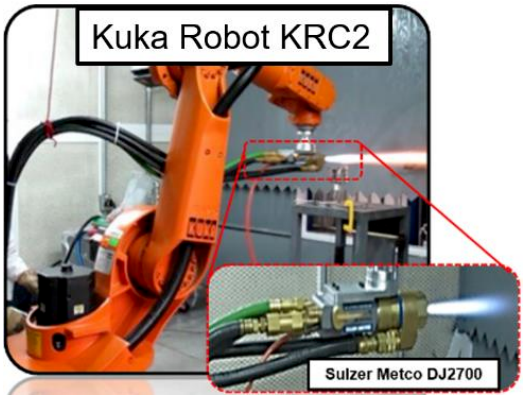

Figure 7. HVOF set up to spray BHAp (Hermann 2017)

Table 5. HVOF thermal spray parameters for BHAp coating deposition

Parameter	Value
O_2 flow(FMR)	26
C_2H_8 flow (FMR)	16
SOD (mm)	200
PFR (g/min)	16
NOP	6

*Units and abbreviations: Flow Meter Reading (FMR), Stand-off Distance (SOD), Powder Feed Rate (PFR) and NOP (Number of Passes).

2.3.BHAp APS coatings fabrication

Besides exploring the effect of the reported set of parameters of APS HAp coatings on the BHAp deposition, a complementary group of parameters combinations was studied. The set of parameters regarding current intensity I (A), powder feed rate PFR (g/min) and stand-off distance SOD (mm) was previously proposed by Levingston *et al.* for the evaluation of stoichiometric HAp coatings deposited by APS [31]. Spraying time was maintained constant at two minutes for all the experiments. The studied set of parameters is presented in the experimental space showed in Figure 8. The set of parameters used in section *2.2* is also presented in the middle of the right lower edge of the experimental cube. The PFR interval was modified according to the Praxair 1264 limits of work. Since BG45S5 thermal decomposition occurs at higher temperatures compared to HAp decomposition, the parameter combination selected to fabricate the gradual coating should be that one that allows keeping the major HAp percentage phase on the BHAp coating. Furthermore, the chosen set of parameters here is the same to be used in the fabrication of gradual BHAp/ BG45S5+Bi_2O_3 coatings.

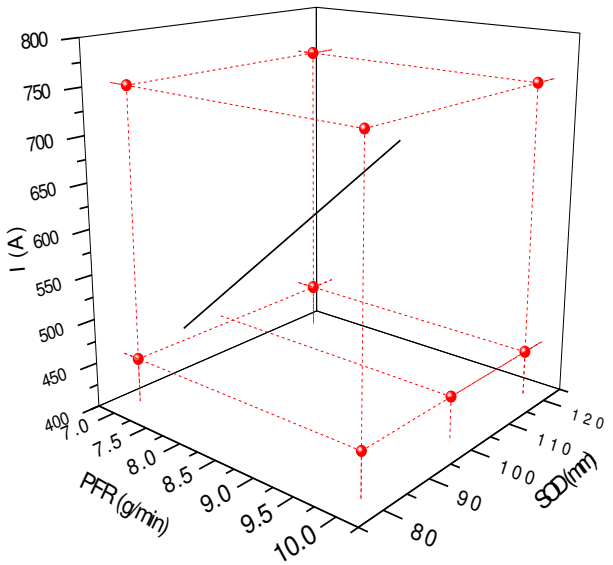

Figure 8. Experimental space to analyze APS thermal spray parameters influence on BHAp deposition

2.4.Graded BHAp/BG45S5+Bi_2O_3 coating fabrication by APS

BG45S5+Bi_2O_3 feedstock powder was deposited by APS on 302SSL substrates under the parameters combination selected in the previous section. This was performed before fabricating the BHAp/BG45S5+Bi_2O_3 gradual coatings to understand the effect that BHAp and the gradual

composition represent for BG45S5+Bi_2O_3 coating deposition. Commercial BG45S5 was also sprayed under the same set of parameters for comparative purposes. The procedure used to spray the gradual configuration of BHAp/BG+Bi_2O_3 coating is presented in Figure 9 and the powders ratios.

Table 6. Composition of the sprayed layers to obtain the gradual configuration

Layer	BHAp wt. %	BG+Bi_2O_3 wt. %
1	100	0
2	75	25
3	25	75
4	0	100

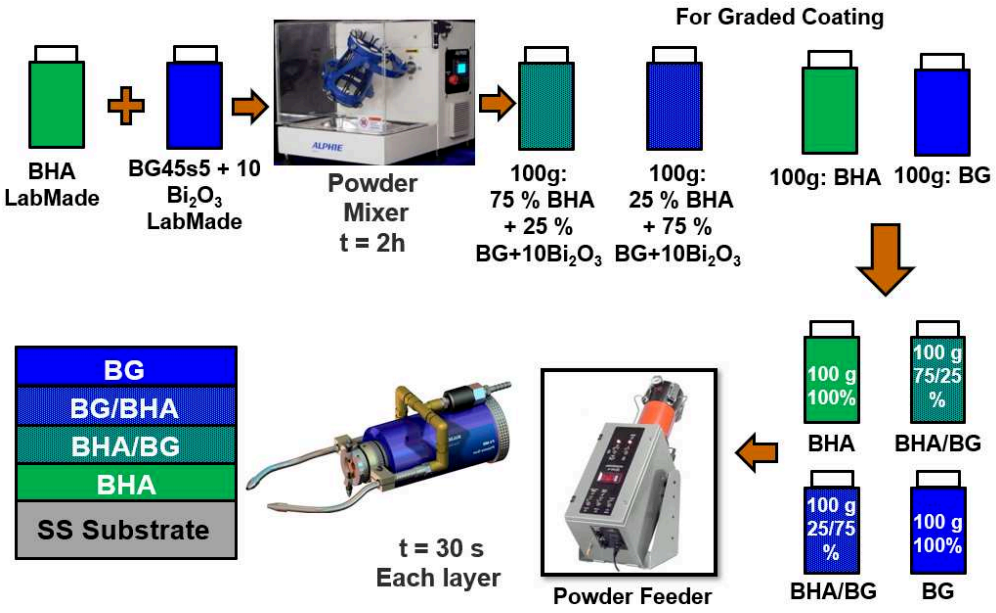

Figure 9. Methodology to fabricate gradual BHAp/BG45S5+Bi_2O_3 by APS thermal spray

Firstly, 100 g of BHAp and BG45S5+Bi_2O_3 mechanically mixed cans are prepared for 2h in ratios of 75:25, 25:75 BG45S5+Bi_2O_3. Afterward, 100 g of BHAp placed within the Praxair feeder and the powder is sprayed for 30 seconds under the plasma sprayed parameters selected in the *APS BHAp Coating Fabrication section.* Then, BHAp powder is extracted and the powder feeder is well cleaned with compressed air. A second and a third layer are sprayed following the same method. These layers are sprayed by using powders mixtures in

BHAp:BG45S5+Bi_2O_3 ratios of 75 g:25 g and 25 g:75 g, respectively (see Table 6). Finally, 100 g of BG45S5+Bi_2O_3 are placed in the powder feeder and the radio-opaque bioactive glasses sprayed as top-coat in the gradual coating under the same set of parameters.

3. CHARACTERIZATION OF FEEDSTOCK POWDERS AND COATINGS

3.1. Particle size distribution analysis by laser diffraction particle sizing (LDPS)

Solutions of the powders to be characterized, either BHAp, BG45S5 and BG45S5+Bi_2O_3 immersed in ethanol are prepared in glass bottles of 2 ml in volume. Later, small drops of the solution were added to the ethanol vessel of the particle size analyzer Granulo LA-950 (Horiba Scientific). Afterward, the Fraunhofer diffraction model methodology was selected as a measurement set up to determine the powder particle sizes after the laser diffraction. Moderate stirring and sonication were used during the analysis to avoid powder agglomeration.

3.2. Feedstock powders density analysis by Helium pycnometry

Feedstock powder density is an important property in thermal spray due to its relevance in the flow behavior of the materials from powders feeders to thermal spray guns. Since the main objective of this contribution was to obtain the gradual deposition of the bioceramics, the similar density of BHAp and BG45S5 allows proposing the mechanical mixing of the powders for their deposition. Moreover, the density of materials is compared to previous reports and references as commercial BG45S5. The density of the powders was measured by using the He pycnometer AccuPyc II 1340 (Micromeritics). 1 g of commercial and lab-made BG45S5 and BHAp were dried at 80°C for 24 h [32]. After powders were placed in an aluminum cell of 1.3 cm^3 in volume and 10 cycles of He gas degasification were employed to measure the density of the powders by gas pycnometry.

3.3. Structural characterization of feedstock powders by Fourier transformed infra-red spectroscopy (FTIR)

Vibrational modes of functional groups of the BHAp and BG45S5, either commercial or lab-made feedstock powders, were characterized by means of Fourier Transformed Infra-Red (FTIR) spectroscopy using the Spectrum GX (PerkinElmer Inc.) under the diffuse reflectance. The measurements were performed in the range of 500 cm^{-1} to 4000 cm^{-1} for BHAp and 400 cm^{-1} – 1200 cm^{-1} for BG45S5 feedstock powders, respectively [33].

3.4. Thermal analysis of BG45S5 and BG45S5+Bi_2O_3 feedstock powders by differential scanning calorimetry (DSC)

Characteristics temperatures of BG45S5, BG45S5+Bi_2O_3 (i.e T_g, T_c and T_m) and BG45S5 precursor mixture of oxides and carbonate, were studied by differential scanning calorimetry (DSC). Samples (50-60 mg) were placed in a Pt crucible next to an empty Pt reference within the TG-DSC STA 443F3 (Netzch). Exothermic and endothermic reactions, as a result of the differential calorimetry, were recorded in air atmosphere from 20 °C to 1300 °C at 5 °C / min. Mass changes in oxides mixture were monitored to evaluate the reactions during the glass fabrication. Finally, Commercial BG45S5 was also characterized under the same parameters for comparative purposes.

3.5. Compositional oxides analysis of BG45S5 by x-ray fluorescence (XRF)

The obtained glass was characterized by XRF to determine if its oxide composition follows the BG45S5 stoichiometry. For this purpose, 1 g of each prepared glass was mixed with 10 g of lithium tetraborate flux and melted in a Pt crucible at 1065°C for 26 mins in the Claisse LeNeo fusion instrument (Malvern Panalytical, UK). The system automatically empties the viscous mixture in a 40 mm in diameter and 3 mm of thickness Pt crucible and glass discs with these dimensions were obtained for XRF analysis. The used detailed preparation of samples for XRF characterization is found elsewhere [34,35]. The glass discs were extracted and placed in the sample holder of the XRF Zetium 1 kW equipment (Panalytical). XRF measurements were performed at 60 kV and 50 mA for 40 minutes per sample. The XRF measurements of BG45S5+Bi_2O_3 were not performed considering the possible Pt crucibles damage due to the presence of Bi_2O_3 in the glass melting and disc fabrication.

3.6. Radiopacity characterization of BG45s5+Bi_2O_3 feedstock powder

Figure 10 shows the used methodology to prepare the radio-opaque BG45S5 pellets. The studied compositions of the radio-opaque BG45S5+Bi_2O frits (See Table 3) were handed crushed in an agate mortar and sieved using a 400 mesh. 0.5 g of each composition of BG45S5+Bi_2O_3 powders were compressed in a 13 mm in diameter matrix using a uniaxial press (Sodemi RD20M). Pellets were obtained after 5 minutes of pressing the powder at 5 tons. A commercial BG45S5 pellet was also prepared as a reference using the same parameters. Binder was not used during the preparation to avoid the addition of components that can impact the radio-opacity measurement. Moreover, pellets were not sintered seeking to keep the amorphous

phase of the radio-opaque glass. Finally, the samples were dry at 100 °C for 24 h to reduce the pellet's brittleness. The thickness of the pellets was measured using a digital thickness gauge micrometer (Mitutoyo 547-313) with a resolution of 0.01 mm. Radiographic images of the pellets were obtained following the norm ISO 13116:2014 and using the intra-oral x-ray system TR-Elitys (Trophy). Voltage and current were fixed at 60 kV and 4 mA, respectively. The exposure time was changed until obtaining radiographic images with proper contrast. An aluminum step-wedge (98 % purity) with 20 steps and a thickness range from 0 to 100 mm (0.5 mm per step) was used as a reference (see Figure 11). The radiographic images of samples with the Al reference were digitally analyzed using the imageJ® software. Firstly, the mean gray value (MGV) of each step was measured and plotted as a function of each step wedge thickness. Secondly, the points were lineally fitted in the measured range. Finally, the MGV of each sample was measured and its value was interpolated in the previous calibration curve. The radio-opacity of the samples was measured 3 times and the units of this property reported in mm Al. An example of the radio-opacity measurement by digital image analysis is showed in Figure 12.

Figure 10. Procedure to prepare radio-opaque BG45S5 pellets following the norm ISO 13116:2014

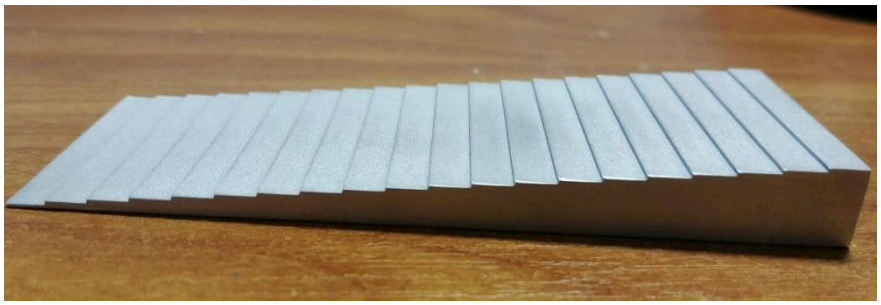

Figure 11. Aluminum reference step-wedge

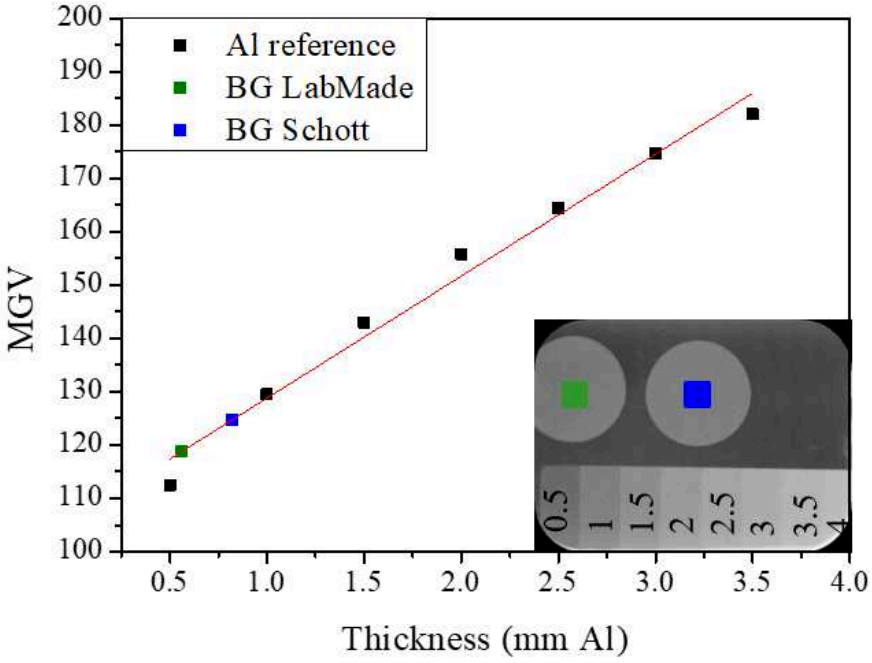

Figure 12. Mean gray value (MGV) of the Al reference at each step, and lab-made and commercial BG45S5 pellets. An inset of a radiographic image of BG45S5 pellets and Al step-wedge section is shown.

3.7.Structural characterization of feedstock powders and coatings by x-ray diffraction analysis (XRD)

Structural characterizations of feedstock powders and coatings were performed using an x-ray D8 ADVANCE (BRUKER, Massachusetts, USA) diffractometer with monochromatic CuK**α** radiation (λ = 1.5406 Å) operated at 40 kV and 40 mA. The XRD patterns were recorded between 20 to 70º on a 2θ scale in steps of 0.02º with a counting time of 0.5 s at each step. The analysis was carried out at a fixed angle of 5º under Bragg-Brentano configuration for feedstock powders, BHAp and BG coatings obtained in sections *1., 2.3.* and *2.4*. Regarding coatings obtained in section *2.2.* grazing angle x-ray diffraction (GIXRD) at a fixed angle of 1° using the DMax diffractometer (2100, Rigaku) operated at 30 kV and 20 mA was employed to analyze the structural composition of the thin apatite growth layer. This, since detailed information of the apatite grown, is a concern of this contribution and previous bioactivities studies of BHAp thermally sprayed were not found in the author's knowledge. Thereafter, Rietveld analysis used to obtain information related to the lattice parameters, phase percentage, crystallite size of crystalline phases was used. BHAp and BG powders were milled and sieved under 400 mesh to assure the powder uniformity and homogeneous height during the x-ray diffraction measurement.

3.7.1. ***Crystallized BG45S5 and BG45S5+Bi_2O_3 structural characterization by XRD***

The amorphous structure of bioactive glasses enhances the reactivity of the material and consequently the bioactivity rate. Thus, the aim structure to be obtained of the BG45S5 and BG45S5+Bi_2O_3 feedstock powders is amorphous. Moreover, the structural analysis of crystalline BG45S5 is well known [33], consequently, it is necessary to crystallize the bioactive glasses by performing heat treatment on the powders, study its structural arrangement and the implications of fabricating the BG45S5 including a radio-opaque oxide as the Bi_2O_3. Firstly, BG45S5 powders were crystallized in Al_2O_3 crucibles to maximum temperatures of 750 °C and 950 °C at a heating rate of 10 °C/ min and the fastest cooling rate allowable by the furnace resistances. This, considering the phase transitions of the BG45S5 between these two temperatures [26]. Secondly, BG45S5+Bi_2O_3 samples were crystallized 1060 °C before the first melting temperature of the BG45S5 (1190 °C) using the same previous type of crucible and heating and cooling rate to understand the role of Bi_2O_3 on the BG45S5 crystalline structure.

3.8. Morphology and microstructure characterization of feedstock powders and coatings by scanning electron microscopy (SEM)

Powders to be analyzed in SEM either BHAp or bioactive glasses were carefully placed in a carbon double side tape surface attached to sample holders and the surplus powder was removed with compressed air. Regarding coatings, two types of micrographs were studied by SEM analysis: cross-section and surface images. In the first, coatings were embedded in resin, sectioned and mirror-polished to revel the coating cross-section morphology. In the second, the coating surface was cleaned with compress air and images were recorded. Powders, coatings surface and coating cross-section were covered with a Pt thin layer in order to increase the electrical conductivity of the samples and enhance the image quality. SEM images were recorded at <15 kV and the secondary electron detector was employed. Finally, the cross-section of gradual coatings was studied by SEM combined with dispersive energy spectrometry (EDS) to determine the gradual configuration thought the identification of the element distribution in the coating architecture

3.9. Bioactivity Characterization of BG45S5 feedstock and coatings powders by immersion in simulated body fluid (SBF)

BG powders, BG and graded BHAp/BG coatings bioactivity were studied by its ability to promote the apatite layer growth after immersion in simulated body fluid (SBF) and ion exchange between the coating and the simulated fluid. The used SBF was Kokubo's solution and its preparation is found elsewhere [36]. Immersed samples were incubated at 37 °C to simulate the blood plasma conditions and analyzed at different proposed times for powders and coatings. Finally, SBF was filtered and elements concentration either Ca, P, Mg or Si were measured in the solution was measured by Inductively Coupled Plasma-Optical Emission Spectroscopy (ICP-OES) employing the Perkin Elmer Optima 8300 spectrometer, after the samples were removed.

3.9.1. ***BG Powders bioactivity***

75 g of commercial BG45S5 and lab-made BG45S5 were separately immersed in 50 ml of SBF using polypropylene falcon tubes following the protocol proposed by A.L.B. Maçon *et al.* Afterward, powders were washed 3 times with distilled water and dried at 100 °C for 24h. The powder bioactivity was evaluated by the apatite layer growth monitored by XRD. Moreover, the pH of SBF was analyzed and reported during the tests. Finally, concentrations of Ca, P and Si in SBF were measured by ICP.

3.9.2. ***Thermally sprayed coatings***

Thermal spray coatings were sectioned in 1 cm^2 in area, down face immersed in SBF on polypropylene falcon tubes and incubated at 37 °C [37] during 3, 5 and 10 days. Afterward, samples were washed with distilled water and dried for 24h at room temperature. The apatite formation on coatings was monitored by SEM micrographs analysis. Furthermore, BG and gradual BHAp/BG+Bi_2O_3 coatings apatite structures were analyzed by conventional XRD using the Bragg-Brentano configuration. On the other hand, structural analysis of apatite grown on BHAp coating was performed by GIXRD. Finally, Ca, P, and Mg concentration in SBF was measured.

REFERENCES

[1] J.A. Rincon-López, J.A. Hermann-Muñoz, A.L. Giraldo-Betancur, A. De Vizcaya-Ruiz, J.M. Alvarado-Orozco, J. Muñoz-Saldaña, Synthesis, Characterization and In Vitro Study of Synthetic and Bovine-Derived Hydroxyapatite Ceramics: A Comparison, Materials (Basel). 11 (2000) 1–17. doi:10.3390/ma11020333.

[2] B. Li, T. Webster, Orthopedic Biomaterials Advances and Applications, Springer, 2017. doi:10.1007/978-3-319-73664-8.

[3] N.M. Neves, R.L. Reis, Biomaterials From Nature for Advances Devices and Therapies, John Wiley & Sons, Inc, New Jersey, 2016. doi:10.1002/9781119126218.

[4] J.. Chern Lin, H.. Lin, S.. Ding, C.. Ju, Characterization of immersed hydroxyapatite-bioactive glass coatings in Hank's solution, Mater. Chem. Phys. 64 (2000) 229–240. doi:10.1016/S0254-0584(00)00209-1.

[5] H.C. Lin, Morphologic variation in plasma-sprayed hydroxyapatite-bioactive glass composite coatings in Hank's solution, J. Biomed. Mater. Res. 28 (1994) 723–730. doi:10.1002/jbm.820280609.

[6] A. El-ghannam, E. Hamazawy, A. Yehia, Effect of thermal treatment on bioactive glass microstructure, corrosion behavior, z potential, and protein adsorption, J. Biomed. Mater. Res. 55 (2001) 387–395. doi:10.1002/1097-4636(20010605)55:3<387::aid-jbm1027>3.0.co;2-v.

[7] X. Chen, Y. Meng, Y. Li, N. Zhao, Investigation on bio-mineralization of melt and sol – gel derived bioactive glasses, Appl. Surf. Sci. 255 (2008) 562–564. doi:10.1016/j.apsusc.2008.06.101.

[8] G. Goller, The effect of bond coat on mechanical properties of plasma sprayed bioglass-titanium coatings, Ceram. Int. 30 (2004) 351–355. doi:10.1016/S0272-8842(03)00107-X.

[9] L. Altomare, D. Bellucci, G. Bolelli, B. Bonferroni, V. Cannillo, L. De Nardo, R. Gadow, A. Killinger, L. Lusvarghi, A. Sola, N. Stiegler, Microstructure and in vitro behaviour of 45S5 bioglass coatings deposited by high velocity suspension flame spraying (HVSFS), J. Mater. Sci. Mater. Med. 22 (2011) 1303–19. doi:10.1007/s10856-011-4307-6.

[10] R. Comesaña, F. Quintero, F. Lusquiños, M.J. Pascual, M. Boutinguiza, A. Durán, J.

Pou, Laser cladding of bioactive glass coatings, Acta Biomater. 6 (2010) 953–961. doi:10.1016/j.actbio.2009.08.010.

[11] R.A. Martin, H. Twyman, D. Qiu, J.C. Knowles, R.J. Newport, A study of the formation of amorphous calcium phosphate and hydroxyapatite on melt quenched Bioglass® using surface sensitive shallow angle X-ray diffraction, J. Mater. Sci. Mater. Med. 20 (2009) 883–888. doi:10.1007/s10856-008-3661-5.

[12] M. Mačković, A. Hoppe, R. Detsch, D. Mohn, W.J. Stark, E. Spiecker, A.R. Boccaccini, Bioactive glass (type 45S5) nanoparticles: In vitro reactivity on nanoscale and biocompatibility, J. Nanoparticle Res. 14 (2012) 1–22. doi:10.1007/s11051-012-0966-6.

[13] I. Halikia, L. Zoumpoulakis, E. Christodoulou, D. Prattis, Kinetic study of the thermal decomposition of calcium carbonate by isothermal methods of analysis, 1 (2001) 89–102.

[14] J. Kim, Y. Lee, H. Lee, Decomposition of Na2CO3 by Interaction with SiO2 in Mold Flux of Steel Continuous Casting, 41 (2001) 116–123.

[15] R. V. Siriwardane, J.A. Poston, C. Robinson, T. Simonyi, Effect of additives on decomposition of sodium carbonate: Precombustion CO2 capture sorbent regeneration, Energy and Fuels. 25 (2011) 1284–1293. doi:10.1021/ef101486m.

[16] W.J. Stark, D. Mohn, M. Zehnder, T. Imfeld, Radio-opaque bioactive glass materials, 2014. http://www.google.com/patents/US8658188.

[17] L. Sun, C.C. Berndt, K.A. Gross, A. Kucuk, Material Fundamentals and Clinical Performance of Plasma- Sprayed Hydroxyapatite Coatings : A Review, J. Mater. Res. 58 (2001) 570–592. doi:10.1002/jbm.xxxx.

[18] L. Sun, Thermal Spray Coatings on Orthopedic Devices: When and How the FDA Reviews Your Coatings, J. Therm. Spray Technol. 27 (2018) 1280–1290. doi:10.1007/s11666-018-0759-2.

[19] J. Cizek, K.A. Khor, Role of in-flight temperature and velocity of powder particles on plasma sprayed hydroxyapatite coating characteristics, Surf. Coatings Technol. 206 (2012) 2181–2191. doi:10.1016/j.surfcoat.2011.09.058.

[20] H. Li, K.A. Khor, P. Cheang, Effect of the powders' melting state on the properties of HVOF sprayed hydroxyapatite coatings, Mater. Sci. Eng. A. 293 (2000) 71–80.

doi:10.1016/S0921-5093(00)01245-4.

[21] R.S. Lima, K. a. Khor, H. Li, P. Cheang, B.R. Marple, HVOF spraying of nanostructured hydroxyapatite for biomedical applications, Mater. Sci. Eng. A. 396 (2005) 181–187. doi:10.1016/j.msea.2005.01.037.

[22] H. Li, K. a Khor, P. Cheang, Titanium dioxide reinforced hydroxyapatite coatings deposited by high velocity oxy-fuel (HVOF) spray, Biomaterials. 23 (2002) 85–91. http://www.ncbi.nlm.nih.gov/pubmed/11762858.

[23] I. Bran, M. Popescu, In vitro characterization of hydroxyapatite layers deposited by APS and HVOF thermal spraying methods, (2011) 25–31. doi:10.1016/S0142-9612(02)00431-3.

[24] J.L. Ong, M. Appleford, S. Oh, Y. Yang, W. Chen, J.D. Bumgardner, W.O. Haggard, The Characterization and Development of Bioactive Hydroxyapatite Coatings, Surf. Modif. Cation Bioapplications. (2006) 67–69.

[25] C.J. Liao, F.H. Lin, K.S. Chen, J.S. Sun, Thermal decomposition and reconstruction of hydroxyapatite in air atmosphere, Biomed. Sci. Instrum. 35 (1999) 99–104.

[26] A.R. Boccaccini, Q. Chen, L. Lefebvre, Sintering, crystallization and biodegradation behaviour of Bioglass-derived glass – ceramics, Faraday Discuss. 136 (2007) 27–44. doi:10.1039/b616539g.

[27] M. Lufitha, Effect of Substrate Temperature on Coating Adhesion, University of Toronto, 2001.

[28] T.J. Levingstone, Optimisation of Plasma Sprayed Hydroxyapatite Coatings, Dublin City University, 2008.

[29] M. Mellali, Influence de la rugosité et de la température de surface du substrat sur l'adhérence et les contraintes résiduelles au sein de dépôts d'alumin, Université de Limoges, 1994.

[30] J.A. Hermann-Muñoz, J.A. Rincón-López, G.A. Clavijo-Mejía, A.L. Giraldo-Betancur, J.M. Alvarado-Orozco, A. De Vizcaya-Ruiz, J. Muñoz-Saldaña, Influence of HVOF parameters on HAp coating generation: An integrated approach using process maps, Surf. Coat. Technol. 358 (2019) 299–307. doi:10.1016/j.surfcoat.2018.11.029.

[31] T.J. Levingstone, M. Ardhaoui, K. Benyounis, L. Looney, J.T. Stokes, Plasma sprayed hydroxyapatite coatings: Understanding process relationships using design of experiment analysis, Surf. Coatings Technol. 283 (2015) 29–36. doi:10.1016/j.surfcoat.2015.10.044.

[32] P. Sepulveda, J.R. Jones, L.L. Hench, Characterization of Melt-Derived 45S5 and sol-gel–derived 58S Bioactive Glasses, J. Biomed. Mater. Res. (2001) 564–569. doi:10.1002/jbm.0000.

[33] L. Lefebvre, J. Chevalier, L. Gremillard, R. Zenati, G. Thollet, D. Bernache-Assolant, A. Govin, Structural transformations of bioactive glass 45S5 with thermal treatments.., Acta Mater. 55 (2007) 3305–3313. doi:10.1016/j.actamat.2007.01.029.

[34] J.P. Willis, Sample Preparation XRF and Glass Beads by Borate Fusions, (2010) 57. https://www.malvernpanalytical.com/en/assets/Glass beads by borate fusion_tcm50-54735.pdf.

[35] M. Watanabe, Sample Preparation for X-ray Fluorescence Analysis IV. Fusion Bead Method, Part 1 Basic Principals, Rigaku J. 31 (2015) 12–17. https://www.rigaku.com/downloads/journal/RJ31-2/Rigaku Journal 31-2_12-17.pdf.

[36] A. Oyane, H. Kim, T. Furuya, T. Kokubo, T. Miyazaki, T. Nakamura, Preparation and assessment of revised simulated body fluids, J. Biomed. Mater. Res. A. 65 (2002) 19–21. doi:10.1002/jbm.a.10482.

[37] R.T. Candidato, C. Thouzellier, L. Pawłowski, Evaluation of the in-vitro behavior of nanostructured hydroxyapatite and zinc doped hydroxyapatite coatings obtained using solution precursor plasma spraying, J. Biomed. Mater. Res. - Part B Appl. Biomater. 106 (2018) 2101–2108. doi:10.1002/jbm.b.34014.

CHAPTER 4: RESULTS AND DISCUSSION

1. CHARACTERIZATION OF FEEDSTOCK POWDERS

1.1.BHAp

1.1.1. BHAp feedstock powders particle size distribution, morphology and microstructure characterization by laser diffraction particle sizing (LDPS) and scanning electron microscopy (SEM)

The BHAp feedstock morphology and size distribution are presented in Figure 1. The feedstock powder consists of rounded and irregular particles with small pores all along their surface, as is observed in Figure 1a. It is also noticed that smaller particles tend to agglomerate, which is attributed to the hydrophilic properties of the powder [1]. Figure 1b shows the BHAp feedstock size distribution. A normal distribution is evidenced with particle sizes d_{10} = 23.0 µm, d_{50} = 32.3 µm, and d_{90} = 48.8 µm. Previous contributions have concluded that projecting HAp particles around 75 µm, allows them to maintain their crystalline phase in the coating. However, under these conditions, particles do not reach the melting state to promote the splat formation and coating built-up [2,3].

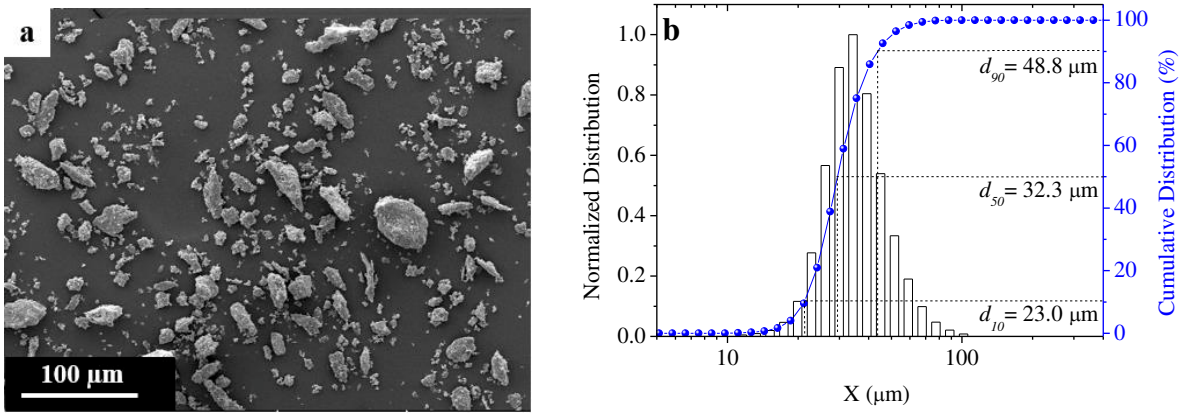

Figure 1. SEM micrograph and cumulative particle size distribution of the obtained BHAp for thermal spray.

On the other hand, spraying powders with size distributions between 10 µm and 20 µm promote the formation of ACP, CaO and TCP phases in the coating due to their high melting state compared to bigger particles [4]. Thus, the intermediate size distribution of BHAp between 30 µm and 50 µm is suitable to be used as feedstock in the fabrication and analysis of coatings deposited by HVOF and APS techniques.

1.1.2. BHAp feedstock powders structural characterization by Fourier Transformed Infra-Red spectroscopy (FTIR)

FTIR spectra analysis of BHAp powder is presented in Figure 2, where the typical vibrational modes of HAp are found. The most intense bands at 1061 cm^{-1} and 1093 cm^{-1} correspond to the vibrational mode *v3* of PO_4^{3-} [5] and the bands of the *v4* vibrational modes of PO_4^{3-}group are also present but with lower intensities at 573 cm^{-1}, 601 cm^{-1}, 634 cm^{-1}, and 962 cm^{-1} [6–8].

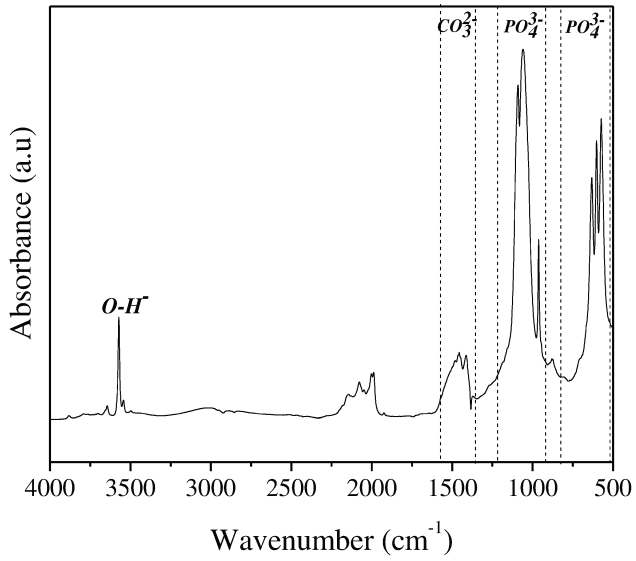

Figure 2. Structural characterization of BHAp by FTIR analysis.

Furthermore, bands at 878 cm^{-1} (*v2*), 1413 cm^{-1} (*v2*) and 1465 cm^{-1} (*v3*) are related to CO_3^{2-} vibrational modes and a narrow band of OH^- in HAp structure is identified at 3572 cm^{-1} [9]. The bands of CO_3^{2-} vibrational modes are evidence of CO_3^{2-} → PO_4^{3-} substitutions on the BHAp structure [7,10–12]. Hence, this bioceramic is mainly a B-type- carbonated apatite due to its biological source. In addition to some ions substitutions (i.e. K^+, Na+, Mg^{2+}, F^-, Cl^-, SiO_4^{4-}), CO_3^{2-} → PO_4^{3-} represents an advantage to increase the feedstock bioactivity rates [13]. Despite the presence of the CO_3^{2-} vibrational modes, OH^- bands are also distinguished. Hence, CO_3^{2-} → PO_4^{3-} substitution is not complete and the BHAp is partially B-type HAp. Finally, the lack of bands between 1620 cm^{-1} – 1680 cm^{-1}, 525 cm^{-1} - 550 cm^{-1} and the band at 1150 cm^{-1} shows that there are not HPO_4^{2-} groups or organic molecules as methylene or amides [5–7,14,15]. As a result, the current feedstock powder can be represented by the formula (1):

$$Ca_{8.1}Mg_{0.2}(PO_4)_{4.3}(CO_3)_{1.7}(OH)_{0.3} \quad (1)$$

1.1.3. BHAp feedstock powders density analysis by He pycnometry

The density of the BHAp measured by helium pycnometry is presented in Table 1. The BHAp density is 0.03 g/cm^3 less compared to the theoretical density of stoichiometric HAp [16] which is expected due to the $CO_3^{2-} \rightarrow PO_4^{3-}$ carbonate substitutions in the BHAp. This difference represents a minimum effect for the feeding of the powder for thermal spray in comparison with the powder feeding of HAp

Table 1. BHAp feedstock powder density

	Density (g/cm^3)	**SD (g/cm^3)**
BHAp	3.1338	0.001

1.1.4. BHAp feedstock powders structural characterization by x-ray diffraction analysis (XRD)

The XRD characterization of BHAp powder is shown in Figure 3. In the XRD pattern of the feedstock powder, a single HAp phase was identified according to the JCPDF 9-432 with the theoretical lattice parameters $a = b = 9.432$, $c = 6.881$, hexagonal structure and *Ca/P ratio* = 1.67 [17]. It is well known that the XRD pattern of highly crystalline biological HAp is identical to the stoichiometric one, and the differences between them are noticed only in the crystallographic parameters [18–20]. Therefore, changes generated in the structural parameters of BHAp by the presence of ions as Mg^{2+} and Na^+ were calculated from the Rietveld refinement and the comparison with the values of the PDF card. The results are presented in Table 2. The slight differences in the lattice parameters of BHAp powders, are related to the variations on the number of $Mg^{2+} \rightarrow Ca^{2+}$ and $CO_3^{2-} \rightarrow PO_4^{3-}$ substitutions and depend on the bovine source (age, bone type, among others). It is known that the incorporation of CO_3^{2-} ions on the apatite structure causes a contraction in *a*-axis and expansion on the *c*-axis [21]. Thus, BHAp has a lower lattice parameter *a* and higher *c* compared to theoretical HAp. Furthermore, the calculated *Ca/P ratio* suggests that the BHAp powder is calcium deficient compared to stoichiometric HAp and this is attributed to the $Mg^{2+} \rightarrow Ca^{2+}$ substitutions and Ca^{2+} sites vacancies.

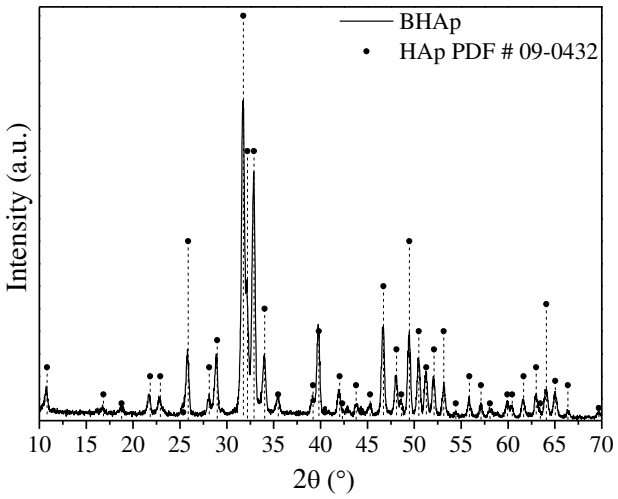

Figure 3. Structural characterization of BHAp by XRD analysis.

Table 2. Structural parameters of HAp and BHAp

	Hydroxyapatite						
	Phase %	a (Å)	c (Å)	Ca/P	Crystallite size (Å)	Cell Volume ($Å^3$)	χ^2
HAp [17]	-	9.432	6.881	1.67	-	528.8	-
BHAp [20]	-	9.429	6.885	-	-	-	-
BHAp feedstock	100	9.419	6.886	1.64	2752.98	529.08	1.62

1.2.COMMERCIAL AND LAB-MADE BG45S5

1.2.1. Commercial and lab-made BG45S5 feedstock powders structural characterization by x-ray diffraction analysis (XRD)

The XRD diffractograms in Figure 4 presents the structural analysis of the commercial BG45S5 and the lab-made BG45S5 obtained at IRCER and Cenaprot facilities. The two Lab-made and the commercial BG45S5 shows similar XRD patterns without any crystalline diffraction peak between the 20 – 70 ° 2θ range. Furthermore, broadband between 20 – 35 ° 2θ was also part of all the XRD diffractograms. This band is characteristic in glassy and amorphous materials and related to diffusion phenomena that occur in the glass fabrication where there is not a long-range order within the BG matrix [22,23]. The used method to fabricate both lab-made BG45S5

allows obtaining the desired glass structure compared to the commercial BG45S5 and previous contributions, in as much as the amorphous structure increases the bioactivity of the bioactive glasses when is in contact with body fluid. The structure of BGCenaprot powders was crystalline when the precursor's mixture was melted at a maximum temperature of 1250 °C as proposed for BGIRCER (see Figure 5). The amorphous arrangement of bioactive glasses is the structural characteristic that enhances the bioactivity of the glass.

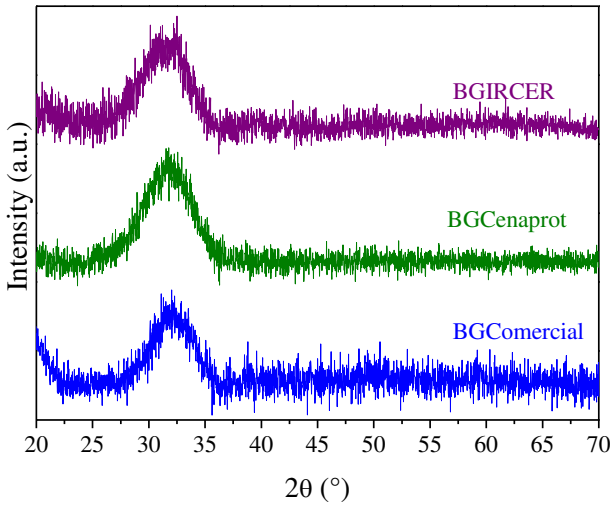

Figure 4. Structural characterization of lab-made BG45S5 and commercial BG45S5 by XRD.

Moreover, it is well known that the fast quenching of the glass assures the amorphous characteristic in its fabrication process. The unique experimental difference between both lab-made glasses was the type of oven where the melting was performed.

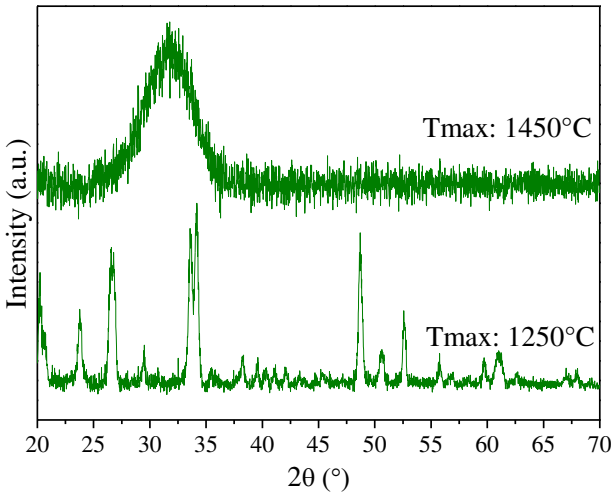

Figure 5. Structural characterization of lab-made BG45S5 Cenaprot fast quenched after heat treatment at 1250 °C and 1450 °C by XRD.

The extraction of the Pt crucible to quench fast the mixture in water was slower by using the vertical oven in the method used to fabricate BGCenaprot. This is a consequence of the low velocity of the base in the vertical oven set up to extract the sample. Thus, the structure of the BGCenaprot melted at 1250 °C and fast quenched, shows the typical crystalline diffractogram of the BG45S5 [24]. However, this was not the desired structural characteristic in the obtained glass. Since it was not possible to increase this velocity and, consequently, to reduce the time to quench the precursor's mixture, a solution to obtain the amorphous glass was to increase the maximum temperature of the heat treatment at 1450 °C. This, increased the disorder of the BG45S5 arrangement just before the fast quenching, allowing to obtain the amorphous bioactive glass despite the lower cooling rate compared to the rate used in the BGIRCER fabrication. The diffractograms of crystallized BGIRCER, BGCenaprot, and BGSchott after thermal treatments at 750 °C and 950 °C are shown in Figure 6. both glasses present a crystalline structure at 750 °C A broadening and separation of the main peak in two other peaks are noticed after crystallization at 950 °C for all the samples.

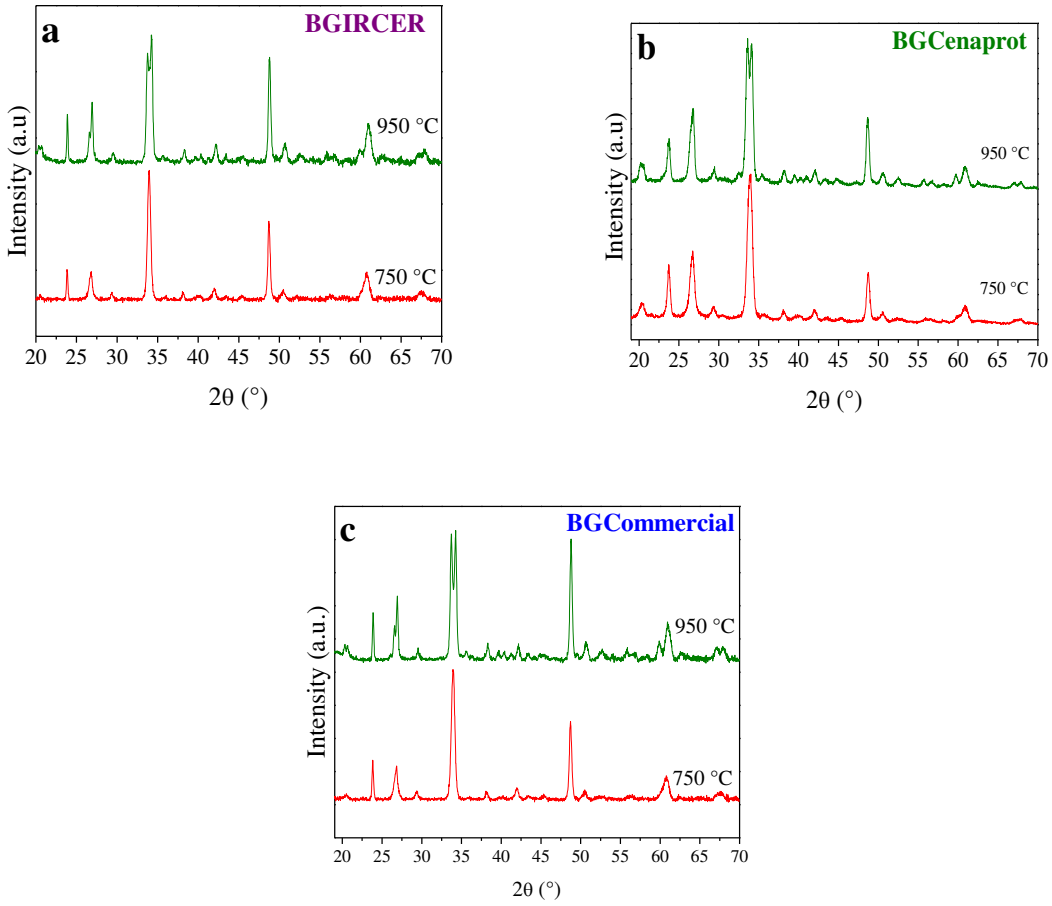

Figure 6. Structural analysis of crystallized BG45S5 at 750 °C and 950 °C: a) Lab-made BG45S5 IRCER, b) Lab-made BG45S5 Cenaprot and c) Commercial BG45S5.

The $Na_{5.27}Ca_3Si_6O_{18}$ phase with the main diffraction peak at ≈ 33.5 ° 2θ after a nucleation process in the glass surface at 750 °C was identified in all diffractograms according to the ICSD 98-002-3058. The crystallization of the BG45S5 starts between 600 – 670 °C [25], thus, the crystallized phase at 750 °C is associated with a Na-rich natural analog and isostructural phase to the combeite structure here identified [26]. On the other hand, the split of the main crystalline phase at 750 °C in two peaks after 950 °C occurs due to the lattice parameter variations where *c* is increased and *a* decreased. It is well known that this split occurs as a consequence of the start of the transformation from $Na_{5.27}Ca_3Si_6O_{18}$ to silicocarnotite phase ($Na_2Ca_4(PO_4)_2SiO_6$) [24,27]. The *a* and *c* lattice parameters changes are attributed to the incursion of orthophosphate ions into the $Na_{5.27}Ca_3Si_6O_{18}$ unit cell. An expected small peak of $Na_2Ca_4(PO_4)_2SiO_6$ at ≈ 32.55 ° 2θ reported by L. Lefevbre et al. was only found on BGCenaprot sample treated at 950 °C [24]. This may be a consequence of the scan XRD measurement resolution and the glass crystallization kinetics which depends also on the thermal treatment conditions and bulk characteristics (i.e. size, morphology) [28]. Nevertheless, the main peak separation in all samples due to incursion of orthophosphate ions into the $Na_{5.27}Ca_3Si_6O_{18}$ unit cell and the initial stages of silicocarnotite phase formation allows concluding that all samples undergo the same structural changes agreeing with the structural changes in commercial BG45S5. In consequence, the structural analysis of the lab-made and commercial BG45S5 powders shows that the structural changes by crystallization are the same for all the samples following the same crystallization kinetics of the 45S5 bioactive glass composition.

1.2.2. Commercial and lab-made BG45S5 compositional oxides analysis by x-ray fluorescence (XRF)

The oxides composition of lab-made and commercial BG45S5 obtained by XRF is presented in Figure 7. The nominal composition of the BG45S5 glass was added for comparative purposes.

The commercial BG, BGIRCER, and BGCenaprot present a SiO_2 content of 45.07, 44.88 and 45.75, respectively. Regarding CaO and Na_2O_3, the higher variation of the content of the oxides was 0.47 % in all samples compared to the nominal BG45S. Finally, the P_2O_5 content was similar to the nominal value of this oxide in the 45S5 configuration. The higher variation of P_2O_5 content was 0.09 %. The obtained results in the XRF analysis are closer to the theoretical oxide composition of BG45S5 in comparison with previous reports [29,30]

Moreover, the weight and mixing steps used in the fabrication methodology were adequate to maintain the desired oxides composition after melting and fast quenching. Additionally, the selection of Na_2CO_3 as a precursor of Na_2O and the decarbonization stage proposed in the fabrication of the glass are an effective alternative to fabricate bioactive glasses. Based on the oxide's composition measurement by XRF it is concluded that the obtained glass accomplishes the 45S5 configuration.

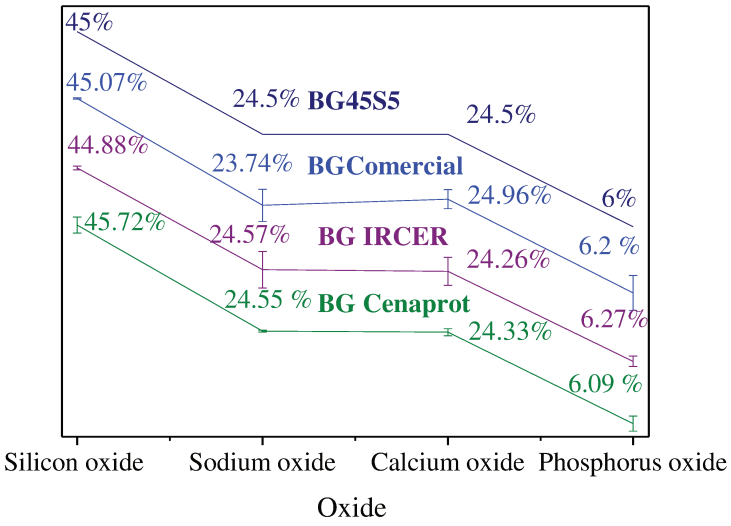

Figure 7. Oxides composition in wt. % of lab-made BG45S5 and commercial BG45S5 obtained by XRF.

The Bioactive glass Network Connectivity (N_c) or degree of cross-linking and connectivity in silica (Number of bridging oxygens per silica tetrahedron) is calculated by using the quantification obtained in the XRF analysis [31] following equation 1.

$$Nc = 2 + \frac{BO - NBO}{G} \tag{1}$$

From equation (1), BO = bridging oxygens per network forming ion, NBO = non-bridging oxygens per network modifier ion and G = total number of glass-forming units. Hence, the N_c is calculated, based on the wt % of the oxides using equation 2,.

$$Nc = 2 + \frac{[(2 \times SiO_2) + (2 \times P_2O_5)] - [(2 \times Na_2O) + (2 \times CaO)]}{[SiO_2 + (2 \times P_2O_5)]} \tag{2}$$

Since equation 2 employees the mol % of the oxides in the BG to estimate the N_c value, the calculated compositions of the oxides in mol % are presented in Table 3. The N_c value of the bioactive glasses was calculated following equation 2 and the mol % of oxides (see Table 4).

The N_c of commercial and lab-made bioactive glasses was in the range of 2.09 and 2.13. It is well known that some properties of silica-based bioactive glasses can be predicted based on the NC value. For instance, the rate of apatite formation of the surface and *in-vivo* osteoconduction and crystallization tendency [32].

The rate of apatite deposition and percentage of newly formed bone is higher when the N_c value is close to 2 and it is decreased at higher values. At greater N_c = 2.4 glasses are not considered as bioactive

Table 3. Oxides composition in mol % of lab-made BG45S5 and commercial BG45S5 calculated form XRF analysis.

	Theoretical oxides composition of BG45S5	**BG Commercial**	**BG IRCER**	**BG Cenaprot**
SiO_2 mol %	46.13	45.72	46.18	46.28
Na_2O mol %	24.35	23.93	24.45	24.31
CaO mol %	26.91	27.76	26.68	26.81
P_2O_5 mol %	2.6	2.726	2.717	2.68

Table 4. Network Connectivity of commercial and Lab-made bioactive glasses.

	Nominal BG45S5	**Commercial BG**	**BG IRCER**	**BG Cenaprot**
NC	2.12	2.09	2.13	2.13

. Based on the findings and in the *in-vitro* and *in-vivo* model proposed by S. Fujibayashi *et al.* [33], commercial and lab-made bioactive glasses promote the apatite formation on its surface after 0.9 and 1.2 days in biological media, respectively. In addition, the percentage of new bone that is formed on the studied glasses is predicted to be 51 % and 49 % for commercial and lab-made bioactive glasses, respectively. This higher bioactivity and osteoconduction is due to the increased tendency of the glass to degradation at lower N_c values. Consequently, it is valid to predict high bioactivity and *in-vivo* osteoconduction of the studied commercial and lab-made bioactive glasses.

1.2.3. Commercial and lab-made BG45S5 feedstock powders thermal analysis by differential scanning calorimetry (DSC)

The thermal characterization by means DSC analysis of the commercial and lab-made bio-glasses is presented in Figure 8 and Figure 9. Figure 8 shows the DSC thermogram of the first set of lab-made bioactive glasses melted using 24.5 % of Na_2CO_3 instead of 24.5 % of Na_2O. The commercial bioactive glass DSC is also added. Commercial BG45S5 DSC presents a first slope change at 541 °C followed by the start of an exothermic peak at 610 °C. Additionally, there is a change on the slope after this first exothermic peak after at 820 °C. Finally, an endothermic reaction is noticed with a small shoulder at 1192 °C and the center of the peak at 1235 °C. On the other hand, the thermograms of both lab-made bioactive glasses present a similar pattern with the first slope change at ~ 600 °C. Moreover, the start of the first endothermic reaction in BGCenaprot and BGDSC analysis starts at 762 °C and 799 °C, respectively. Finally, two endothermic peaks between 1080 and 1120 °C are seen.

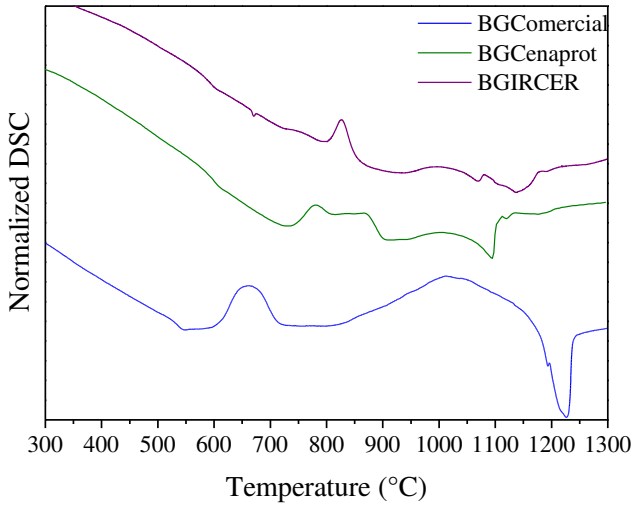

Figure 8. DSC.analysis lab-made bioactive glass prepared with 24.5 wt% of Na_2CO_3 and commercial BG45S5

Commercial BG45S5 DSC analysis shows the typical thermogram of BG45S amorphous glass. The first slope change at 541 °C indicates the first glass transition temperature (T_{g1}) The start of the first endothermic peak at 610 °C shows the characteristic crystallization temperature of the glass (T_c). Furthermore, the slope change at 830 °C is related to the second glass crystallization temperature (T_{g2}) of BG45S5. The last endothermic peaks at 1192 °C and 1235 °C are associated with the melting temperatures T_{m1} and T_{m2} which are attributed to the melting of two crystalline phases [27]. The firsts set of lab-made bioactive glasses are Na_2O deficient.

As this oxide is a network disrupter [34], the lab-made bioactive glasses follows a different glass formation with different characteristics temperatures. The thermogram of the lab-made bioactive glasses with 24.5 % wt.of Na_2O to obtain the BG45S5 configuration is shown in Figure 9. Both thermograms present a similar pattern with a first slope change at 536 °C, followed by a peak at 720 °C which starts at 660 °C and a slope change at 840 °C. Finally, two peaks are noticed at 1190 °C and 1214 °C.

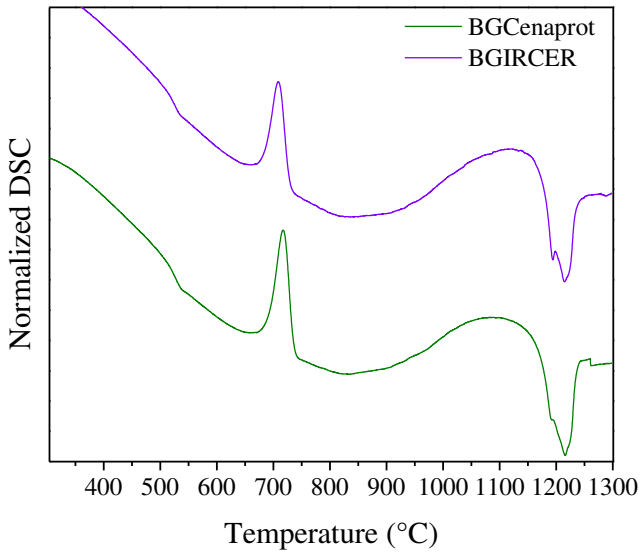

Figure 9. DSC.analysis of lab-made BG45S5 prepared with 24.5 wt % of Na_2O

The thermograms of both lab-made bioactive glasses are similar to the DSC analysis of commercial BG45S5. Thus, the glass transition temperatures T_{g1} = 536 °C and T_{g2} = 840 ° and crystallization temperature T_c = 660 °C are characteristic temperatures of sintering starting stage and silicate phase crystallization of BG45S5, respectively. The maximum value of the first endothermic peak at 720 °C is attributed to the starting of lattice change in the silicate crystalline phase. The melting temperatures T_{m1} = 1190 °C and T_{m2} = 1214 °C are in agreement with the melting temperatures of commercial BG45S5 as expected. The characteristic temperatures of commercial and lab-made bioactive glasses with the proper content of Na_2O agreeing with the thermal analysis results of BG45S5 presented in other contributions [24,28,32,35,36]. The slight differences in the characteristic temperatures of commercial, lab-made and previously reported BG45S5 are due to differences in particle size distribution [37] and the morphology of the particles [38]**.** Nevertheless, the performed DSC analysis of the lab-made BG is in agreement with the analysis of amorphous commercial BG45S5 and previous

thermal studies of the same BG, confirming the findings on the XRF and XRD studies performed in this contribution.

Figure 10 shows the thermal analysis of oxides and carbonate mixture by DSC during the glass melting. Three differentiable zones are presented in the thermogram. In the first zone before 250 °C, the mass change occurs due to water loosening within the powder. The Si-O-Si destabilization and the P_2O_5 net former reaction is presented in the zone between 350 °C - 420 °C.

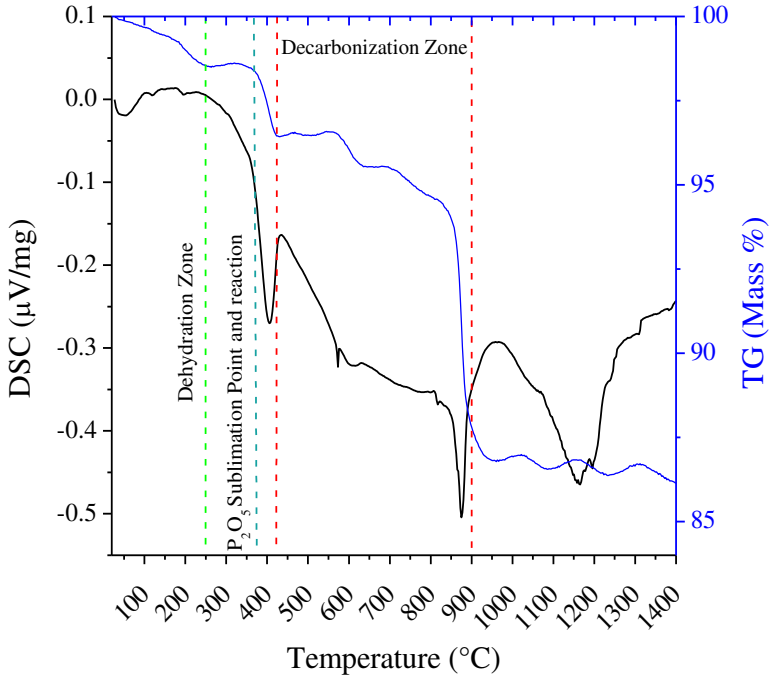

Figure 10. Thermal analysis of oxides and carbonate mixture by DSC during the glass melting.

The P_2O_5 sublimation point at 360°C matches with the first endothermic peak of the DSC. In consequence, the phosphorus oxide is not loosed and starts to break the SiO_2 net as expected. This explains the high value of -0.25 µV/mg in the endothermic reaction. Afterward, a decreased TG zone between 450 °C and 900 °C related to the decarbonization of the Na_2CO_3 is presented. Moreover, the action of the Na_2O and CaO as net modifiers in the glass net, are noticed at 800 °C and 860 °C. The typical melting temperatures of the BG45S5 are seen at 1160 °C and 1194 °C. Additionally, the TG curve presents a weight loosening of 12 % which is unambiguously associated with the decarbonization of the Na_2CO_3.

1.2.4. Commercial and lab-made BG45S5 feedstock powders bioactivity analysis after immersion in simulated body fluid (SBF).

The structural characterization of commercial and lab-made bioactive glasses after 21 days of immersion in SBF by XRD is presented in Figure 11. Moreover, the diffractogram of non-immersed powders is also shown. An amorphous diffraction pattern is seen for non-immersed powders. In addition, both diffractograms show a diffraction band between 25 and 35 °2θ. On the other hand, the XRD patterns of the glasses after 21 days of immersion are characterized by the appearance of four peaks at 25 °2θ, 31 °2θ, 40 °2θ and 47 °2θ. The diffractograms of non-immersed bioactive glasses are the typical XRD patterns of amorphous BG45S5 previously analyzed in section 1.2.1. The diffractograms of immersed commercial and lab-made bioactive glasses indicate that the surfaces of both bioactive glasses were modified to a more crystalline structure.

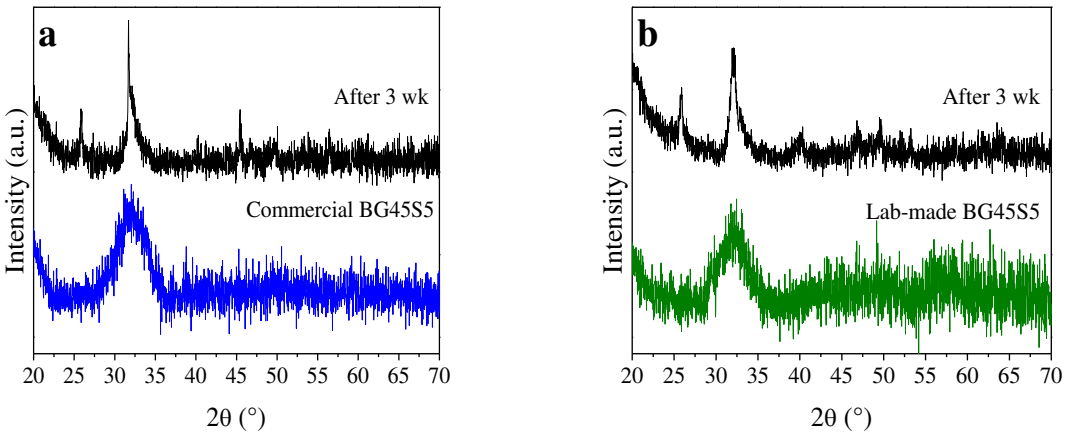

Figure 11. Structural characterization of BG45S5 feedstock powders after 0 and 21 days of immersion in SBF: a) Commercial BG45S5 and c) Lab-made BG45S5.

The diffraction peaks at 25 °2θ, 31 °2θ, 40 °2θ and 70 °2θ are associated with the formation of the apatite layer [39]. This, as a consequence of the ion interchange between the bioactive glass surface and the ions in the SBF solution. Afterward, the deposition of calcium and phosphates groups starts, and the apatite layer is formed. The commercial and lab-made glasses have an apatite structure on their surface after 21 days of immersion in SBF. These results agree with previous reports where similar diffractograms after the same time of immersion are found [39]. Hence, the obtained lab-made glass has the same type of surface modification in interaction with SBF, and consequently, similar bioactivity behavior compared to the BG45S5 glasses.

The pH and concentration of Si, Ca and P in SBF were monitored after 4 h, 8 h, 24 h, 72 h, 1 week, 2 weeks and 3 weeks (see Figure 12). In Figure 12a an increasing trend of the pH is noticed starting in the range of 7.5 - 7.6 and increased to 7.9 - 8 for commercial and lab-made bioactive glasses. However, there is a pH drop to 7.35 - 7.4 during the first 4 h before the continuous increment. Similarly, Si concentration in SBF has an increasing trend from 22 - 23 mg/L to 47 - 50 mg/L with a small drop to 10 - 14 mg/L at 4 h of immersion (see Figure 12b). On the contrary, P concentration in Figure 12c decays from ~ 30 mg/L to ~ 0.1 mg/L in the SBF of commercial and lab-made bioactive glasses during the measured times. A small increase in P content of 5 mg/L is also noticed. Regarding Ca concentration presented in Figure 12d is almost constant with a drop of ~ 50 mg/L at 48 h for commercial BG and a final concentration of 110 - 115 mg/L. This is a similar value compared to the initial concentration of Ca in SBF.

The increasing trend in pH is associated with the cation exchange, predominantly of Na^+ and Ca^{2+} from the glasses with protons from the solution. The pH decay at 8 h, is attributed to the network dissolution in the bioactive glasses surface as expected in the apatite layer deposition. Si release was the greater differential concentration measured in SBF as a consequence of the rapid reaction and reactivity of glass with SBF.

Si concentration follows a similar trend compared to pH as a because of the formed bond with OH- from SBF in the kinetics of the apatite layer formation. Consequently, Si release from both bioactive glasses to the SBF was similar and the network dissolution is considered the same for the commercial and lab-made glasses.

Ca concentration in SBF is decreased due to the Ca deposition in the surface of bioactive glasses after 72 h of immersion and the formation of the Ca-rich layer in the first stages of apatite growth. Afterward, the concentration of Ca is increased by the ion release from the previous Ca-rich layer and its stabilized by the continuous P intake from the SBF to the glasses. P trend occurs as expected showing high bioactivity in both glasses.

All the obtained and results in here analyzed, agreeing with the analysis performed by Maçon *et al.* in the robin round test to evaluate the SBF of bioactive glasses powders by immersion in Kokubo's solution [39]. Therefore, both, lab-made a commercial bioactive glass shows the bioactivity performance of the BG45S5.

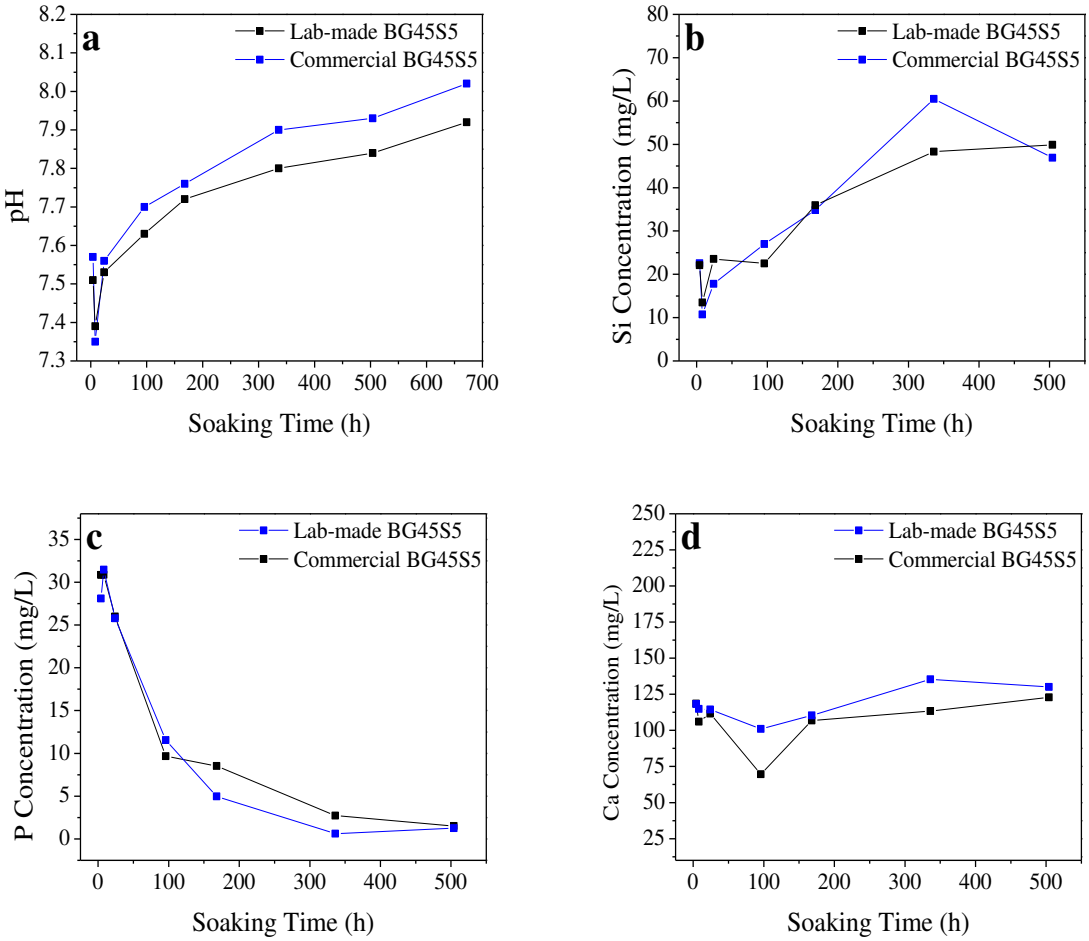

Figure 12. pH and Elements concentration in SBF after 4 hours,8 hours, 24 hours, 72 hours, 1 week, 2 weeks and 3 weeks of BG45S5 feedstock powders immersion in SBF: a) pH, b) Si, c) P and d) Ca.

1.2.5. *Commercial and lab-made BG45S5 feedstock powders particle size distribution, morphology and microstructure characterization by laser diffraction particle sizing (LDPS) and scanning electron microscopy (SEM).*

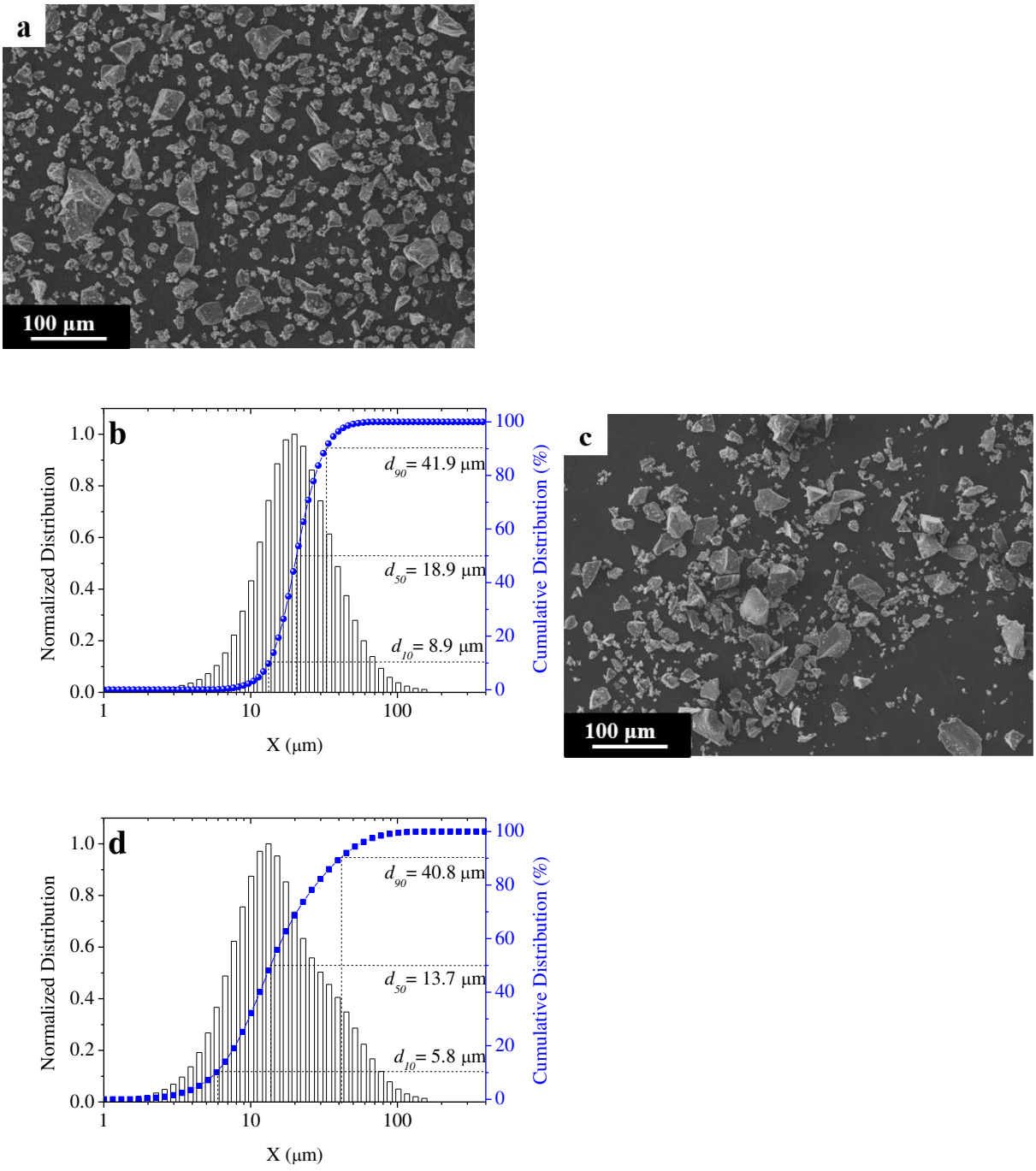

Figure 13. SEM micrograph and particle size distribution of a,b) Commercial BG45S and c,d) Lab-made BG45S5.

Figure 13 presents the morphology and particle size distribution of commercial and lab-made BG45S5. Commercial BG45S5 particle morphology is irregular and it comprises of flat faces

and pronounced edges (see Figure 13a). Furthermore, heterogeneous sizes and shapes are also noted. The particle size of this powder in Figure 13b shows symmetric distribution with deciles 10 and 90 of 8.9 µm and 41.9 µm, respectively. Regarding lab-made BG45S5 morphology presented in Figure 13c is very close to the commercial glass. The differences in the particle sizes in the SEM micrographs are due to the preparation of the sample. This is evidenced in the size distribution in Figure 13d showing a normal distribution similar to the one presented in Figure 13b, with a small positive skew and deciles 10 and 90 of 5.8 µm and 40.8 µm, respectively. Commercial BG45S5 size is in agreement with the powder datasheet which reports a $d_{50} = 16 \pm 4$ µm [40]. Thermally sprayed bioactive glass with feedstock powders with particle size distribution under 63 µm, leads to reduce the amount of inter-splat cracks [29]. Despite de difference of 5 µm between the d_{50} values from commercial and lab-made BG45S5, their distribution behavior in thermal spray should be comparable.

1.2.6. Commercial and lab-made BG45S5 feedstock powders density analysis by He pycnometry

The values of the density of commercial and lab-made bioactive glass are listed in Table 5. The density of commercial BG45S5 was 2.671 ± 0.016 g/cm^3 and 2.683 ± 0.002 g/cm^3 lab-made for the lab-made bioglass. The studied glass densities differ in values of less than 1 % in comparison with the theoretical density of BG45S5 (2.7 g/cm^3) [32]. This difference is not significant since BG45S5 obtained by the same melt and quenching method has been reported in a range of 2.707 – 2.825 g/cm^3 [41,42]. These slight variations are related to differences in particle size, superficial area and small differences of Na_2O content within the glasses. Since Na_2O expands the glass network and in consequence decreases the glass density, it's content increments decrease the density of the entire glass [34]. Hence, it can be assumed that the obtained lab-made bioactive glass shows the density of the BG45S5 structure and it is closer to the theoretical value compared to the commercial BG45S5 density.

Table 5. Commercial and lab-made 45s5 bioactive glasses density

	Density (g/cm³)	**SD (g/cm³)**
Commercial BG	2.6926	0.0011
Lab-made BG	2.6996	0.001

1.2.7. Commercial and lab-made BG45S5 feedstock powders structural characterization by Fourier transformed infra-red spectroscopy (FTIR)

The FTIR spectra of commercial and lab-made BG45S5 is shown in Figure 14. The spectrograms of both BG45S5 present similar absorption bands between 400 cm^{-1} and 1200 cm^{-1}. A first band is seen at 476 cm^{-1} followed by a shoulder at 591 cm^{-1}. Finally, two close absorption bands at 929 cm^{-1} and 1011 cm^{-1} are also noticed.

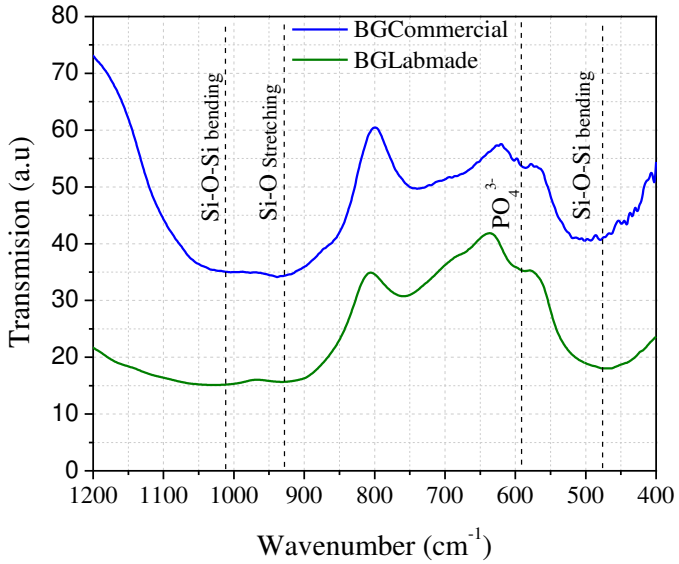

Figure 14. Structural characterization of commercial and lab-made BG45S5 by FTIR.

Bands of BG45S5 glasses at 929 cm^{-1} and 1024 cm^{-1} belongs to the stretching vibrational modes of Si-O-Si [43]. Specifically, vibrational mode at 929 cm^{-1} is associated with Si-O-2_{NBO} (non-bridging oxygen) bound to Na^{+} and Ca^{2+} in the 45S5 structure [43,44]. Furthermore, the band at 476 cm^{-1} is attributed to the Si-O-Si bending mode and indicates the presence of amorphous silicate [24,44]. Another amorphous oxide is evidenced by the presence of the 591 cm^{-1} band which belongs to amorphous P_2O_5 [24]. The lack of bands associated with the vibrational modes of crystalline BG45S5 (i.e. 729 cm^{-1}, 788 $cm^{-1,}$ and 839 cm^{-1}) supports the findings in the XRD analysis where the amorphous structure of the bioactive glass was evidenced [44,45].

1.3.LAB-MADE BG45S5 + Bi_2O_3

After obtaining the bioactive glass by the proposed methodology and assuring that this procedure was suitable for preparing the composition 45S5 and its possible variations, Bi_2O_3 was added to the oxides and carbonate mixture before the melting and fast quenching stage.

The influence of the addition of this new oxide in the BG45S5 structure, radio-opacity, and thermal behavior is here described. As mentioned before, the quantity of Bi_2O_3 which represents the minimum thermal and structural changes and maximizes the radio-opacity is selected to prepare feedstock powders to fabricate thermally sprayed coatings.

1.3.1. Lab-made BG45S5 + Bi_2O_3 feedstock powders structural characterization by x-ray diffraction analysis (XRD)

The XRD structural analysis of BG45S5 with the additions of Bi_2O_3 in different compositions was performed and presented in Figure 15. The XRD patterns present no diffraction peaks in the range of 20-70 °2θ. A diffraction pattern is noticed in all diffractograms in the range of 25 – 35 °2θ. Additionally, a small change in the pattern is detected between 43 and 47 °2θ.

All the diffractograms do not differ from the XRD pattern of the amorphous BG45S5 without Bi_2O_3.

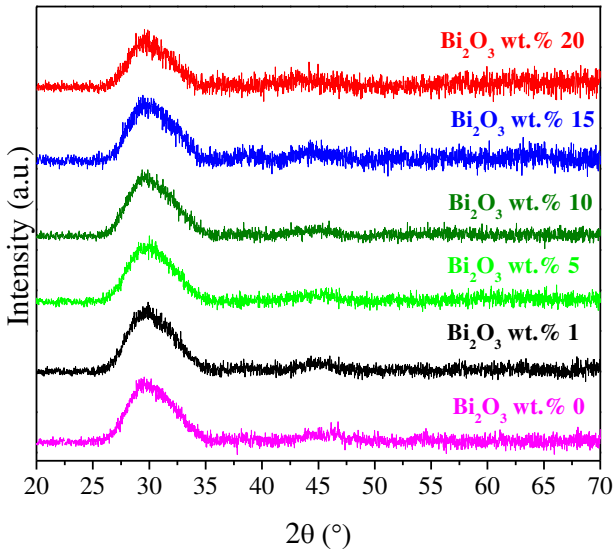

Figure 15. Structural characterization of lab-made BG45S5 + Bi_2O_3 by XRD.

The detected diffraction band between 25 and 35 °2θ is characteristic from the amorphous BG45S5 as mentioned in section *1.2.1.* This band is related to the near atom order in Silica glasses and the similarity between all XRD patterns indicates that this diffraction band is not affected by the presence of Bi_2O_3. Thus, the used process to fabricate the glass and quantities of Bi_2O_3 has no influence on the fabrication of amorphous bioglass. On the other hand, the change in the pattern detected between 43 and 47 °2θ is not associated with any structural characteristics of all the samples and could be caused by the sample scattering.

Since the understanding of the influence of Bi_2O_3 on BG45S5 structure was not clear because of the amorphous character of the glass and the similar XRD patterns, all the samples were crystallized and characterized by XRD analysis (see Figure 16). Two glasses with additions of 11.25 and 13.75 wt. % were fabricated and crystallized under the same parameters and included in the study. This, in order to increase the available data in the range between 10 and 15 wt. % of added bismuth oxide. Furthermore, BG45S5 + 20 wt. % Bi_2O_3 sample was not included in this analysis inasmuch as the glass was fully melted and attached to the crucible surface.

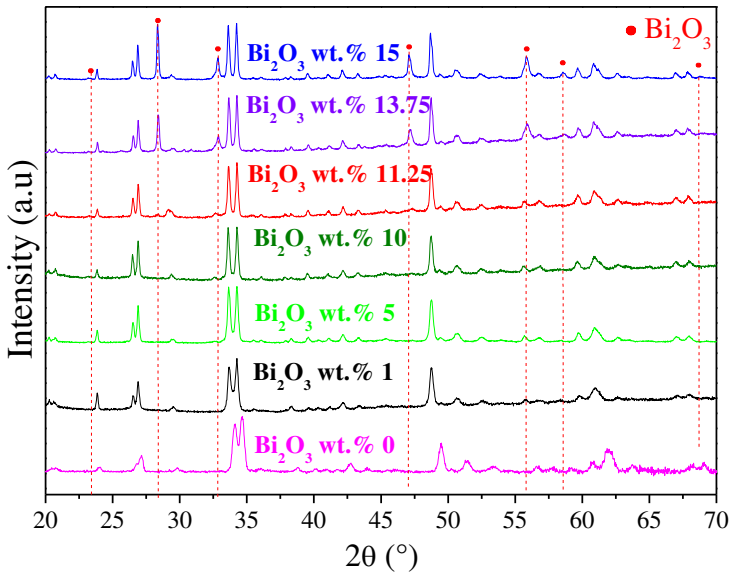

Figure 16. Structural analysis of crystallized lab-made BG45S5 + Bi_2O_3 at 1060 °C by XRD.

XRD patterns of BG45S5 with 0, 1 and 5 in total wt. % of Bi_2O_3 shows the characteristic peaks of the $Na_{5.27}Ca_3Si_6O_{18}$ phase at 23.8, 26.5, 26.8, 33.8 and 34.2 °2θ (ICSD 98-002-3058). Additionally, peaks from the diffraction of crystalline Bi_2O_3 (ISCD 98-003-8436) are identified at 28.3, 32.8, 47, 55.8 and 58.5 °2θ. The intensity of these peaks is increased progressively from the sample with 0 to sample with 15 wt. % of Bi_2O_3. Moreover, the mean width of the peaks of $Na_{5.27}Ca_3Si_6O_{18}$ phase is decreased and the difference of split between the diffraction peaks at 33.8 and 34.2 °2θ is increased. Despite the presence of the Bi_2O_3 in different concentrations in the bioactive glasses, the peaks diffraction of the $Na_{5.27}Ca_3Si_6O_{18}$ are maintained in all XRD patterns with slight positions shifts. This indicates that the Bi is not entering within the $Na_{5.27}Ca_3Si_6O_{18}$ crystalline structure a no other crystalline phase is formed. Moreover, the progressive increase of the intensity of the Bi_2O_3 peaks at the same positions shows that there are no occupied sites of the elements from the BG45S in the unit cell of the bismuth oxide

crystalline phase. The percentage of Bi_2O_3 phase was obtained by the Rietveld analysis of XRD patterns and it is presented as a function of the Bi_2O_3 content in the BG45S5 in Figure 17.

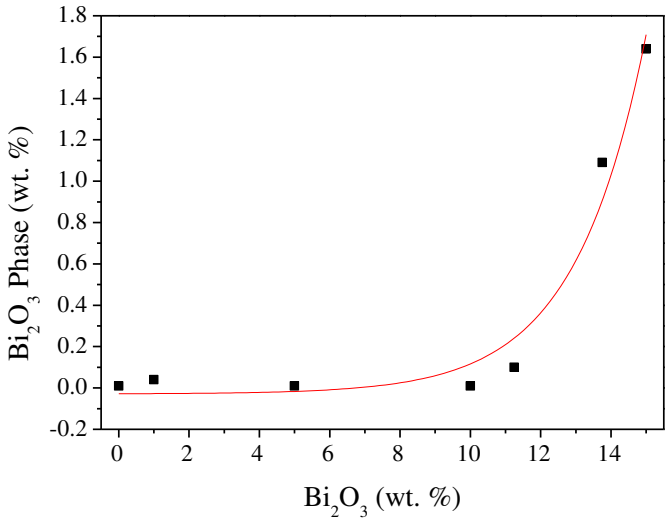

Figure 17. Bi_2O_3 percentage in the crystalline structure of lab-made BG45S5 + Bi_2O_3.

The calculated Bi_2O_3 phase percentage was negligible (0.0175 ± 0.015 %) in samples with additions until 10 wt. % of bismuth oxide. This phase increased to 0.1 % in the sample with 11.25 wt. % of Bi_2O_3 added in the BG. Afterward, the quantified phase increased following a positive exponential function from 0.1 % to 1.64 % in the sample with 15 wt. % of Bi_2O_3. The crystalline phase of Bi_2O_3 was not detected by the XRD and Rietveld analysis before the addition of 11.25 %. This is in agreement with the results of reported bioactive glasses with a maximum addition of 8 wt. % of Bi_2O_3 in its preparation [46]. Bi_2O_3 phase is crystallized with enough periodicity to increase the number of sites of crystalline nucleators and phase content in samples after the addition of 10 wt. % of Bi_2O_3 in the bioglass. This explains the increased intensity of the diffraction peaks and positive exponential tendency growth associated with the Bi_2O_3 phase quantification. On the other hand, its seen that the crystallization of the $Na_{5.27}Ca_3Si_6O_{18}$ is proportional to the crystalline phase of Bi_2O_3. Furthermore, the mean width of the glass crystalline phase is decreased, thus, the crystallinity of the structure was increased. The crystallite size of $Na_{5.27}Ca_3Si_6O_{18}$ crystal as a function of the wt. % of Bi_2O_3 is presented in Figure 18.

From Figure 17 and Figure 18 it can be concluded that the crystallization of Bi_2O_3 and its coexistence with the $Na_{5.27}Ca_3Si_6O_{18}$ phase leads to the crystallinity increasing of the second phase. This is possible since the crystallization kinetics and content of the Bi_2O_3 decreased the

glass viscosity due to the formation of non-bridging oxygen (NBO), increasing the devitrification of glass or glass crystallization [47]. Thus, the narrowing of the diffraction peaks of the $Na_{5.27}Ca_3Si_6O_{18}$ and the crystallite growth of this phase as a function of Bi_2O_3 content is explained.

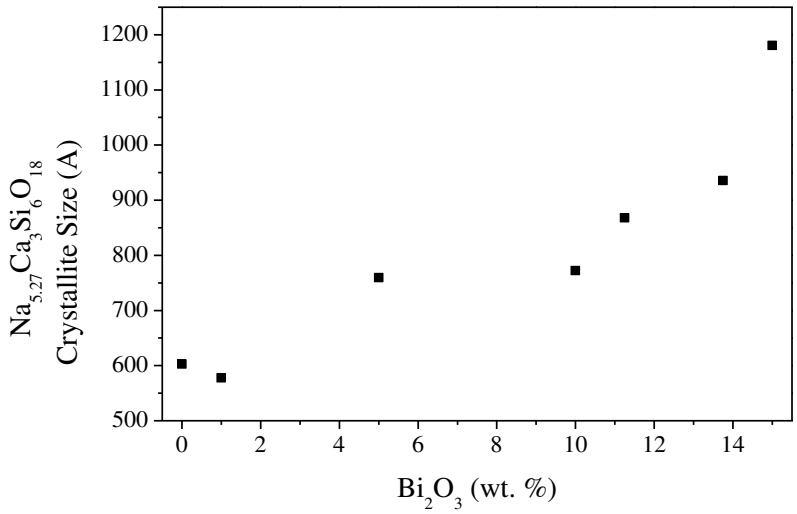

Figure 18. Crystallite size of $Na_{5.27}Ca_3Si_6O_{18}$ phase vs Bi_2O_3 content in lab-made BG45S5 + Bi_2O_3.

The results and analysis here showed allow to conclude that the BG45S5 structure was modified by additions of Bi_2O_3 using more than 10 wt. % of the oxide in its fabrication. Moreover, the presence of Bi_2O_3 induce glass crystallization of amorphous BG45S5 in thermal treatments (i.e. thermal spray) and this tendency is proportional to the Bi_2O_3 content.

1.3.2. Lab-made BG45S5 + Bi_2O_3 feedstock powders thermal analysis by simultaneous thermogravimetry and differential scanning calorimetry (TG-DSC)

DSC curves of the BG + Bi_2O_3 samples are shown in Figure 19. The thermograms present similar DSC curves of BG45S5 samples with 0, 1 and 5 wt. % of bismuth oxide. These curves are characterized by a first slope change between 519 and 528 °C. Furthermore, an exothermic reaction associated with the glass crystallization between 670 and 710 °C and the melting endothermic reactions between 1200 and 1220 °C, are seen. The T_c of this first 3 samples varies from 663, 653 and 648 °C in samples with 0, 1 and 5 wt. % of Bi_2O_3. However, the melting temperatures are constant with values of T_{m1} ~ 1195 °C and T_{m2} ~ 1211 °C. Regarding the thermogram of the sample with 10 wt. % of Bi_2O_3 shows a similar pattern compared to the DSC curve of samples with less bismuth oxide. However, T_c, $T_{m1,}$ and T_{m2} decreased to 638, 1133 and 1193 °C, respectively. Tg was maintained at 518 °C The samples in the range of 15 and 20

wt. % of Bi_2O_3 presents considerable changes in their thermograms. Firstly, the DSC curve of the sample with 15 wt. % shows a second exothermic peak at 623 °C. In addition, the thermogram of the sample with 20 wt. % is highly different compared to the other curves. The exothermic reaction associated with the glass crystallization and melting temperatures in this sample are noticed at 746 °C and 1046 °C, respectively.

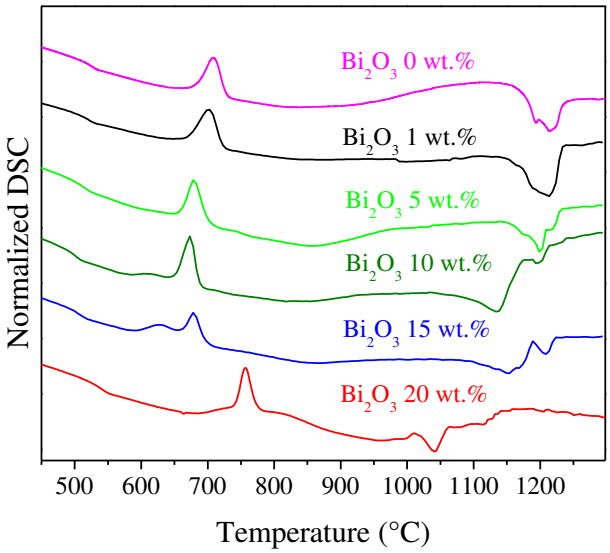

Figure 19. Thermal analysis of lab-made BG45S5 + Bi_2O_3 by DSC

The addition of 1 and 5 % of Bi_2O_3 has a minimum effect on the crystallization of the BG45S5 as was concluded in the previous section (*1.3.1*). Consequently, the T_c was decreased by approximately 20 °C and Tm was constant compared to BG45S5 without Bi_2O_3. T_c is decreased due to the reduction in the glass viscosity caused by the increase in the content of Bi_2O_3 [47]. Despite the small changes in T_c, T_{m1} and T_{m2} were not decreased, the modifier role of bismuth oxide was negligible, and the content was not enough to reduce the melting temperatures. On the contrary, the melting temperature of BG45S5 + 10 wt. Bi_2O_3 sample was reduced ~ 60 °C which indicates that the modifier role of Bi_2O_3 in the melting temperatures of the glass was noticed by adding 10 wt. % of this oxide. Nevertheless, this reduction is small in comparison with the T_m of samples with 15 and 20 wt. %. In addition, the T_c value is still close to the T_c value of BG45S5. In consequence, the structure of the BG45S5 with 10 wt. % was not significantly modified as it was concluded in the XRD analysis in section *1.3.1*.

1.3.3. Lab-made BG45S5 + Bi_2O_3 feedstock powders radio-opacity characterization

The radio-opacity of BG45S5 pellets with different additions of Bi_2O_3 was measured and shown in Figure 20 and Figure 21. Commercial and lab-made BG45S5 without Bi_2O_3 were also analyzed for comparative purposes. A sample set of radiographic images of the pellets next to the Al reference is shown in Figure 20. The image in Figure 20a presents the pellets of commercial (left) and lab-made (right) BG45S5 without Bi_2O_3. The first step of the Al reference on the left side has a thickness of 0.5 mm. The opacity of both pellets is similar to the opacity of the second step of the Al reference. Pellets with 1 (left) and 5 wt. % (right) of Bi_2O_3 in the radiographic image from Figure 20b presented an opacity comparable to the steps with thicknesses of 1 and 1.5 mm, respectively. In this figure, there is a mark on the left side of the image that indicates the place before the first step of the Al step-wedge.

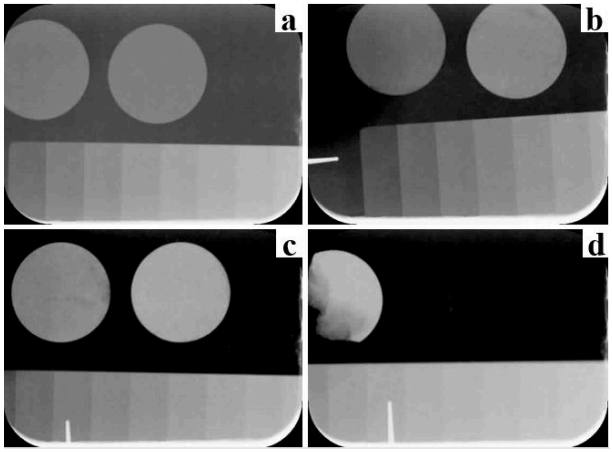

Figure 20. Radiographic images of lab-made BG45S5 + Bi_2O_3 pellets. a) 0 wt. % Bi_2O_3 (left) and commercial BG45S5 (right), b) 1 wt. % Bi_2O_3 (left) and 5 wt. % Bi_2O_3 (right), c) 10 wt. % Bi_2O_3 (left) and 15 wt. % Bi_2O_3 (right), and d) 20 wt. % Bi_2O_3.

On the other hand, Figure 20c and Figure 20d show this mark at the step with a thickness of 4 mm. In Figure 20c pellets with 10 and 15 wt. % of Bi_2O_3 are placed next to the Al reference at the left and right sides, respectively. As is seen in the figure the opacity of the pellet on the right side is higher and comparable with the step with 4 mm of thickness. Finally, a fragmented pellet of BG45S5 with 20 wt. % of Bi_2O_3 is observed in Figure 20d. The fragmentation of the pellet after manipulation for the measurement was caused by the pellet high brittleness associated with the high content of Bi_2O_3 and the lack of binder use and sintering in its preparation. However, a high area of the pellet was maintained to perform the opacity measurement

More accurate measurements of the pellet's radio-opacity by digital image processing are shown in Figure 21. Firstly, the radiopacities of commercial and lab-made samples without Bi_2O_3 are

statistically considered as equals. Additionally, the pellets' radio-opacity is exponentially increased from samples with 1 wt. % of Bi_2O_3 to 20 wt. %. This tendency starts at ~ 1 mm Al and increased until 5.31 mm Al.

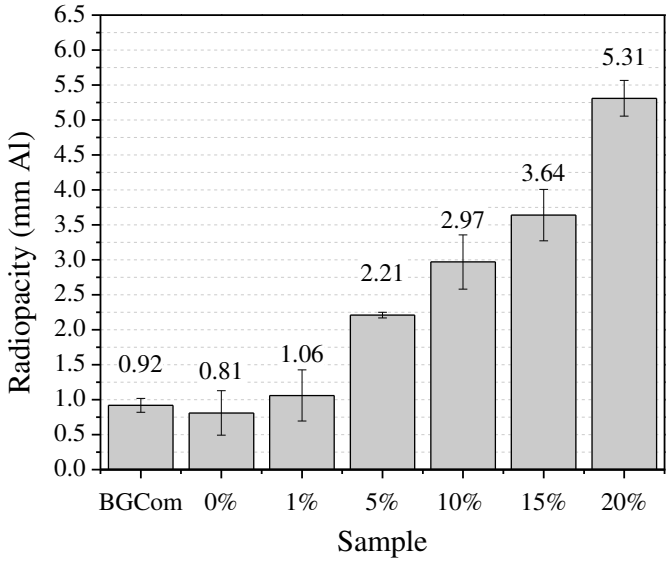

Figure 21. Lab-made BG45S5 + Bi_2O_3 pellets radio-opacity

This tendency follows the exponential growth of the Bi_2O_3 addition in the studied samples. Hence, it is concluded that the radio-opacity is directly proportional to the Bi_2O_3 content, as expected. Therefore, the used melt and fast quenching method allow maintaining the added bismuth oxide content in glasses. Previously BG45S5 + Bi_2O glass reported in the patent US 2012/0148646A1 and fabricated by flame spray pyrolysis presents a lower radio-opacity compared to the obtained glass in this contribution. In the patent, flame derived nanoparticles of BG45S5 with 20 wt. % of Bi_2O_3 shows a radio-opacity of 1.8 mm Al. In contrast, the BG45S5 with 10 % of bismuth oxide fabricated on this contribution has a radio-opacity of 2.97 ± 0.38 mm Al. The higher efficiency in radio-opacity may be associated with the flame spray process considering that in the melt and fast quenching method the incursion of Bi_2O_3 in the glass network is more effective due to the melting temperatures and times of the heating process. The radio-opacity of the sample with 5 wt. % of Bi_2O_3 is higher compared to the one prepared by using 20 wt. % in the flame process. This also supports the hypothesis that the flame spray process conditions do not allow the incursion of the total added Bi_2O_3 in the glass network and, consequently, the radio-opacity is not maximized according to the Bi_2O_3 content. Despite the high radio-opacity of samples with 5 and 20 wt. % of bismuth oxide, the modified structure of the glasses and thermal properties are not in agreement with the BG45S5.

According to the structural, thermal and radio-opacity analysis performed in this section the 10 wt. % was the quantity selected of Bi_2O_3 to increase the radio-opacity of BG45S5. The analyses show that the addition of this quantity allows maintaining the structural and thermal properties of the BG45S5 composition increasing its radio-opacity by ~ 3 times compared to commercial and lab-made BG45S5 without Bi_2O_3. Thus, the feedstock powder of BG45S5 + Bi_2O_3 to fabricate thermally sprayed coatings, either single coating or gradually sprayed, is fabricated with the addition of 10 wt. % of Bi_2O_3.

1.3.4. Lab-made BG45S5 + 10 wt. Bi_2O_3 feedstock powders particle size distribution, morphology and microstructure characterization by laser diffraction particle sizing (LDPS) and scanning electron microscopy (SEM)

The BG45S5 feedstock powder with the selected composition of Bi_2O_3, now named BG45S5 + 10 wt. Bi_2O_3 was prepared and its morphology and size distribution are observed in Figure 22. In Figure 22a irregular shaped particles with flat and dense faces are seen. The heterogeneity of the morphology of the particles is also evidenced. Regarding the particle size, Figure 22a presents a symmetric gaussian distribution with deciles values of d_{10} = 8.4, d_{50} = 18.7 and d_{90} = 38.5. BG45S5 + 10 wt. Bi_2O_3 particle morphology and size are closely similar to the commercial BG45S5. As mentioned in section *1.2.5*, the heterogeneous morphology of particles is due to the milling and sieving process of the glass where elonged particles with low thicknesses passed through the sieving mesh. The used methodology for milling and sieving the BG45S5 + 10 wt. Bi_2O_3 frits was adequate since the differences in the deciles between commercial and BG45S5 + 10 wt. Bi_2O_3 glasses are in the range of 0.2 – 2.4 µm.

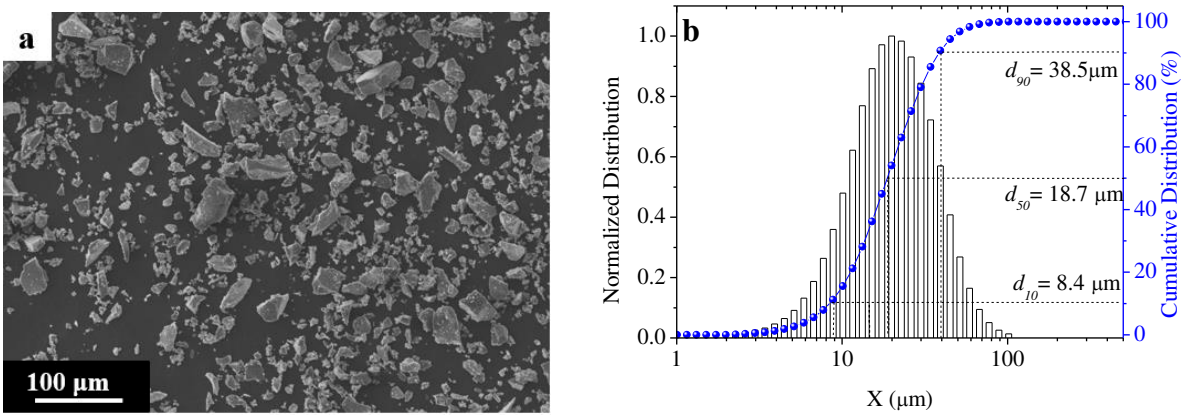

Figure 22. SEM micrograph and particle size distribution of lab-made BG45S5 + 10 wt. % Bi_2O_3.

In consequence, the comparison between thermally sprayed coatings by using commercial and BG45S5 + 10 wt. Bi_2O_3 feedstock powders should be valid.

1.3.5. Lab-made BG45S5 + 10 wt. % Bi_2O_3 feedstock powders density analysis by He pycnometry

The density of the BG45S5 + 10 wt. % Bi_2O_3.powders were measured by He pycnometry and the result is enlisted in Table 6. The density of the BG45S5 was increased by 0.22 g/cm³ due to the higher density of the added Bi_2O_3 [46]. This increment represents an advantage for the objective of this contribution since the densities of the BG45S5 + 10 wt. % Bi_2O_3 and BHAp to be mixed and gradually sprayed are similar. In consequence, the mixture of powders and deposition will be more homogeneous in comparison with mixed powders with significant density differences.

Table 6 Lab-made BG45S5 + 10 wt. % Bi_2O_3 density

	Density (g/cm³)	**SD (g/cm³)**
BG+ 10 wt. % Bi_2O_3	2.916	0.0009

2. CHARACTERIZATION OF THERMALLY SPRAYED COATINGS

2.1.BHAp COATINGS OBTAINED BY HVOF AND APS

2.1.1. APS BHAp powder feeding analysis

Figure 23 presents the different pathways that in-flight particles could undergo as a consequence of the particle kinetic energy and the plasma energy and gases flow in the powders radial feeding:

1. Particles rebound with the plasma and are not deposited on the substrate. Consequently, the powder deposition efficiency is low.
2. Particles enter within the plasma with an unparallel trajectory to the plasma axis, then particle pathways do not follow the plasma axis. Consequently, the powder deposition efficiency is low.

3. Particles enter within the plasma with a parallel trajectory to the plasma axis, then particles pathways follow the plasma axis. Consequently, the powder deposition efficiency is high.
4. Particles pass through the plasma due to the high kinetic energy and are not deposited on the substrate. Consequently, the powder deposition efficiency is low.

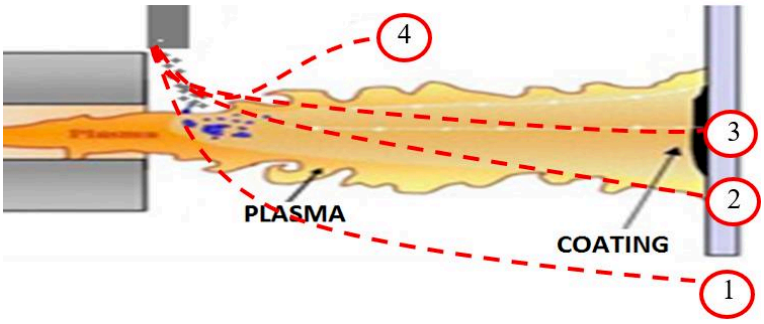

Figure 23. Side schematic view of radial powder feeding in APS. The possible trajectories of in-flight particles are shown.

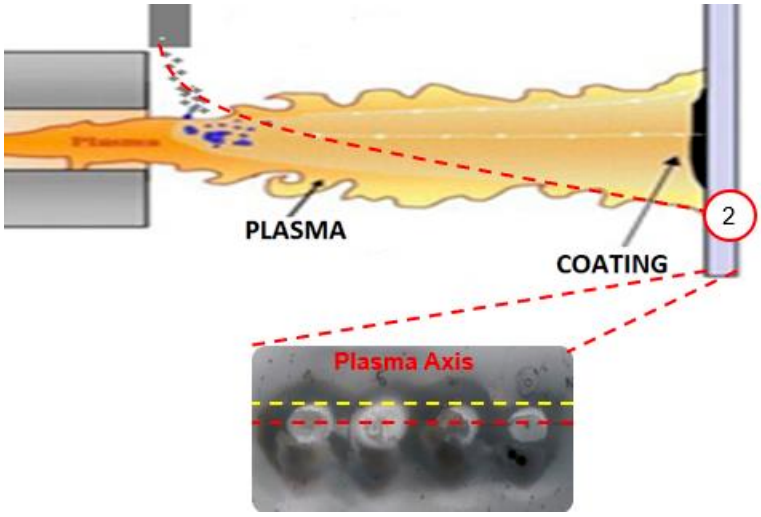

Figure 24. Trajectories of BHAp in-flight particles injected to the plasma at 10 mm using Ar carrier gas at 5NL/min and 5 bar.

Figure 24 presents a schematic representation of the trajectories of BHAp particles injected at 10 mm of the plasma nozzle using Ar carrier gas at 5NL/min and 5 bar. The trajectory was proposed considering the difference in the axis of the BHAp deposits compared to the plasma nozzle axis. It is assumed that either the distance between the powder injector and plasma nozzle was low and carrier gas flow and pressure were too high, hence, the efficiency of the deposition was low. Deposits of BHAp were studied by varying the pressure and distance between the injector and plasma nozzle. These deposits are seen in Figure 25. Figure 25a shows the BHAp

deposited at initial conditions: translation and rotation of the sample holder (2.4 cm/s, 124 RPM) and powder injected at 10 mm at 5 bar. Afterward, Figure 25b shows BHAp deposited with the same initial conditions and the substrate at a fixed position. This deposit was repeated with substrate translation at 2.4 cm/s and presented in Figure 25c. Similarly, Figure 25d presents the deposit after reducing the carrier gas pressure to 3 bar. Moreover, the injection distance was reduced and the deposit is seen in Figure 25e.

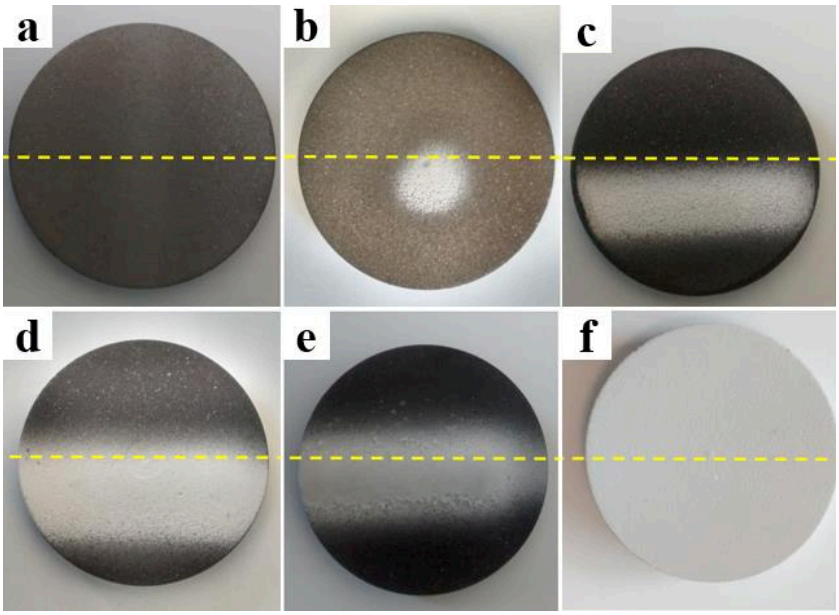

Figure 25. Deposits of BHAp sprayed using different powder injection distances, carrier gas pressure and sample holder translation and rotation and translation: a) 10 mm, 5 bar, 2.4 cm/s and 124 RPM, b) 10 mm, 5 bar, stationary conditions, c) 10 mm, 5 bar, 2.4 cm/s and no rotation, d) 10 mm, 3 bar, (2.4 cm/s) and no rotation, e) 7 mm, 3 bar, 2.4 cm/s and no rotation, and f) 7 mm, 3 bar, 2.4 cm/s and 124 RPM.

Finally, the surface of the substrate was fully coated by projecting BHAp at 7mm of injection and carrier gas pressure of 3 bar. The powder was not deposited by using the initial conditions which indicate either that the powder was not entering within the plasma or it was passing through the plasma. Protecting the BHAp in translation conditions as is showed in Figure 25b and Figure 25c supports the hypothesis that powder was passing through the plasma, then the deposit was under the axis of the gun. Ar carrier gas was decreased 2 bar and the deposition efficiency was increased as is seen in Figure 25b due to the higher interaction of powder with the plasma. As particles are more condensed among them at closer distances from powder injector, the interaction of particles with plasma is more efficient. For this reason, the injector was placed 2 mm closer to the plasma and the efficiency of the deposition was increased as is seen in Figure 25b. A coating was deposited under the same plasma conditions compared to the coating deposited in Figure 25c to test this hypothesis. Consequently, the powder feeding

conditions at 7 mm of injection distance and 3 bar allows increasing the deposit efficiency and the coating was obtained under the rotation and translation of the substrate. BG powder feeding parameters are the same considering the similar size, morphology, and density compared to BHAp.

2.1.2. HVOF and APS BHAp coatings morphology and microstructure characterization by scanning electron microscopy (SEM)

Cross-section and surface SEM micrographs of BHAp coatings projected by APS and HVOF are presented in Figure 26. The thickness of the APS coating was in the range of 56.61 ± 11.88 µm (see Figure 26a). Moreover, macro and micropores are present all along the cross-section of the APS coating and a rough surface profile is also noted. On the other hand, the cross-section of the HVOF coating shows a dense microstructure with a thickness in the range of 74.98 ± 4.67µm (see Figure 26b). The surface roughness is lower than the APS coating and the presence of fewer micropores and cracks is also observed. Pores and higher roughness of APS coatings are related to the heterogeneous in-flight particle state, gas-filled voids and the low velocity of the APS process [48].

Despite the high temperature of plasma, the radial powder feeding in the deposition leads to a heterogeneous interaction between BHAp particles and the plasma. Consequently, a mixture of molten, semi-molten and non-molten particles is seen in the surface, in which the low impacting velocity of subsequent particles over previous cooled down deposits prevents the particle packaging and in consequence, a disordered splat overlapping. In contrast to APS coatings, the high velocity of projected BHAp under HVOF conditions allows obtaining a dense coating, where deposits were well packed and compressed among them. Non-molten particles are not observed on the surface, which agrees with the dense microstructure presented in the coating cross-section.

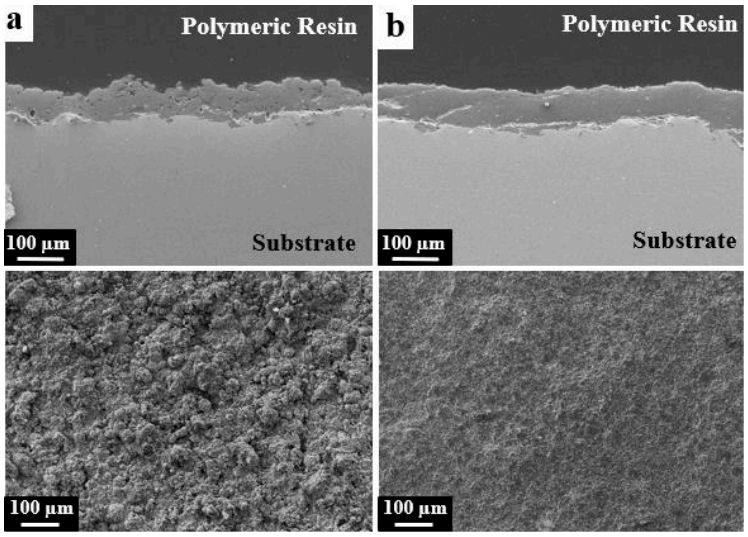

Figure 26. Cross-section and surface SEM micrographs of a) BHAp APS coating and b) BHAp HVOF coating.

The interaction between the BHAp in-flight particles and the plume was more effective than in APS considering the used axial feeding of powders. Hence, a homogeneous surface is seeing in comparison to the BHAp APS coating. A Similar morphology description for HAp APS and HVOF coatings is reported elsewhere [49].

2.1.3. HVOF and APS BHAp coatings structural characterization by grazing incident angle x-ray diffraction (GIXRD)

The structural characterization of BHAp APS and HVOF coatings is presented in Figure 27. The crystallographic card JCPDF 9-432 that corresponds to $Ca_5(PO4)_3(OH)$ phase was used to identify the apatite crystalline phase. The analyzed diffractograms were normalized based on the intensity of the peak corresponding to plane 211 at 32.5 º 2θ. HAp phase presents its main peak at 31.82 ° 2θ and is the major phase content in both coatings. In addition, a secondary phase was observed on the HVOF coating diffractogram evidenced by the peak presence at 31.28 ° of 2θ, which reveals the phase formation of dolomite ($CaMg(CO_3)_2$) identified with the ICSD 10404 card. Table 7 summarizes the phase content and the calculated structural parameters of the HAp phase obtained from the Rietveld analysis for both coatings.

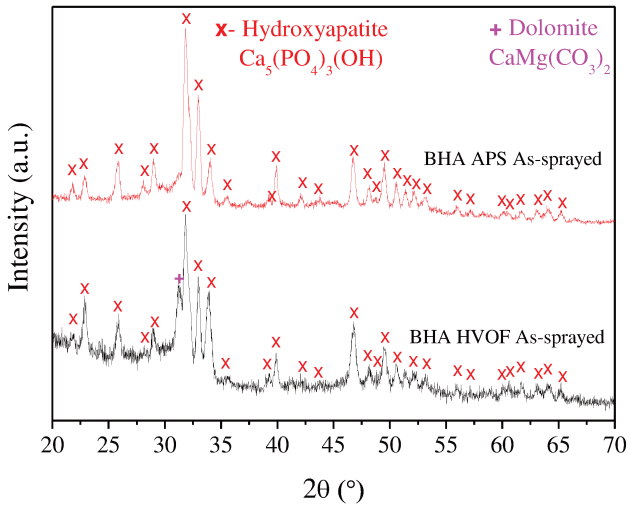

Figure 27. XRD patterns of As-sprayed BHAp HVOF and APS coatings

The obtained results can be compared to magnesium-containing apatites with similar lattice parameters. For instance, *a* and *c* in the unit cell of APS coating were similar to the structural distances in apatites with 0.21 % Mg^{2+} and 7.3 % CO_3^{2-}. Regarding HVOF coatings, lattice parameters were similar to apatites with 1.47 % Mg^{2+} and 7.7 % CO_3^{2-} [19]. This comparison shows that HVOF coatings contain major Mg^{2+} →Ca^{2+} (II) and CO_3^{2-} → PO_4^{3-} substitutions and that the deposition conditions promote the carbonization of the BHAp

Table 7. Structural parameters of the HAp phase on BHAp feedstock powder, BHAp APS and BHAp HVOF coatings obtained by Rietveld analysis.

	Hydroxyapatite						
	Phase %	a (Å)	c (Å)	Ca/P	Crystallite size (Å)	Cell Volume ($Å^3$)	χ^2
BHAp APS	100	9.408	6.902	1.48	266.26	529.16	2.56
BHAp HVOF	51.25	9.393	6.887	1.42	203.29	526.4	1.62

Higher carbonization of HVOF coatings is expected considering the interaction of the bioceramic with a major concentration of carbon dioxide due to the propane combustion (see equation 3).

$$C_3H_8 + 5O_2 \rightarrow 3CO_2 + 4H_2O \quad (3)$$

Therefore, the dolomite formation on the coating surface structure is promoted by two reasons: the carbonization of the BHAp deposited by the HVOF process and the available Mg^{2+} from bovine-derived hydroxyapatite in the feedstock powder. This phase is formed with Ca from BHAp leading to a *Ca/P ratio* reduction in the HAp crystalline phase. Commercial stoichiometric HAp coatings deposited under the same HVOF parameters did not show any secondary phases within its structure [50]. Thus, it can be concluded that BHAp is more unstable compared to commercial HAp, which is expected given the substitutions and vacancies on the feedstock powder structure. The dolomite phase percentage and its structural information are shown in Table 8.

Table 8. Structural information of the dolomite phase on BHAp HVOF coating obtained by Rietveld analysis

	Dolomite				
	Phase %	a (Å)	c (Å)	Cell Volume ($Å^3$)	χ^2
BHAp HVOF	48.75	4.801777	16.012957	319.747	1.62

The number of Ca atoms per formula unit (nCa) of the dolomite structure was calculated following the model proposed by Nascimento dos Santos *et al.* (see equations 4 and 5) [51], where *a* and *c* are the obtained lattice parameters in the Rietveld analysis.

$$a = 4.6904 + 0.1168\ nCa \tag{4}$$

$$c = 15.138 + 0.8646\ nCa \tag{5}$$

From equations 4 and 5, the number of Ca atoms in the dolomite phase (nCa) is 0.953 and 1.0123, respectively. Hence, the phase should be considered stoichiometric and the calculated lattice parameters agree with the reported crystallographic information for this phase [52]. Although the feedstock powder is considered carbonated and the Mg^{2+} is present in the crystals structure and surface, the dolomite phase was not identified in the APS coating. In this technique, the plasma was generated by employing Ar and H_2 and there was not a source of dioxide carbon in the spray process different than air. Hence, the hypothesis here proposed should be valid and the formation of the dolomite in HVOF coating was possible under two subsequent conditions: 1) Carbonization of the feedstock powder because of its interaction with the propane combustion plume and 2) Presence of Mg^{2+} in the BHAp either as a substitution or in the surface of the crystal.

2.1.4. HVOF and APS BHAp coatings bioactivity analysis after immersion in simulated body fluid (SBF)

Scanning electron microscopy (SEM) surface micrographs

APS coating morphology after immersion in SBF during 0, 3, 5 and 10 days is showed in Figure 28. In Figure 28a the micrographs of as-sprayed coating show melted, overlapped and impacted particles with an irregular flattening shape. Microcracks and small pores with a diameter less than 100 nm are also seen. The surface modification due to the growth of a bone-like apatite layer is clearly observed after 3 days of immersion in SBF (see Figure 28b). The apatite layer microstructure comprises of small nanocrystals is similar to the microstructures described as a globular flake-like [53–55]. However, the polyhedral grain microstructure typically from Ca-deficient apatites [56] better describes the morphology of the growth layer seen in the figures. The polyhedral grain layer covers all the coating surface with preferential growth in the splats edges, cracks, and pores. Finally, Figure 28c and Figure 28d show the polyhedral grain layer with bigger crystals after 5 and 10 days of immersion.

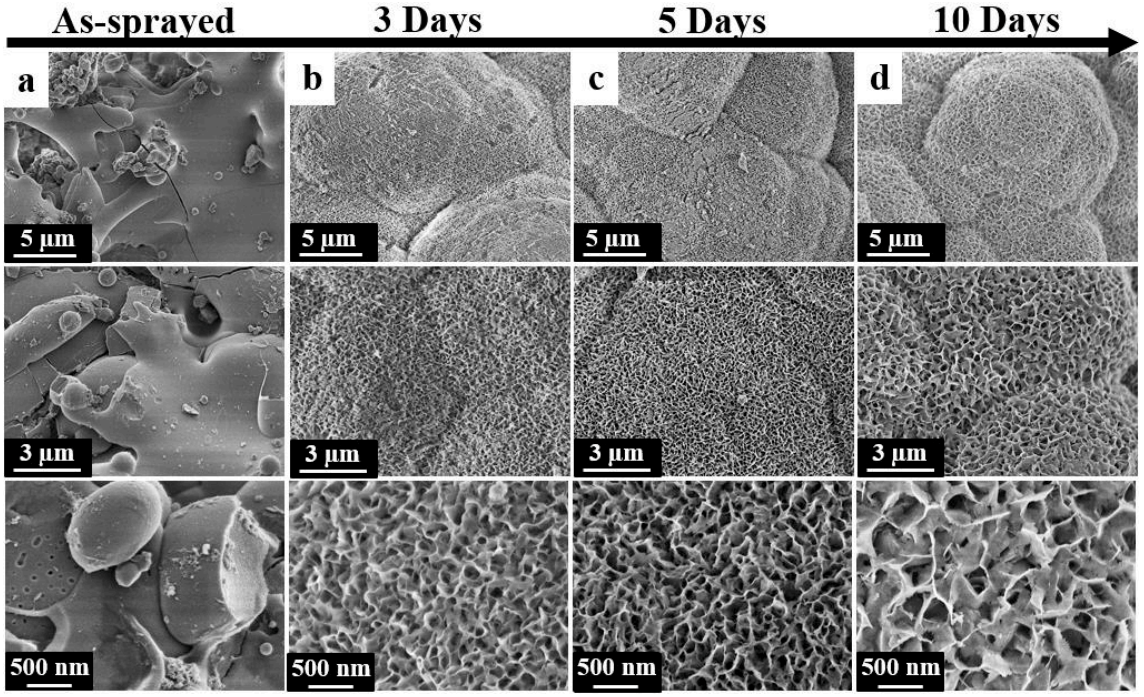

Figure 28. Apatite formation on the BHAp APS coating surface monitored by SEM after immersion in SBF at a) 0, b) 3, c) 5 and d) 10 days. Each surface is shown at three magnifications: 5000 x, 10000 x, and 35000 x.

Microcracks and small pores in the as-sprayed coating are caused by residual stresses and entrapped air in the coating build-up [57,58]. On the other hand, splat edges pores and cracks are known as nucleation sites for Ca precipitation after immersion in SBF, which explains the

preferential sites for apatite growth [59]. After this precipitation, particles of calcium compounds work as nucleators in the formation of calcium phosphates nuclei. Later, the layering of the ions interchange with the simulated fluid leads to two-dimensional crystal growth. This polynuclei-like phenomenon occurs rapidly on carbonate-apatite coatings as BHAp [60,61]. The surface morphology after 3 days of immersion is similar to the morphology of Ca- deficient apatites and immersed HAp coatings after either 7 days or several weeks presented in previous reports [62–64]. Therefore, the bioactivity rate of the BHAp APS coating is higher than those from commercial stochiometric HAp deposited by plasma spray.

Figure 29 shows the SEM micrographs of BHAp HVOF surface coating after immersion in SBF at 3, 5 and 10 days. Micrographs of the as-sprayed coating surface were also added. As-sprayed coating surface present disk-like shape splats as well as small spherical semi-molten particles (~1µm) (see Figure 29a,). After 3 days of immersion, the polyhedral grain apatite layer covers the coating surface and a spherulite of 6 µm is noticed. Furthermore, microcracks are also observed and the growth of the nanocrystals is more evident at higher magnifications (see Figure 29b). Figure 29c. shows a smoother coating surface with numerous microcracks compared to the surface in the coating after 3 days of immersion. The apatite layer is less evident than it is in Figure 29b, and the polyhedral grain apatite morphology is nearly observed in the area between the splats edges. Splats partially covered by the apatite layer are also seen at 10000 x. This apatite morphology has smaller crystals compared to those presented in Figure 29b. At 10 days of immersion (See Figure 29d), the coating surface has similar microcracks to those shown in Figure 29c. Nevertheless, the apatite layer has a morphology similar to the coating surface after 3 days of immersion.

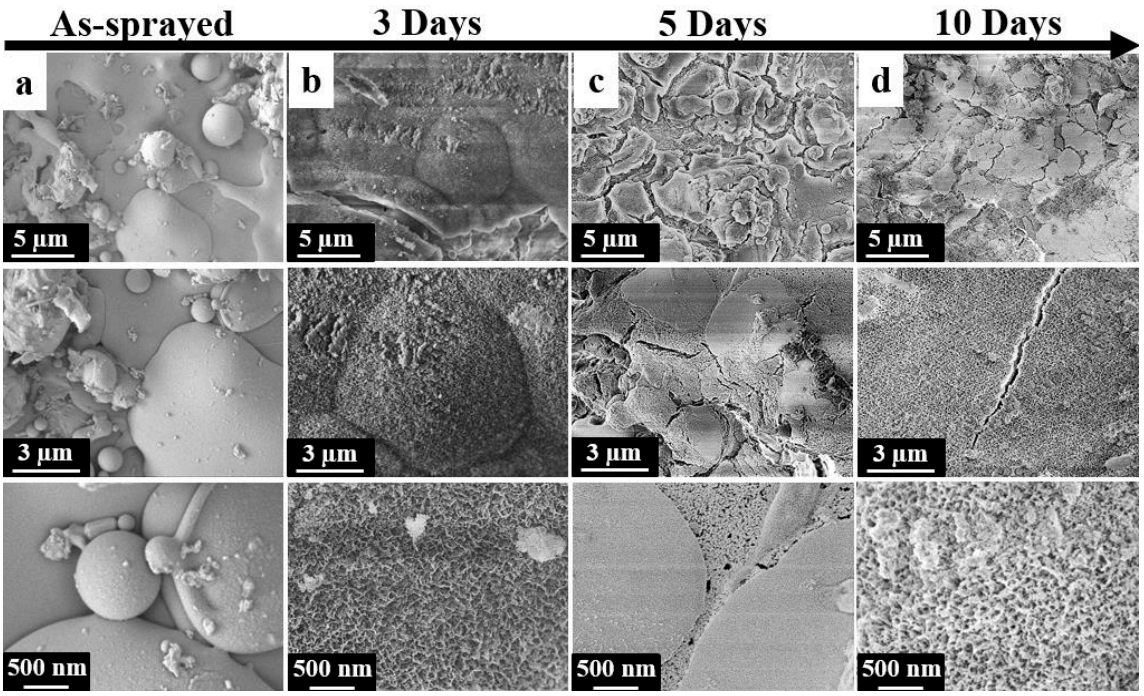

Figure 29. Apatite formation on the BHAp HVOF coating surface monitored by SEM after immersion in SBF at a) 0, b) 3, c) 5 and d) 10 days. Each surface is shown at three magnifications: 5000 x, 10000 x, and 35000 x.

The combination of the in-flight particle temperature and high velocity promotes the formation of disk-like splats in the coating build-up. After 3 days of immersion in SBF, the apatite growth occurs as expected. Microcracks formation is a consequence of the coating reaction and partial ion diffusion with the simulated fluid [61]. Delamination of the new apatite layer in the coating after 5 days of immersion is attributed to the presence of dolomite as a secondary phase. It is well known that delamination after immersion in HAp ($Ca_5(PO_4)_3(OH)$) bioactivity analysis is caused by the presence of secondary phases such as $Ca_3(PO_4)_2$ (β-TCP) within its structure [65]. Similarly to β-TCP in decomposed HA, dolomite ($CaMg(CO_3)_2$) is a secondary phase of the BHAp ($Ca_{10-x}(PO4)_{6-x}(CO_3)_x(OH)_{2-x}.Mg$) crystallized after the deposition by HVOF. On the other hand, the high bioactivity of the BHAp leads to the rapid formation of a new polyhedral grain layer evidenced after 10 days of immersion. The present contribution shows that dolomite phase formation is detrimental for coating stability and its influence on the mechanical properties of the BHAp HVOF coating must be further analyzed.

Micrographs of coatings surface after 5 days of immersion with lower magnifications are presented in Figure 30 to give a complementary description of the surface bioactivity. Figure 30a presents the APS coating surface at 100 x and 800 x. A dune-like layer surface with a globular morphology, spherulites of different sizes and characteristic microcracks cover most of the coating area. Figure 30b shows similar micrographs for HVOF coating. The growth

apatite layer covers a wide area of the surface with spherulites of ~ 15 um in diameter. However, the micrographs show interlayer coating delamination characterized by a multilayer surface with apatite deposited in layers at different heights and small areas without the characteristic apatite morphology.

The globular dune-like morphology in APS coating is similar to that one from the layer that grows on commercial HAp deposited by APS after higher immersion times (i.e. 14, 28 days) [64,66,67]. Thus, BHAp coatings deposited by APS compared to conventional HAp coatings present a higher bioactivity rate and agree with the previous SEM analysis at higher magnifications (see Figure 28). Despite the presence of the dolomite phase in HVOF coating, the surface also shows the globular dune-like morphology of the apatite layer after 5 days of immersion in SBF, which represents the high bioactivity of the coating. This morphology is seen in conventional HAp HVOF coatings after 7 to 14 days of immersion in the simulated fluid [68,69] and even after 28 days in HAp coatings sprayed under the same parameters [50].

The rapid apatite formation on the coating surface is not surprising given that dolomite is a direct depositor of minerals as Ca^{2+} and Mg^{2+} and in biological media, this ceramic plays a supporting role in the formation of new mineral complexes leading to hard tissue remineralization [70]. The multilayer surface morphology of HVOF coating demonstrates that the delamination of the coating was induced by the apatite growth between the sprayed layers. This delamination is unambiguously related to the formation and dissolution of the dolomite phase in the interlayers of the coating. The dissolution is followed by the apatite formation after the sedimentation of ions from the simulated fluid and the dissolved dolomite. Hence, the appearance of the globular dune-like surface at different layers and the coating rapid apatite formation after delamination is explained.

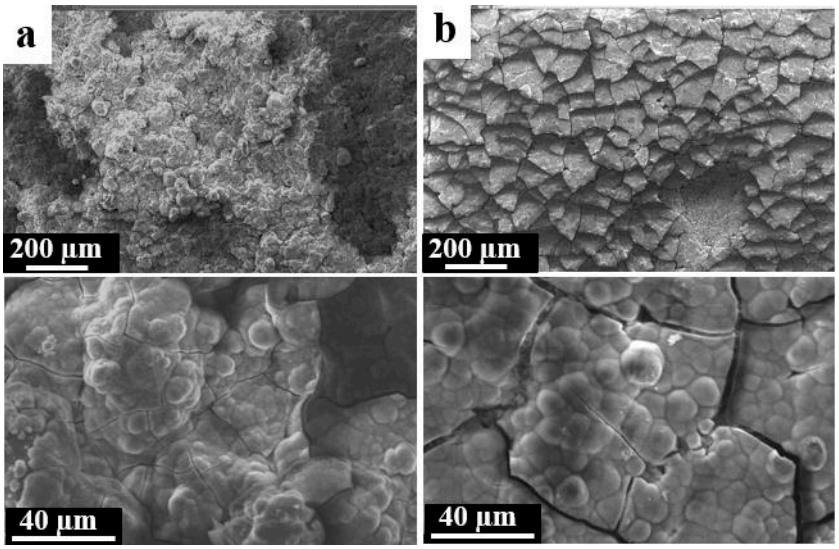

Figure 30. Apatite formation on the BHAp coatings surface monitored by SEM after 5 days of immersion in SBF at 100 x and 800 deposited by a) APS and b) HVOF.

Grazing incident angle x-ray diffraction (GIXRD) and Rietveld analysis

X-ray diffractograms of the APS and HVOF coatings after 3, 5 and 10 days of immersion in SBF are showed in Figure 31. The mean width of the peaks is increased in the diffractogram of the APS coating after 3 days of immersion (see Figure 31a). The increase of the 002 peak intensity at 26° 2θ is also seen and similar diffractograms are obtained for the measurements of coating immersed at 5 and 10 days. On the other hand, the diffractograms of BHAp HVOF coating after the same days of immersion are presented in Figure 31b. The surface XRD pattern after 3 days is similar to the structure of the BHAp APS coating surface at the same days of exposition to the simulated fluid. Nevertheless, the mean width of the peaks is decreased after 5 and 10 days of immersion. In addition, a peak around 31.1° 2θ is again observed compared to the as-sprayed HVOF XRD pattern.

The peaks broadening of the diffractograms evidences the growth of the apatite layer on the surface of both coatings. Furthermore, the apatite growth preferential orientation in the 002 direction confirms the crystal orientation of natural apatite in the animal's hard tissues [66]. The APS coatings diffractograms show the apatite structure after 3 days of immersion in SBF and the growth of this layer continues after 5 and 10 days of immersion. This in agreement with the description of the micrographs in the surface morphology analysis where the apatite growth layer was progressive during all the bioactivity test (see Figure 28and Figure 29).

On the other hand, the apatite layer growth in HVOF coating is seen after 3 days of immersion in SBF. However, the reduction of the mean width of the peaks after 5 days and the intense

peak at 31.1° 2θ after 10 days of immersion probes that the apatite growth is followed by the coating interlayer delamination. In fact, the XRD pattern after 10 days in SBF is similar to the diffractogram of the as-sprayed HVOF coating. Consequently, the dissolution of the dolomite phase followed by the apatite growth and coating interlayer delamination is again confirmed.

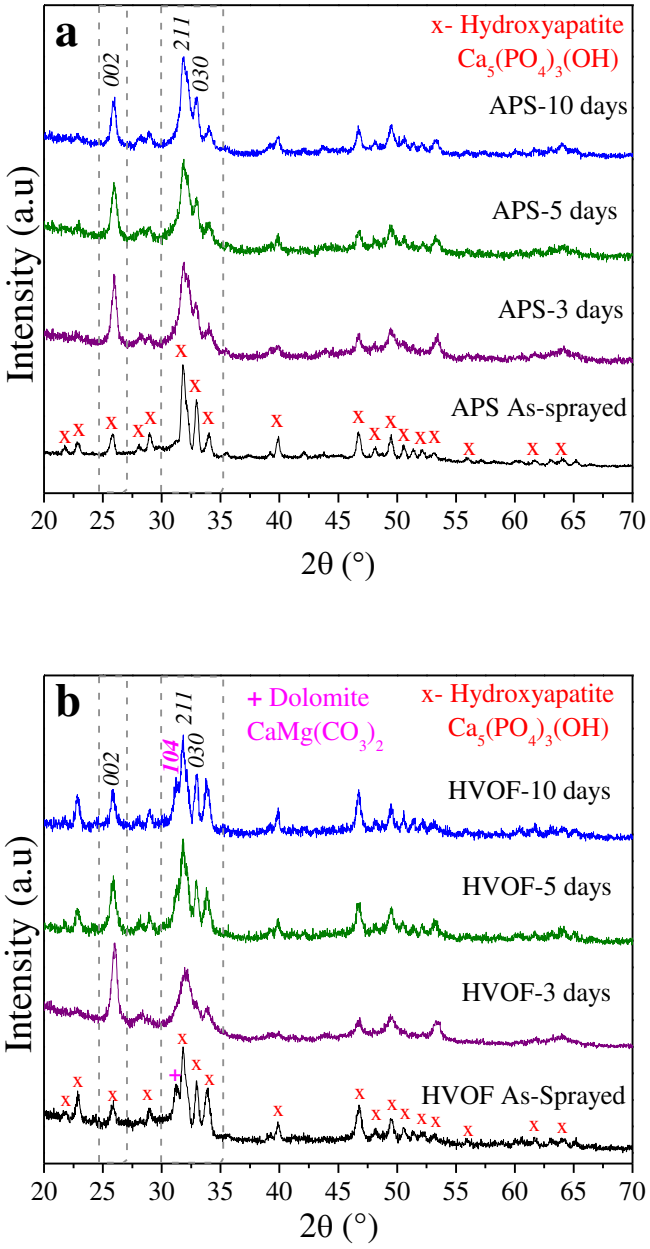

Figure 31. Structural characterization of BHAp coatings after 0, 3, 5 and 10 days of immersion in SBF deposited by a) APS b) HVOF.

Figure 32 shows the calculated *Ca/P ratio* of coatings surface by Rietveld analysis as a function of immersion time. The initial *Ca/P ratio* of APS coating of 1.49 increased up to 1.85 between

0 and 3 days of immersion, decreased to 1.55 after 5 days and then increased again to 1.64 after 10 days. This final *Ca/P* value matches with the *Ca/P ratio* of the feedstock powder. Additionally, the initial *Ca/P ratio* of 1.42 in HVOF coating is increased to 1.53 after 3 days and after decreased to 1.24 and 1.09 after 5 and 10 days of immersion, respectively.

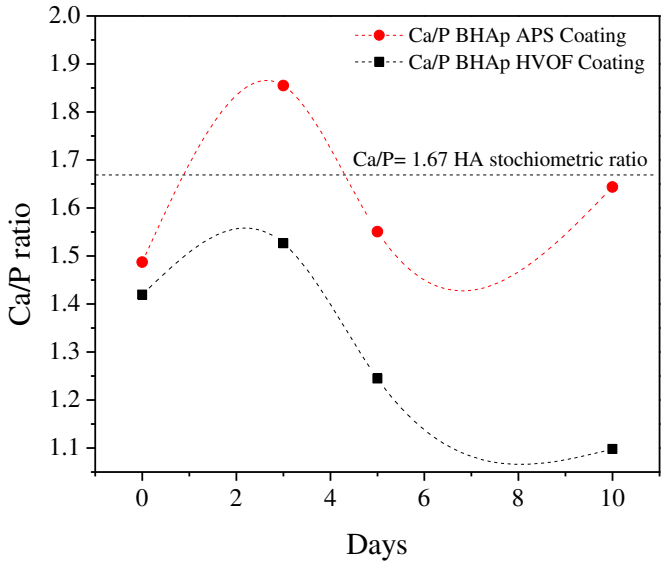

Figure 32. Ca/P ratio after 0, 3, 5 and 10 days of immersion in SBF of BHAp coatings deposited by APS and HVOF.

The first increment value of Ca/P in APS is due to the formation of a Ca-rich layer as a consequence of the interaction of the BHAp surface with Ca^{2+} from the SBF. Thereafter, the value of Ca/P after 5 days of immersion decreased by the interaction of the Ca-rich layer with phosphate ions from SBF resulting in a Ca-poor layer deposition. Finally, after 10 days of immersion, the growth of the apatite layer incorporates Ca^{2+} and PO_4^{3-} ions simultaneously resulting in a greater *Ca/P ratio* compared to the coating Ca-poor layer after 5 days of immersion. Similarly, the increment of the *Ca/P ratio* in the HVOF coating after 3 days shows the Ca-rich layer deposition. Nevertheless, the Ca-rich layer interaction with PO_4^{3-} form SBF and the subsequent coating delamination decreased the *Ca/P ratio* after 5 days of immersion. The decreasing rate of the *Ca/P ratio* is reduced because of the initial stages of growth of a new apatite layer after 10 days of immersion which is also seen in SEM micrographs (see Figure 29).

Elements concentration measurements in SBF by ICP after coatings immersion

The concentration of *Ca*, *P* and *Mg* in SBF during the bioactivity analysis is presented in Figure 33. Figure 33a and Figure 33b. show that the *Ca* and *P* concentrations follow a decreasing pattern in the SBF of both coatings. The *Ca* concentration was higher in the HVOF SBF during all the immersion times. The total *Ca* concentration was reduced by 20 % and 22.5 % in the HVOF SBF and APS SBF, respectively. *P* concentration was also higher in HVOF SBF during all the immersion times. Additionally, the total *P* concentration was reduced by 30.7 % and 51.9 % in the HVOF SBF and APS SBF, respectively. *Mg* concentration evolution has opposite patterns in APS SBF compared to the concentration HVOF SBF (see Figure 33c.). *Mg* concentration decreases 23.8 % from 0 to 3 days of immersion in HVOF SBF and it does not undergo significant concentration changes after 5 and 10 days. On the contrary, Mg concentration in APS SBF is almost constant until 5 days of immersion. Thereafter, the concentration decreases by 25.9 % from 5 to 10 days of immersion.

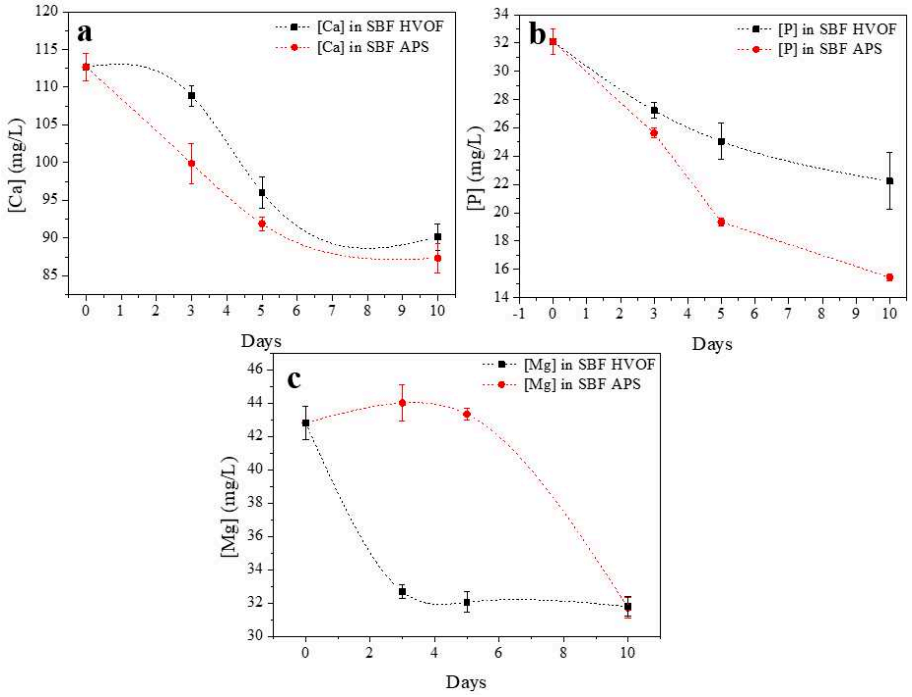

Figure 33. Elements concentration in SBF after 3, 5 and 10 days of coatings immersion: a) Ca, b) P and c) Mg.

The uptake of *Ca* and *P* from SBF to the coating is due to the expected bioactivity kinetics in the apatite layer growth for both coatings. The higher uptake of *Ca* and *P* in APS coatings shows that the apatite formation kinetics was faster on this coating compared to HVOF coating. Additionally, the decreased *Mg* content in the HAp structure of HVOF as-sprayed coating due to the formation of the dolomite phase promotes vacancies and increases the *Mg* uptake from

SBF to the coating in the firsts days of immersion. Consequently, the rapidly *Mg* uptake leads to growth inhibition of new apatite on the surface [59,71], which also explains the smaller polyhedral crystals on the coating SEM micrographs after immersion compared to APS coating. It is well known that this inhibition activity is related to the competition of Ca^{2+} and Mg^{2+} for Ca sites or vacancies and the Mg^{2+} adsorption on the apatite surface growth sites [72,73]. On the other hand, a crystalline phase containing Mg was not formed in APS coating. In consequence, the *Mg* uptake from SBF to this coating was noticed after 5 days of immersion. The incorporation of this ion is expected to start at 5 days of immersion in bioactivity tests during the formation of the apatite layer [74] agreeing with the results here presented.

2.2.BHAp APS COATINGS ANALYSIS

2.2.1. BHAp APS coatings morphology and microstructure characterization by scanning electron microscopy (SEM).

Micrographs in Figure 34 and Figure 35 shows the cross-sections of coatings deposited under the parameters combinations presented in Figure 8. Similar thicknesses are observed in BHAp coatings deposited at 7 g/min of PFR with values of 58.2 ± 5.5 µm (Figure 34a), 54.9 ± 5.7 µm (Figure 34b) 57.5 ± 5.7 µm (Figure 34c) and 59.9 ± 9.4 µm (Figure 34d). Moreover, the roughness of this set of coatings is also similar among them having Ra values of 6.4 ± 1.1 µm, 5.6 ± 0.5 µm, 6.9 ± 0.4 µm, and 6.3 ± 1.1 seen in Figure 34a, Figure 34b, Figure 34c, and Figure 34d, respectively. On the contrary, the microstructure of coatings deposited using a current of 750 A is denser than coatings deposited using plasma generated with a current of 450 A.

Similar characteristics are seen in the micrographs of coatings deposited at PFR = 10 g/min, where deposits fabricated using 750 A in the plasma generation also shows a denser microstructure. The roughness of this set of coatings was also statistically similar presenting Ra values of 6.3 ± 0.1 µm, 6.6 ± 1.2 µm, 5.3 ± 0.6 5.3 ± 0.3. Regarding the thickness, coatings present values of 65.2 ± 5.9 µm, 39.7 ± 4.7 µm, 98.9 ± 8.0 µm and 61.8 ± 5.5 as is seen in Figure 35a, Figure 35b, Figure 35c, and Figure 35d, respectively. Based on micrographs in Figure 34 is possible to conclude that the studied range of SOD has no influence on the thickness and roughness of the coatings. This, considering that the difference of residence time of in-flight particles in plasma within this range does not have a considerable effect on the particle's physical state. Consequently, particles are packed similarly in the build-up of all the studied coating. On the other hand, the studied range of plasma current from 450 to 750 A, demonstrates to have a considerable effect on the microstructure of the coatings. Thus, the high melting state

of particles due to the higher enthalpy of plasma leads to a more effective overlapping of deposited particles. Therefore, cross-sections of coatings deposited at 750 A shows a denser microstructure. This difference is also noticed on coatings deposited using a PFR = 10 g/min where the microstructure of coatings at higher current and plasma enthalpy shows a denser microstructure.

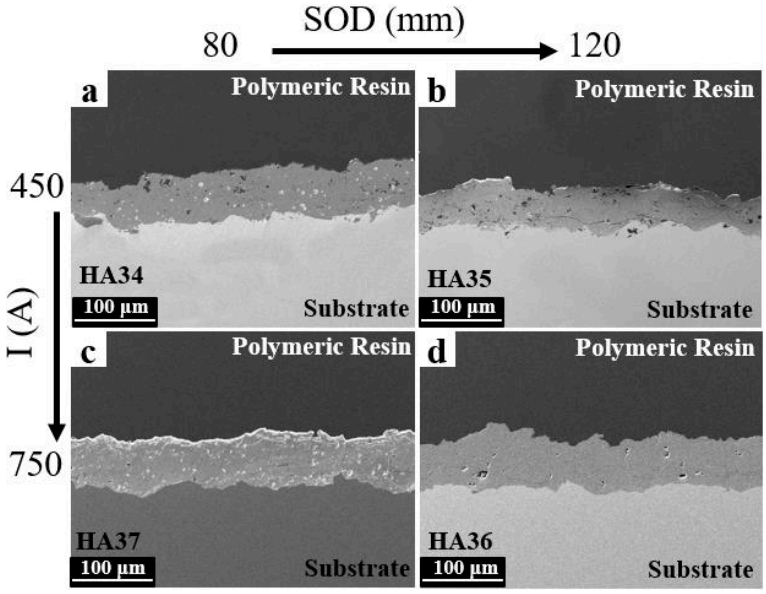

Figure 34. Cross-section micrographs of BHAp coatings sprayed by APS at 7 g/ min of PFR and values of I and SOD of a) 450 A and 80 mm, b) 450 A and 120 mm, c) 750 A and 80 mm, and d) 750 A and 120 mm.

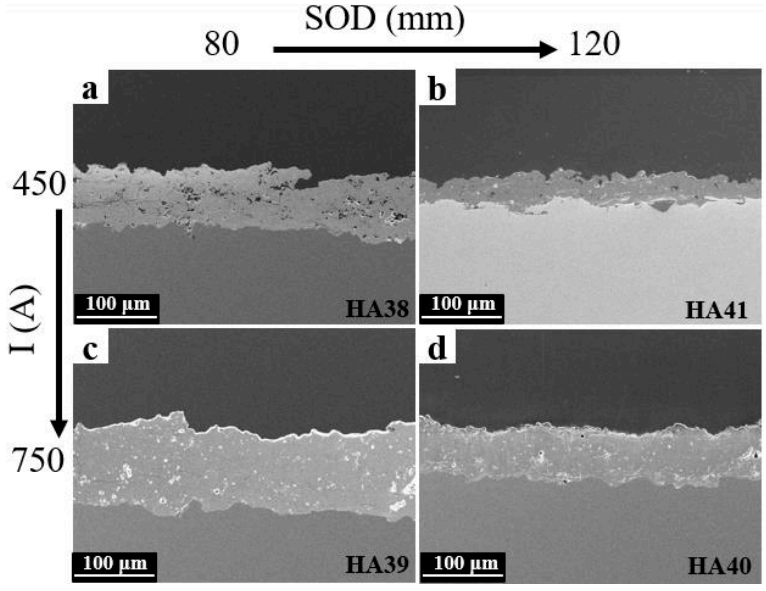

Figure 35. Cross-section micrographs of BHAp coatings sprayed by APS at 10 g/ min of PFR and values of I and SOD of a) 450 A and 80 mm, b) 450 A and 120 mm, c) 750 A and 80 mm, and d) 750 A and 120 mm.

The increment of PFR leads to obtain thicker coatings. However, the coating presented in Figure 35b shows a reduced thickness. Since coatings were sprayed during the same session, available powder in powder feeder was decreased from coating to coating before obtaining the last sample named HA41. Therefore, the powder feeder control was affected by the reduction of available powder decreasing the deposition efficiency on the coating deposition (see Figure 35b). Besides this, no significant differences were founded in deposits sprayed at PFR = 10 g/m. Hence, the coating microstructure and surface roughness were no affected by the PFR studied range. It is known that dense HAp coatings reduce the cell ingrowth in coatings [75], thus, samples obtained at 450 A represent coatings with higher biocompatibility. In addition, the studied parameters lead to the deposition of APS coatings with proper thicknesses and roughnesses to allow a good cell attachment, proliferation and fatigue behavior in comparison with the results from previous biocompatibility and mechanical studies of HAp deposited by APS [76,77].

2.2.2. BHAp APS coatings structural characterization by x-ray diffraction (XRD) and Rietveld analysis

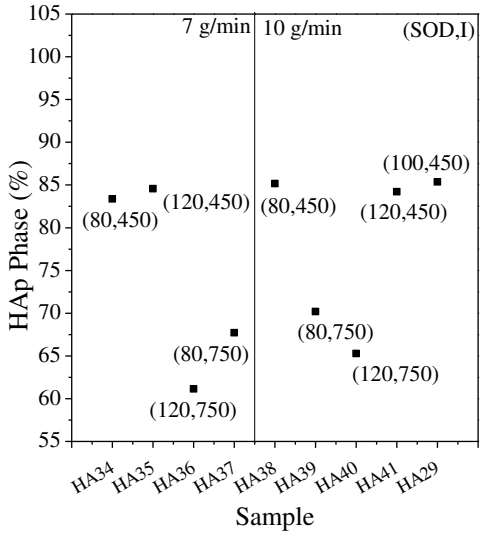

Figure 36. Quantification of HAp crystalline phase in BHAp APS coatings structure

The HAp crystalline phase quantification of APS coatings is shown in Figure 36. The phase quantification from XRD and Rietveld analysis of the APS coating obtained at PFR = 10 g/min SOD = 100 mm and Current = 450 A (HA29) is also presented. Moreover, the values of SOD and current are added below each obtained value from the analysis. The HAp phase content was similar in all the coatings sprayed by using 450 A for the plasma generation (83.7 to 85.3 wt. %). The HAp phase in coatings sprayed at 750 A was in the range of 61.1 and 70.1 wt. %, being

lower in coatings deposited at 120 mm. As expected, high plasma current leads to a higher decomposition of HAp in secondary phases. This decomposition is increased at lower PFR and higher SOD values, as a consequence of the incremented residence of time of particles in the plasma and the reduced in-flight mass to transfer the plasma energy during the deposition. This is similar in coatings plasma-sprayed at 450 A. Despite the high HAp phase content within the structure of these coatings, the HAp percentage was higher in samples sprayed at shorter distances and PFR of 10 g/min. Among these deposits, conditions HA38 and HA29 shows the maximum HAp content with a difference of 0.19 wt. %. Summarizing, coatings with higher HAp phase content were those sprayed at PFR = 10 g/m, Current= 450 A and SOD either 80 or 100 mm. The APS process and the set of parameters PFR = 10 g/m, I = 450 A and SOD = 100 mm (HA29), were chosen to fabricate the bioactive glass (BG45S5 and BG45S5+10Bi_2O_3) and gradual BHAp/BG45S5+10Bi_2O_3 coatings. This, taking into account that BHAp decomposition is higher under the fabrication of coatings by HVOF, the previous results and the bioactivity analysis of APS coating deposited by using the set of parameters of used in the fabrication of HA29 sample.

2.3.COMMERCIAL AND LAB-MADE BG45S5 COATINGS OBTAINED BY APS

2.3.1. Commercial BG45S5 and lab-made BG45S5 + 10 wt. % Bi_2O_3 APS coatings morphology and microstructure characterization by scanning electron microscopy (SEM).

The micrographs showing the cross-section and surface of commercial and lab-made BG45S5 + 10 wt. % Bi_2O_3 (BG45S5+10Bi_2O_3) fabricated under the set of parameters chosen in the previous section are seen in Figure 37. The cross-section of commercial BG45S5 coating presents a thickness of 105.5 ± 1.5 µm (see Figure 37b).

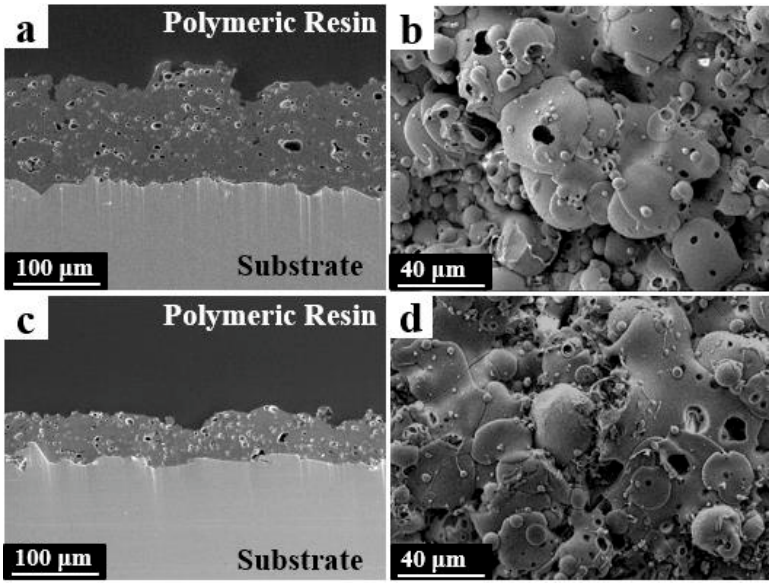

Figure 37. SEM micrographs of APS BG45S5 coatings: a), b) Commercial cross-section and surface and c), d) lab-made cross-section and surface.

Well overlapped splats are seen with sizes between 5 µm and 40 µm in diameter in the surface micrographs (Figure 37b). Additionally. Fully melted particles are also observed along with particles of 5 µm attached to the splats. On the other hand, the BG45S5+10Bi_2O_3 cross-section micrograph (see Figure 37c) presents a coating with a thickness of 45.5 ±5.2 µm. Furthermore, a mixture of splats and fully melted particles are also seen on the surface of this coating (see Figure 37d). Macropores are noticed in al the micrographs either cross-section or surface images. The surface and cross-section microstructure of both coatings was similar. This is not surprising given the similar thermal properties of both feedstock powders (see Figure 19). Differences in coating thicknesses may be attributed to the powder feed rate lack of control or powder injector clogging during spraying. However, thick coatings were obtained and splats flattening and overlapping show proper combination of APS parameters. The size of these splats agreeing with the particle size distribution of both feedstock powders (see Figure 13 and Figure 22). However, the macropore's presence in all the micrographs, possibly by the P_2O_5 evaporation, indicates that the plasma conditions, coating exposition to the plasma and cooling rate of the coating were such that induces the evaporation and entrapment of sublimed oxides from the glass leading to the formation of the pores [78]. It is well known that this type of porosity increases its biocompatibility and reduces its mechanical properties [79]. Nevertheless, the gradual configuration of thermally sprayed BHAp with BG45S5 could represent an advantage to reduce the porosity of the single coating.

2.3.2. Commercial BG45S5 and lab-made BG45S5+10Bi_2O_3 APS coatings structural characterization by x-ray diffraction (XRD)

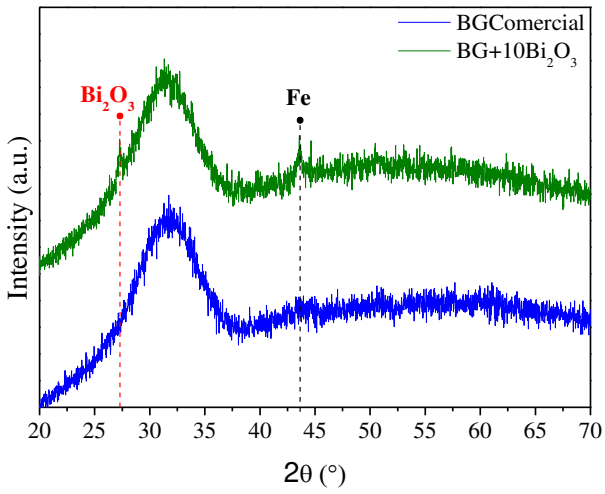

Figure 38. Structural characterization by XRD of commercial BG45S5 and lab-made BG45S5+10Bi_2O_3 APS coatings by XRD.

The structure of the coatings studied in the previous section was investigated by XRD analysis and their diffractograms are shown in Figure 38. Both diffractograms present a diffraction band between 25 and 35 °2θ. However, two diffraction peaks at ~ 27.2 and ~ 43.6 °2θ of with low intensities are observed in the XRD pattern of BG45S5+10Bi_2O_3 which are not seen in the diffractogram of the commercial BG45S5 coating. Both diffraction patterns follow the typical XRD diffractograms of amorphous silicate glasses characterized by the diffraction band centered at ~ 31.4 °2θ. Moreover, the APS process did not promote the crystallization of the oxides of the BG45S5 in the feedstock powders deposition. This is a desired structural characteristic in topcoat coatings of bioactive glasses taking into account that the amorphous structural characteristic of the coating represents a high reactivity of the surface, maximizing the bioactivity of the coating [32]. The diffraction peak at 27.2 °2θ with low intensity is associated with the presence of Bi_2O_3 (ISCD 98-003-8436) which was promoted by the plasma high temperatures and the low cooling rate of the coating due to the continuous exposition to plasma during the powder deposition. Nevertheless, the coating is still considered amorphous. Regarding the peak ~ 43.6 °2θ was identified as Fe (ICSD 98-005-3803) and the diffraction peak from the substrate which indicates the low and heterogeneous thickness of the BG45S5+10Bi_2O_3 coating agreeing with the low thickness evidenced In Figure 37c.

2.3.3. Commercial BG45S5 and lab-made BG45S5+10Bi_2O_3 APS coatings bioactivity analysis after immersion in simulated body fluid (SBF)

The bioactivity of Commercial BG45S5 and lab-made BG45S5+10Bi_2O_3 was followed by SEM and XRD analysis of the surface coatings after 3, 5 and 10 days of immersion in SBF.

Scanning electron microscopy (SEM) surface micrographs

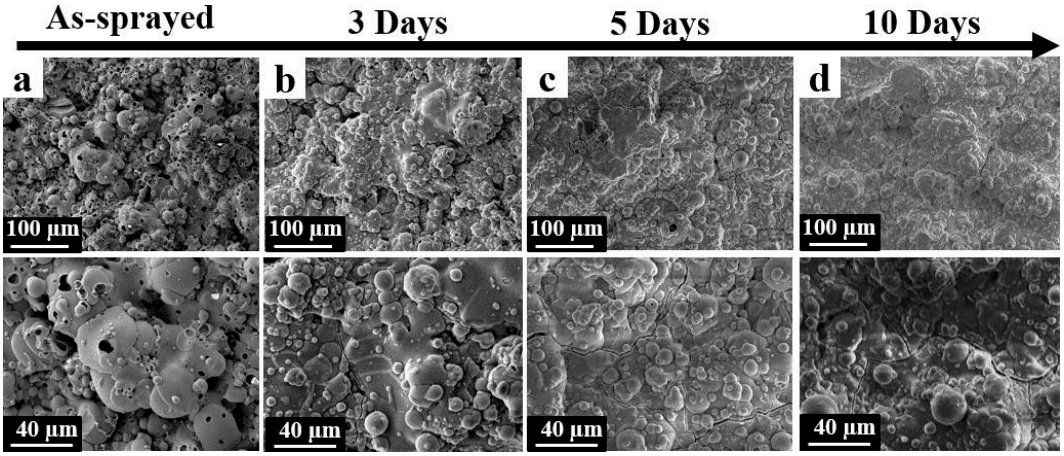

Figure 39. Apatite formation on the commercial BG45S5 APS coating surface monitored by SEM after immersion in SBF at a) 0, b) 3, c) 5 and d) 10 days. Each surface is shown at two magnifications: x 300, x 800.

Figure 40 presents SEM micrographs of the surface of commercial BG45S5 coatings after immersion in SBF during 3, 5 and 10 days. Micrographs of the as-sprayed coating were added for comparative purposes (see Figure 40a). After 3 days of immersion in SBF there are no micropores in comparison with the as-sprayed surface (see Figure 40b). Moreover, spherulites with different diameters (5 – 20 µm) and large microcracks are observed in all the coating surface. Additionally. the size of these spherulites is more homogeneous after 5 days of immersion in SBF (see Figure 40c) and microcracks are more evident. Finally, spherulites are in the coating after10 days of immersion in SBF are more numerous and the surface of the coating is more homogenous with more visible microcracks (see Figure 40d).

Figure 40 shows the typical morphology changes in BG45S5 after exposition to SBF. During this immersion, the pores were filled with calcium phosphate deposits, as expected in the apatite growth at its first stages. The high reactivity of the BG45S5 coating promotes the rapid apatite formation characterized by the typical globular morphology. The growth of this layer is evidenced by the increased number and size of the spherulites as is seen in Figure 40c and Figure 40d. The microcracks are caused the partial ion diffusion with the simulated fluid as was

explained in session 2.1.4. From this analysis is concluded that commercial BG45S5 shows high bioactivity as predicted from its structural characterization.

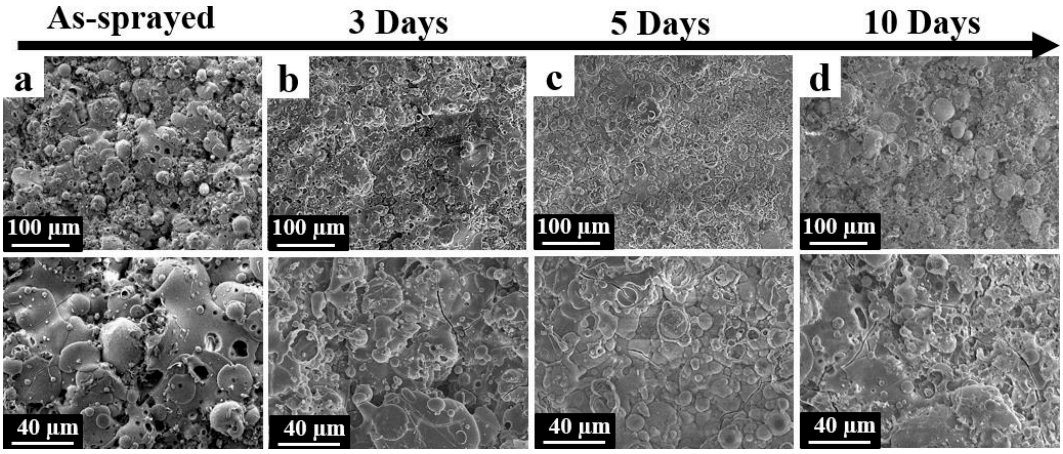

Figure 40. Apatite formation on the lab-made BG45S5+10Bi_2O_3 APS coating surface monitored by SEM after immersion in SBF at a) 0, b) 3, c) 5 and d) 10 days. Each surface is shown at two magnifications: 300 x, 800 x.

A similar analysis of BG45S5+10 Bi_2O_3 coating after immersion in SBF is presented in Figure 40. Similarly to BG45S5 coating, the surface coating porosity was reduced after 3 days of immersion in SBF in comparison with the as-sprayed surface (see Figure 40a and Figure 40b). After immersion to SBF during this period, fewer and smaller spherulites and microcracks were observed compared to immersed commercial BG45S5 coating. Despite the increment in the number of these spherulites after 5 days of immersion (see Figure 40c), this morphology is poorly seen in the surface of the coating after 10 days and delaminated zones are also seen (see Figure 40d). The apatite grown deposition rate was reduced in comparison with the APS coating of the bioactive glass without Bi_2O_3 radio-opacifier. This is noticed by the small and reduced number of spherulites formed in the coating surface after 3 days of immersion in SBF. The reduction in the ability to form the apatite layer and its stability in the surface after immersion in SBF is related to the increment in the network connectivity and the reduction of non-bridging oxygen as is reported by S. Prasath et al. [46]. In these contributions, additions of 4 and 8 wt. % of Bi_2O_3 in BG obtained by the melt and fast quenching results show similar bioactivity results compared to the APS thermally sprayed coatings. Despite the reduced bioactivity of the thermally sprayed BG, the coating performance is still being good as a biomaterial considering the apatite formation during the studied days in addition to the improved radio-opacity.

X-ray diffraction analysis (XRD)

The structural characterization of the commercial BG45S5 and lab-made BG45S5+10Bi_2O_3 coatings after immersion in SBF by XRD are shown in Figure 41. The XRD patterns of the as-

sprayed coatings are also presented. The structural changes of the structure of commercial BG45S5 are characterized by the appearance of peaks at 26, 31.9, 33.9, 40, and 53.1 °2θ with a reduced mean width in comparison with the BGcharacteristic diffraction band in the as-sprayed diffractogram (Figure 41a). The intensity of the peak at 26 and 33.9 °2θ was increased after 5 and 10 days of immersion. Additionally, a small peak was observed at 43.3 °2θ. Regarding the XRD patterns of lab-made BG45S5+10Bi_2O_3 coatings after immersion in SBF presented in Figure 41b, the diffractograms show the appearance of small peaks at 26, 31.9 and 40 °2θ after 5 days of immersion. Moreover, the intensity of peaks at 43.3, 44.5 and 50.7 °2θ was increased after the same time of immersion, decreased after 10 days. Finally, a diffraction peak at 27.2 °2θ was observed in all the diffractograms.

The diffraction of peaks at 26, 31.9, 33.9, 40, and 53.1 °2θ in Figure 41a are associated with the formation of the apatite layer on the surface of the commercial BG45S5 coating. The increased intensity of these peaks demonstrates the progressive growth of this layer during the immersion in the simulated fluid and the bioactive behavior of the coating after 3, 5 and 10 days of immersion. The small peak observed at 43.3 °2θ is associated with Fe from the substrate which indicates that there are some delaminated zones in the coating. Analyses at higher immersion times are needed in other to further explain the stability of the coating in SBF.

The diffractograms of lab-made BG45S5+10Bi_2O_3 (see Figure 41b) show a slower apatite growth on its surface according to the peaks at 26, 31.9 and 40 °2θ in diffractograms after 5 days of immersion. The increment of the intensity of the peaks at 43.3, 44.5 and 50.7 °2θ are associated with the delaminated zones indicating that delamination was higher in comparison with the commercial BG45S5 coating after interaction with SBF. The crystalline phase of Bi_2O_3 related to the peak 27.2 °2θ demonstrates that this phase was stable after interaction with SBF supporting the hypothesis that the presence of Bi_2O_3 reduces the number of non-bridging oxygen. The results here presented agreeing with the SEM micrographs analysis presented in Figure 40.

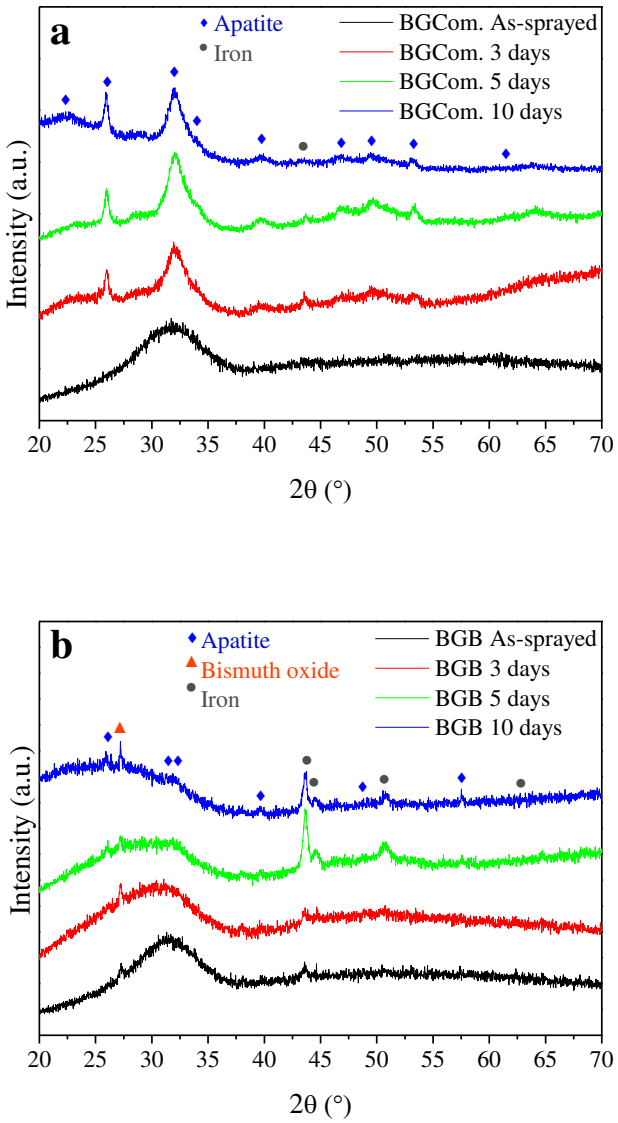

Figure 41. Structural characterization by XRD of BG45S5 APS coatings after 0, 3, 5 and 10 days of immersion in SBF: a) commercial BG45S5 and b) lab-made BG45S5+10Bi_2O_3.

Elements concentration measurements in SBF by ICP after coatings immersion

Ca and P concentration in the SBF after interaction with commercial BG45S5 and lab-made BG45S5+10Bi_2O_3 was followed by ICP analysis and the results are shown in Figure 42. The Ca concentration in SBF from commercial BG45S5 (see Figure 42a) and undergoes under an increment of 7.2 mg/L and decreases to 110.1 mg/L after 3 and 5 days of immersion, respectively. Finally, the Ca concentration was incremented by 24 mg/L after 10 days of immersion in SBF. In addition, the P concentration in the same SBF was decreased from 30 mg/L to 1.3 during the firsts 3 days of immersion and this tendency continues until a concentration of 0.4 mg/L at 10 days. The Ca concentration from SBF of lab-made

BG45S5+10Bi_2O_3 observed in Figure 42b was approximately constant with variations of ± 8.2 mg/L. Regarding P concentration was decreased to 4.2, 3.4 and 1.2 mg/L after 3, 5 and 10 days, respectively.

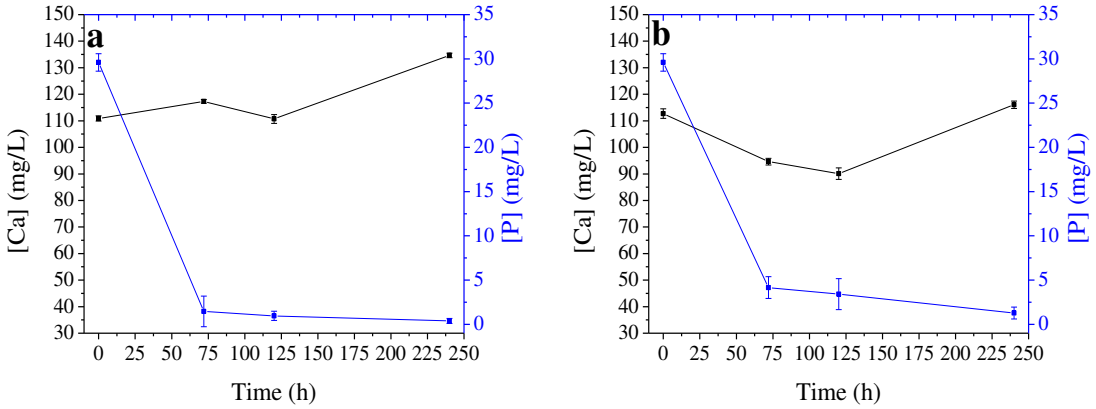

Figure 42. Ca and P concentration in SBF after 3, 5 and 10 days of BG45S5 APS coatings immersion: a) commercial BG45S5 and b) lab-made BG45S5+10Bi_2O_3.

The concentration tendency of Ca and P in SBF is similar to that one from the bioactivity analysis of the commercial BG45S5 feedstock powder (see section 1.2.4. Figure 12). Ca decrements after 3 days of immersion are due to the deposition of this element in the coating at the first stages of the apatite formation. Additionally, the P reductions in SBF are associated with the rapid intake of this element from the SBF to the coating surface which indicates rapid bioactivity of both coatings. However, this reduction was higher in the P concentration of the SBF of commercial BG45S5 coating. This is another sign of the higher apatite forming ability this coating in comparison with the lab-made BG45S5+10Bi_2O. Nonetheless, the rapid P intake of the coating obtained by the lab-made feedstock powder demonstrates the ability of this coating to promote the deposition of the apatite layer in interaction with SBF and, consequently, its bioactivity.

2.4.GRADED BHAp/BG45S5+10Bi_2O_3 COATING OBTAINED BY APS

The fabrication and analysis of the APS BHAp coatings and BG45S5+10Bi_2O_3 coatings obtained by using lab-made feedstock powders presented in sections 2.1, 2.2 and 2.3, shows the high bioactive BHAp coatings with high crystallinity and an amorphous BG45S5+10Bi_2O_3 coating with a proper apatite forming ability. Thus, is expected to fabricate a gradual BHAp/ BG45S5+10Bi_2O_3 that increases the stability and bioactivity of the radio-opaque

BG45S5+10Bi_2O_3 topcoat by the deposition of both biomaterials in a gradual configuration. The analysis of this coating is presented in this section.

2.4.1. Graded BHAp/BG45S5+10Bi_2O_3 APS coating morphology, microstructure and elemental composition characterization by scanning electron microscopy- energy-dispersive x-ray spectroscopy (SEM-EDS)

The cross-section of the gradually sprayed BHAp/ BG45S5+10Bi_2O_3 coating has a thickness of 145.5 ± 15.3 µm according to Figure 43a. The microstructure shows the typical APS coating lamella architecture with very small pores which are not in the interface between the splats. Fully melted splats and some shell-like semi-melted particles are seeing on the surface of the coating (see Figure 43b). Additionally, no differentiable layers are seen,

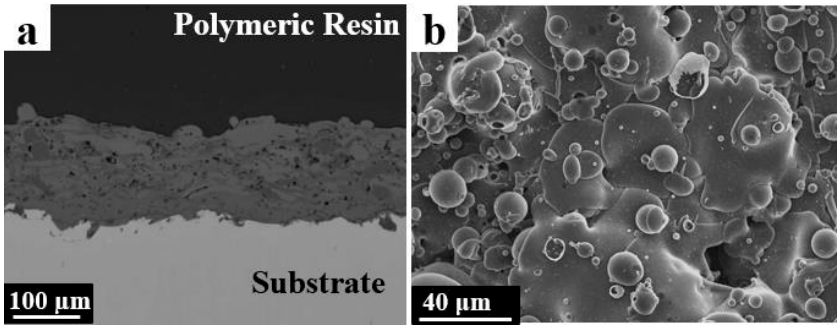

Figure 43. SEM micrographs of graded BHAp/BG45S5+10Bi_2O_3 APS coating: a) cross-section and b) surface.

The thickness of the coating was greater compared to the previous BHAp or BG APS coatings due to the chosen methodology to spray the gradual coating in which 4 layers with gradual ratios of BHAp/BG were deposited separately. Few pores are seen in the 100 % BHAp first layer as expected based on the results obtained in section 2.2. Furthermore, the open shell-like particles observed in Figure 43b are associated with the entrapped gas during the particle spray and coating cooling rate [78]. However, this type of particle and pores either in the surface or the cross-section caused by the same phenomena are reduced in comparison with the analysis of single BG45S5+Bi_2O_3 APS coating. This is explained by the reduction of the exposure time of the coating to the plasma during each layer deposition. On the other hand, the homogenous microstructure of the coating and the lack of interlayer boundaries demonstrates that the multilayer's deposition was not detrimental for the adherence of the previous deposits and a proper cohesion is seen among the layers.

Figure 44 and Figure 45 shows the EDS analysis of the cross-section of the coating in order to determine the elemental distribution and gradual architecture. The SEM micrograph of the

coating and a schematic drawing of the gradual microstructure are also shown for comparative purposes.

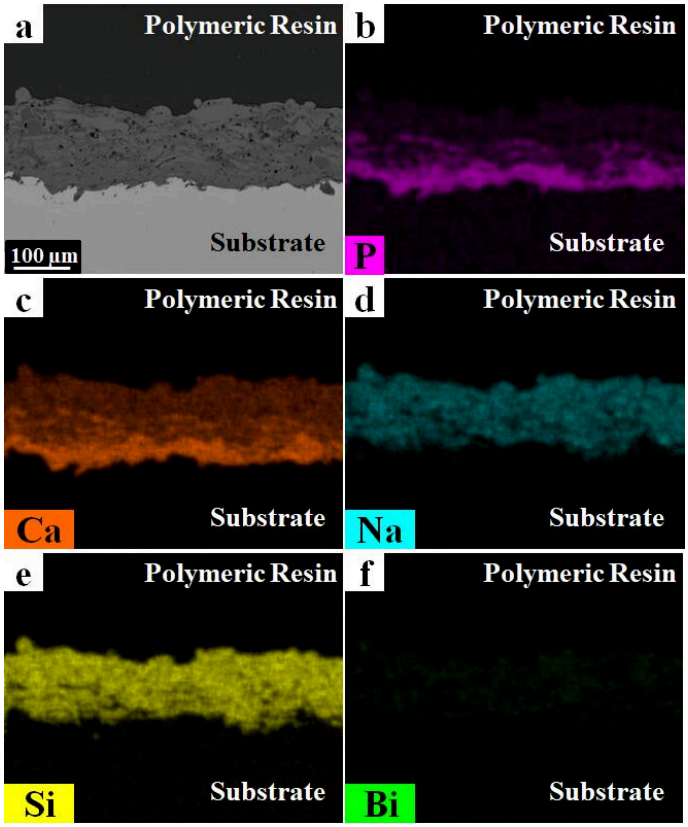

Figure 44. EDS Map analysis of graded BHAp/BG45S5+10Bi_2O_3 APS coating cross-section: a) Secondary electron micrograph, b) Phosphorus, c) Calcium, d) Sodium, e) Silicon and f) Bismuth.

Figure 44b and Figure 44c present the elemental analysis of P and Ca in the coating respectively, showing a mayor density in the interface with the substrate and some dense areas in the middle of the coating. The density of both elements is gradually decreased from the bottom to the top where the presence of Ca higher than P.

The elemental analysis of Na and Si is shown in Figure 44c and Figure 44d. These elements are not observed in the first layer on the coating and its distribution is homogenous after the BHAp layer. In addition, Si density is higher than the Ca or Na and the Bi density is low being homogeneously distributed after the first quarter of the coating cross-section.

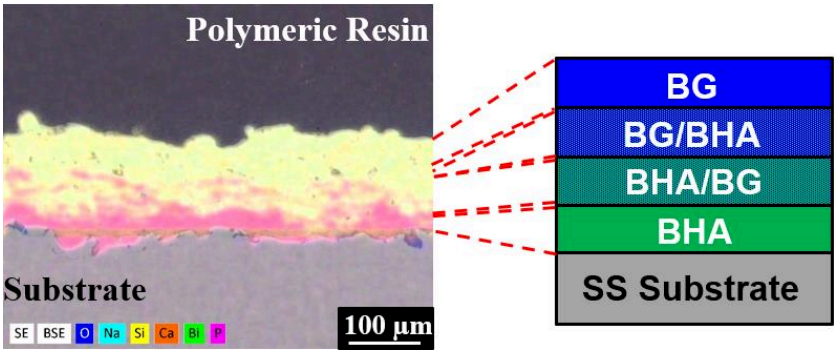

Figure 45. EDS Map analysis of graded BHAp/BG45S5+10Bi_2O_3 APS coating cross-section. A schematic figure of the gradual architecture is shown (right).

BHAp in the EDS analysis is characterized by the high density of Ca and P which is expected based on the high content of these elements in its composition. The dense areas are seen beyond the middle of coating cross-section agreeing with the third deposited layer using a feedstock powder ratio of 25:75 of BHAp:BG45S5+10Bi_2O_3. After this, the P density is lower compared to Ca considering that the concentration of P_2O_5 is 17.5 wt. % lower than the CaO concentration in the BHAp:BG45S5+10Bi_2O_3 feedstock powder. The density of Na is comparable to the Ca density after the first quarter of the coating cross-section and Si density is grater than Na and Ca as a consequence of their concentration in the BG feedstock powder. Similarly, the Bi density is in agreement with its concentration in the BG45S5+10Bi_2O_3. Furthermore, the homogenous density of this element in the coating where quantities of BG45S5+10Bi_2O_3 have been added probes that the used methodology in the glass preparation assures a proper mixture of the used oxides. Therefore, the radio-opaque response of the feedstock powder and coating can be considered as uniform in all the surfaces of the materials which represent an advantage for the desired radio-opaque performance. As is seen in Figure 45 the gradual architecture of BHAp and BG45S5+10Bi_2O_3 was obtained by using the method proposed in section 2.4.

2.4.2. Gradual BHAp/BG45S5+10Bi_2O_3 coating structural characterization by x-ray diffraction (XRD)

Figure 46 shows the structural characterization of the gradual BHAp/BG45S5+10Bi_2O_3 coating. The XRD pattern shows a diffraction peak at 27.2 °2θ followed by a broad diffraction band between 25 and 37 °2θ. The XRD pattern agrees with the analysis in section 2.3.2. The diffraction peak at 27.2 °2θ and the broad-band are present as a result of the amorphous structure of the BG45S5 and the presence of Bi_2O_3. Therefore is concluded that the structure of the

gradual coating is the same as the single BG45S5+10Bi_2O_3 coating which is expected considering the thickness of the topcoat and its composition.

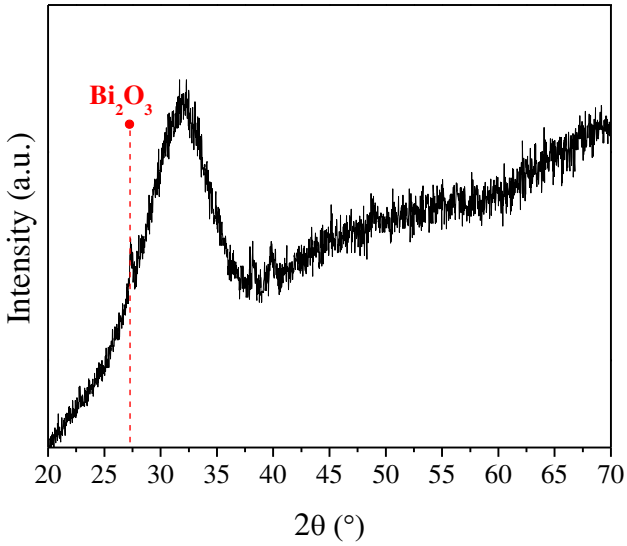

Figure 46. Structural characterization by XRD of the surface of gradual BG45S5+10Bi_2O_3 APS coating.

2.4.3. Graded BHAp/BG45S5+10Bi_2O_3 coating bioactivity analysis after immersion in simulated body fluid (SBF)

Scanning electron microscopy (SEM) surface micrographs

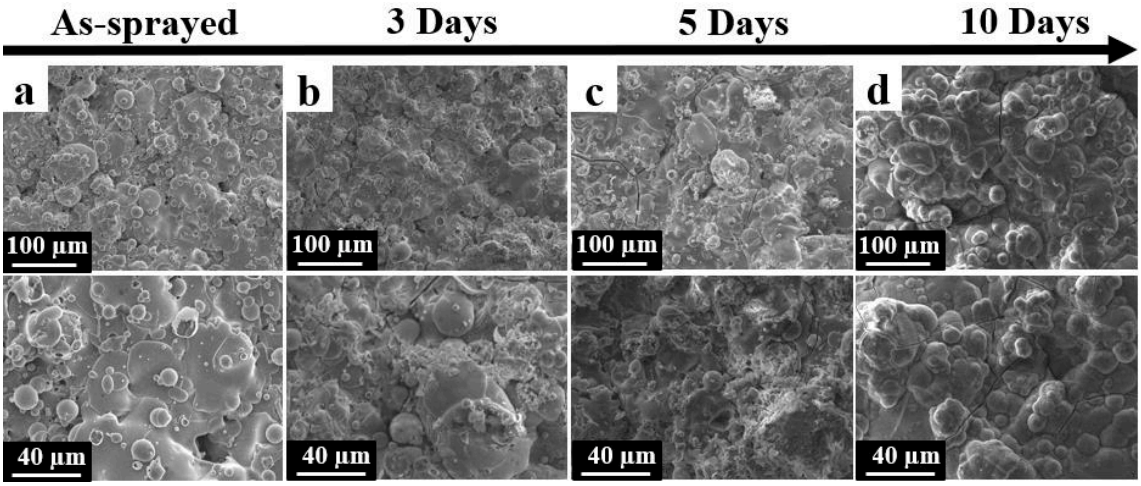

Figure 47. Apatite formation on the graded BHAp/BG45S5+10Bi_2O_3 APS coating surface monitored by SEM after immersion in SBF at a) 0, b) 3, c) 5 and d) 10 days. Each surface is shown at two magnifications: 300 x, 800 x.

SEM micrographs of the surface of the gradual BHAp/BG45S5+10Bi_2O_3 coating after immersion in SBF during 3. 5 and 10 days are observed in Figure 47. The SEM micrographs of

the as-sprayed surface are also shown in Figure 47a. The edges of some splats limits vanished and some microcracks and deposits irregular shaped are seen after 3 and 5 days of immersion (see Figure 47b and Figure 47c), which is more evident in the micrographs in Figure 47b. Moreover, a small spherulite with a diameter of ~ 10 µm is seen after 5 days of immersion at a magnification of x 800. After 10 days of immersion in SBF, the coating shows a globular like morphology all along its surface with several spherulites and microcracks.

Despite the lack of visible spherulites after 3 and 5 days of immersion in SBF the vanished edges of splats and microcracks formation indicate that the deposition of calcium phosphates occurs and the growth beginning of the apatite layer. The irregular shaped deposits are attributed to salt deposits from the SBF showing that the samples were not fully washed and cleaned for the SEM characterization which could explain the low visibility of apatite spherulites in Figure 47b and Figure 47c. The coating shows a high forming apatite ability after 10 days of immersion in contrast to the results of a single BG45S5+10Bi_2O_3 coating in section 2.3.3. BHAp presence on the gradual coating increased the stability of BG45S5+10Bi_2O_3 in immersion in SBF. Therefore no delamination took place in the gradual coating after 10 days of immersion allowing the rapid apatite growth on the surface. The possible ion migration from the coating to the SBF due to the coating porosity and its role in the bioactivity is not discarded and it needs to be further analyzed.

X-ray diffraction analysis (XRD)

Figure 48 presents the XRD diffractograms of gradual BHAp/BG45S5+10Bi_2O_3 coating after immersion in SBF during 3, 5 and 10 days. A broadening of the diffraction band between 25 and 37 °θ and the diffraction of the peak at 27.2 °2θ is observed in the coatings XRD pattern after 3, 5 and 10 days of immersion in SBF. In addition, similar diffraction peaks at 31.9, 33.9 °2θ are seen in all the diffractograms with greater intensities in the XRD pattern of the coating immersed at 10 days. This diffractogram shows an additional diffraction peak at 26 °2θ. Furthermore, a diffraction peak of similar intensity of that one at 27.2 °2θ is observed at 29.4 °2θ in the XRD pattern of the sample immersed at 3 days.

The broadening of all the XRD patterns of coatings after immersion in SBF is associated with the apatite layer deposition at its first stages. The growth of this layer is also evidenced by the diffraction peaks at 31.9, 33.9 °2θ. This growth is more evident in the diffractogram of the XRD coating after 10 days of immersion which presents an additional apatite diffraction peak at 26°2θ. The salt deposits seen in the SEM analysis of immersed coatings were evidenced in the

XRD pattern of the coating after 3 days of immersion by the diffraction of the peak at 29.4 °2θ associated with a Na salt compound.

The higher apatite ability forming of the gradual coating in comparison with the single BG45S5+10Bi_2O_3 is again confirmed agreeing with the previous SEM analysis.

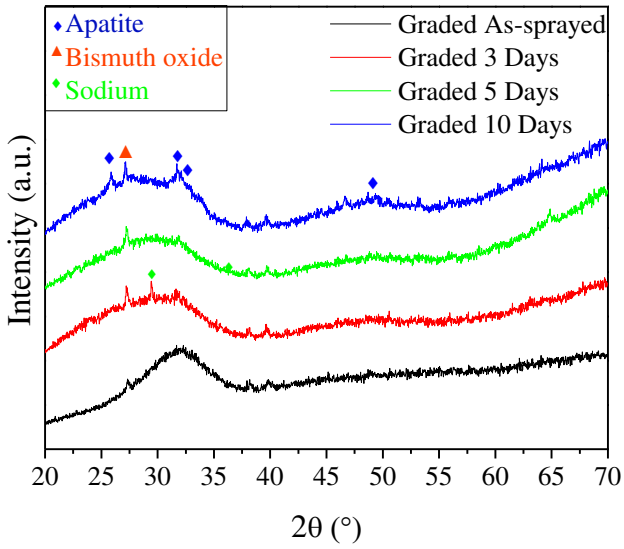

Figure 48. Structural characterization by XRD of graded BHAp/BG45S5+10Bi_2O_3 APS coating after 0, 3, 5 and 10 days of immersion in SBF.

Elements concentration measurements in SBF by ICP after coatings immersion

The Ca and P concentration in the SBF monitored by ICP during the bioactivity analysis of graded BHAp/BG45S5+10Bi_2O_3 APS coating during the evaluated days is presented in Figure 49. Ca was maintained in the range of 109.2 ± 10 mg/L from 0 to 3 days of immersion. This concentration was increased to 151 mg/L at 10 days of immersion. Regarding P concentration was decreased from 29.6 to 6.7 mg/L during the first 3 days of immersion. Afterward, the decreasing rate was decelerated and P concentration was 4.5 mg/L and 15.7 mg/L after 5 and 10 days of immersion, respectively.

Ca concentration was in agreement with the results in the bioactivity analysis of lab-made BG45S5 powder and lab-made BG45S5+10Bi_2O_3 APS coating until 5 days of immersion. However, this concentration was increased by 40 mg/L. Similarly to commercial BG45S5 APS coating the Ca concentration was increased at 10 days of immersion in SBF. The Ca-rich deposition layer at the first stages of apatite growth noted by the Ca decreased concentration after 3 and 5 days of immersion. Afterward, the Ca uptake from the coating surface is reduced

followed by the increased P uptake. Based on this and the rapid formation of the apatite layer after 10 days of immersion, the Ca concentration was increased after the apatite formation seen also in the SEM micrographs. Finally, P uptake from the coating was as expected according the previously reported BG45S5 powder and lab-made BG45S5+10Bi_2O_3 APS coating bioactivity. This uptake is characterized by the rapid P concentration decrease at the 3 days of immersion caused by the apatite ability of the coating.

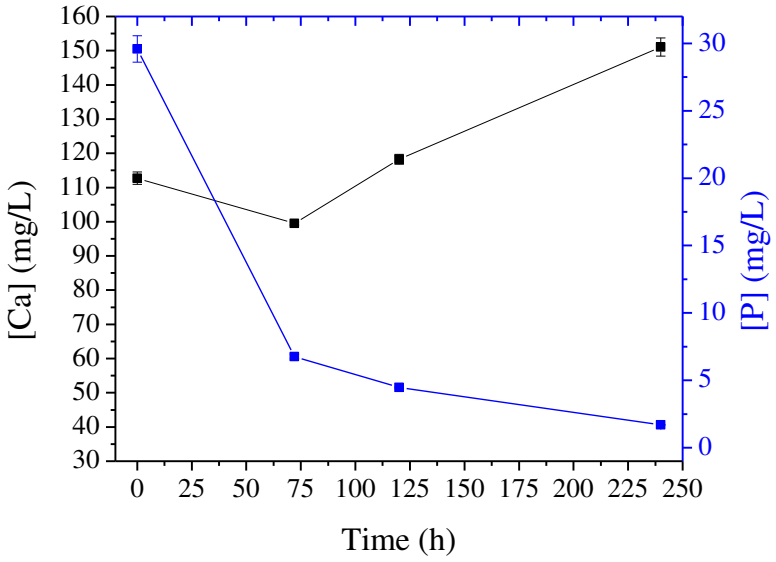

Figure 49. Ca and P concentration in SBF after 3, 5 and 10 days of graded BHAp/BG45S5+10Bi_2O_3 APS coatings immersion.

REFERENCES

[1] A. Maidaniuc, F. Miculescu, S.I. Voicu, C. Andronescu, M. Miculescu, E. Matei, A.C. Mocanu, I. Pencea, I. Csaki, T. Machedon-Pisu, L.T. Ciocan, Induced wettability and surface-volume correlation of composition for bovine bone derived hydroxyapatite particles, Appl. Surf. Sci. 438 (2018) 158–166. doi:10.1016/j.apsusc.2017.07.074.

[2] K. a. Khor, H. Li, P. Cheang, Significance of melt-fraction in HVOF sprayed hydroxyapatite particles, splats and coatings, Biomaterials. 25 (2004) 1177–1186. doi:10.1016/j.biomaterials.2003.08.008.

[3] W. Tong, J. Chen, X. Li, Y. Cao, Z. Yang, J. Feng, X. Zhang, Effect of particle size on molten states of starting powder and degradation of the relevant plasma-sprayed hydroxyapatite coatings, Biomaterials. 17 (1996) 1507–1513. doi:10.1016/0142-9612(96)89775-4.

[4] P. Cheang, K.A. Khor, Thermal spraying of hydroxyapatite (HA) coatings effects of powder feedstock, J. Mater. Process. Technol. 48 (1995) 429–436. doi:10.1016/0924-0136(94)01679-U.

[5] C. Rey, M. Shimizu, B. Collins, M.J. Glimcher, Resolution-Enhanced Fourier Transform Infrared Spectroscopy Study of the Environment of Phosphate Ion in the Early Deposits of a Solid Phase of Calcium Phosphate in Bone and Enamel and their Evolution with Age: 2. Investigations in the v3 PO4 Domain, (1991) 383–388.

[6] C. Rey, M. Shimizu, B. Collins, M.J. Glimcher, Resolution-Enhanced Fourier Transform Infrared Spectroscopy Study of the Environment of Phosphate Ions in the Early Deposits of a Solid Phase of Calcium-Phosphate in Bone and Enamel , and their Evolution with Age . I : Investigations in the v4 PO4 Domain, Clacified Tissue Int. (1990) 384–394.

[7] S. Marković, L. Veselinović, M.J. Lukić, L. Karanović, I. Bračko, N. Ignjatović, D. Uskoković, Synthetical bone-like and biological hydroxyapatites: a comparative study of crystal structure and morphology., Biomed. Mater. 6 (2011) 045005. doi:10.1088/1748-6041/6/4/045005.

[8] D.K. Pattanayak, P. Divya, S. Upadhyay, R.C. Prasad, B.T. Rao, T.R. Rama Mohan, Synthesis and evaluation of hydroxyapatite ceramics, Trends Biomater. Artif. Organs. 18 (2005) 87–92.

[9] ASTM F1581-08(2016), Standard Specification for Composition of Anorganic Bone for Surgical Implants, ASTM Int. (2016).

[10] M. Jevtic, M. Mitric, S. Skapin, B. Jancar, N. Ignjatovic, D. Uskokovic, Crystal Structure of Hydroxyapatite Nanorods Synthesized by Sonochemical Homogeneous Precipitation, Cryst. Gorwth Des. 8 (2008) 2217–2222.

[11] C. Rey, B. Collins, T. Goehl, I.R. Dickson, M.J. Glimcher, The Carbonate Environment in Bone Mineral : A Resolution-Enhanced Fourier Transform Infrared Spectroscopy Study Preparation of Bone Samples, (1989) 157–164.

[12] F. Ren, Y. Ding, Y. Leng, Infrared spectroscopic characterization of carbonated apatite : A combined experimental and computational study, J. Biomed. Mater. Res. - Part A. 102 (2014) 496–505. doi:10.1002/jbm.a.34720.

[13] S.V. Dorozhkin, Calcium orthophosphates (CaPO 4): Occurrence and properties, Prog. Biomater. 5 (2016) 9–70. doi:10.1016/j.morpho.2017.03.007.

[14] L. Berzina-Cimdina, N. Borodajenko, Research of Calcium Phosphates Using Fourier Transform Infrared Spectroscopy, in: T. Theophile (Ed.), Infrared Spectrosc. – Mater. Sci. Eng. Technol., InTech Published, 2012: pp. 123–148.

[15] M.M. Figueiredo, J.A.F. Gamelas, A.G. Martins, Characterization of Bone and Bone-Based Graft Materials Using FTIR Spectroscopy, in: T. Theophile (Ed.), Infrared Spectrosc. - Life Biomed. Sci., InTech, 2012: pp. 315–338.

[16] D. Haverty, S.A.M. Tofail, K.T. Stanton, J.B. Mcmonagle, Structure and stability of hydroxyapatite : Density functional calculation and Rietveld analysis, Phys. Rev. B. (2005) 1–9. doi:10.1103/PhysRevB.71.094103.

[17] J.A. Rincon-López, J.A. Hermann-Muñoz, A.L. Giraldo-Betancur, A. De Vizcaya-Ruiz, J.M. Alvarado-Orozco, J. Muñoz-Saldaña, Synthesis, Characterization and In Vitro Study of Synthetic and Bovine-Derived Hydroxyapatite Ceramics: A Comparison, Materials (Basel). 11 (2000) 1–17. doi:10.3390/ma11020333.

[18] A. Prokopiuk, B. Budner, Structural studies of magnesium doped hydroxyapatite coatings after osteoblast culture, J. Mol. Struct. 977 (2010) 145–152. doi:10.1016/j.molstruc.2010.05.025.

[19] L. Mayer, R. Scblam, J.D.B. Featberstone, Magnesium-Containing Carbonate Apatites,

J. Inorg. Biochem. 66 (1997) 1–6. doi:10.1016/S0162-0134(96)00145-6.

[20] R. Murugan, T.S.S. Kumar, K.P. Rao, Fluorinated bovine hydroxyapatite: preparation and characterization, Mater. Lett. 57 (2002) 429–433. doi:10.1016/S0167-577X(02)00805-4.

[21] M.S. Sader, K. Lewis, G.A. Soares, R.Z. Legeros, Simultaneous Incorporation of Magnesium and Carbonate in Apatite : Effect on Physico-chemical Properties, Mater. Reserch. 16 (2012). doi:10.1590/S1516-14392013005000046.

[22] C. Lin, Na2 – CaSi2O6 – P2O5 based bioactive glasses . Part 1 : Elasticity and structure, J. Non. Cryst. Solids. 351 (2005) 3195–3203. doi:10.1016/j.jnoncrysol.2005.08.020.

[23] E. Dietrich, Synthèse et études physico-chimiques de verres bioactifs denses et poreux. Applications en tant que biomatériaux en sites osseux, 2008.

[24] L. Lefebvre, J. Chevalier, L. Gremillard, R. Zenati, G. Thollet, D. Bernache-Assolant, A. Govin, Structural transformations of bioactive glass 45S5 with thermal treatments.., Acta Mater. 55 (2007) 3305–3313. doi:10.1016/j.actamat.2007.01.029.

[25] T. Process, C. Centre, Crystallization of 45S5 during Isothermal Heat Treatment, Ceram. Mater. 62 (2010) 349–354.

[26] H. Ohsato, I. Maki, Structure of Na2CaSi2O6, Acta Crystallogr. Sect. C Cryst. Struct. Commun. C41 (1985) 1575–1577. doi:10.1107/S0108270185008617.

[27] A.R. Boccaccini, Q. Chen, L. Lefebvre, Sintering, crystallization and biodegradation behaviour of Bioglass-derived glass – ceramics, Faraday Discuss. 136 (2007) 27–44. doi:10.1039/b616539g.

[28] D. Bellucci, V. Cannillo, A. Sola, R. Emilia, V. Vignolese, M. Mo, An Overview of The Effects of Thermal Processing on Bioactive Glasses, Sci. Sinter. 42 (2010) 307–320. doi:10.2298/SOS1003307B.

[29] V. López, M.V. Cabedo, E. Bannier, E.C. Recacha, A.R. Boccaccini, L.C. Arias, E.S. Vilches, 45S5 bioactive glass coatings by atmospheric plasma spraying obtained from feedstocks prepared by different routes, J. Mater. Sci. 49 (2014) 7933–7942. doi:10.1007/s10853-014-8519-2.

[30] N.F. Ibrahim, H. Mohamad, Effects of milling media on the fabrication of melt-derived

bioactive glass powder for biomaterial application, in: AIP Conf. Proc., 2016: pp. 1–7. doi:10.1063/1.4968865.

[31] R.G. Hill, D.S. Brauer, Predicting the bioactivity of glasses using the network connectivity or split network models, J. Non. Cryst. Solids. 357 (2011) 3884–3887. doi:10.1016/j.jnoncrysol.2011.07.025.

[32] J. Jones, A. Clare, Bio-glasses: an introduction, Wiley, 2012.

[33] S. Fujibayashi, M. Neo, H.M. Kim, T. Kokubo, T. Nakamura, A comparative study between in vivo bone ingrowth and in vitro apatite formation on Na2O-CaO-SiO2 glasses, Biomaterials. 24 (2003) 1349–1356. doi:10.1016/S0142-9612(02)00511-2.

[34] I. Farooq, Z. Imran, U. Farooq, A. Leghari, H. Ali, Bioactive Glass: A Material for the Future, World J. Dent. 3 (2012) 199–201. doi:10.5005/jp-journals-10015-1156.

[35] X. Chatzistavrou, T. Zorba, E. Kontonasaki, K. Chrissafis, P. Koidis, K.M. Paraskevopoulos, Following bioactive glass behavior beyond melting temperature by thermal and optical methods, Phys. Status Solidi Appl. Res. 201 (2004) 944–951. doi:10.1002/pssa.200306776.

[36] D. Groh, F. Döhler, D.S. Brauer, Bioactive glasses with improved processing. Part 1. Thermal properties, ion release and apatite formation, Acta Biomater. 10 (2014) 4465–4473. doi:10.1016/j.actbio.2014.05.019.

[37] J. Massera, S. Fagerlund, L. Hupa, M. Hupa, Crystallization mechanism of the bioactive glasses, 45S5 and S53P4, J. Am. Ceram. Soc. 95 (2012) 607–613. doi:10.1111/j.1551-2916.2011.05012.x.

[38] O. Bretcanu, X. Chatzistavrou, K. Paraskevopoulos, R. Conradt, I. Thompson, A.R. Boccaccini, Sintering and crystallisation of 45S5 Bioglass ® powder, 29 (2009) 3299–3306. doi:10.1016/j.jeurceramsoc.2009.06.035.

[39] A.L.B. Maçon, T.B. Kim, E.M. Valliant, K. Goetschius, R.K. Brow, D.E. Day, A. Hoppe, A.R. Boccaccini, I.Y. Kim, C. Ohtsuki, T. Kokubo, A. Osaka, M. Vallet-Regí, D. Arcos, L. Fraile, A.J. Salinas, A. V Teixeira, Y. Vueva, R.M. Almeida, M. Miola, C. Vitale-Brovarone, E. Verné, W. Höland, J.R. Jones, A unified in vitro evaluation for apatite-forming ability of bioactive glasses and their variants, J. Mater. Sci. Mater. Med. 26 (2015) 1–10. doi:10.1007/s10856-015-5403-9.

[40] S. AG, SCHOTT Technical Glass Powders: Product Information, n.d. https://www.schott.com/d/epackaging/6c468bf9-72b6-40da-9154-433773ef2c36/1.5/schott-technical-glass-powders_eng.pdf.

[41] A.K. Srivastava, R. Pyare, S.P. Singh, Elastic Properties of substituted 45S5 Bioactive Glasses and Glass – Ceramics, Int. J. Sci. Eng. Res. 3 (2012) 1–13. http://www.tandfonline.com/doi/full/10.1080/01442870802576207?scroll=top&needAccess=true&instName=Queen+Margaret+University.

[42] P. Sepulveda, J.R. Jones, L.L. Hench, Characterization of Melt-Derived 45S5 and sol-gel–derived 58S Bioactive Glasses, J. Biomed. Mater. Res. (2001) 564–569. doi:10.1002/jbm.0000.

[43] M. Mačković, A. Hoppe, R. Detsch, D. Mohn, W.J. Stark, E. Spiecker, A.R. Boccaccini, Bioactive glass (type 45S5) nanoparticles: In vitro reactivity on nanoscale and biocompatibility, J. Nanoparticle Res. 14 (2012) 1–22. doi:10.1007/s11051-012-0966-6.

[44] L.A. Adams, E.R. Essien, R.O. Shaibu, A. Oki, Sol-Gel Synthesis of SiO2-CaO-Na2O-P2O5 Bioactive Glass Ceramic from Sodium Metasilicate, 2013 (2013) 11–15. doi:10.4236/njgc.2013.31003 ublished.

[45] Y. Xiao, L. Song, X. Liu, Y. Huang, T. Huang, Y. Wu, J. Chen, F. Wu, Applied Surface Science Nanostructured bioactive glass – ceramic coatings deposited by the liquid precursor plasma spraying process, Appl. Surf. Sci. 257 (2011) 1898–1905. doi:10.1016/j.apsusc.2010.09.023.

[46] S. Prasad, I. Ratha, T. Adarsh, A. Anand, P.K. Sinha, P. Diwan, K. Annapurna, K. Biswas, In vitro bioactivity and antibacterial properties of bismuth oxide modified bioactive glasses, J. Mater. Res. 33 (2018) 178–190. doi:10.1557/jmr.2017.442.

[47] B.S. Kim, E.S. Lim, J.H. Lee, J.J. Kim, Effect of Bi2O3 content on sintering and crystallization behavior of low-temperature firing Bi2O3-B2O3-SiO2 glasses, J. Eur. Ceram. Soc. 27 (2007) 819–824. doi:10.1016/j.jeurceramsoc.2006.04.013.

[48] R.B. Heimann, Thermal spraying of biomaterials, Surf. Coatings Technol. 201 (2006) 2012–2019. doi:10.1016/j.surfcoat.2006.04.052.

[49] I. Bran, M. Popescu, In vitro characterization of hydroxyapatite layers deposited by APS and HVOF thermal spraying methods, (2011) 25–31. doi:10.1016/S0142-

9612(02)00431-3.

[50] J.A. Hermann-Muñoz, J.A. Rincón-López, G.A. Clavijo-Mejía, A.L. Giraldo-Betancur, J.M. Alvarado-Orozco, A. De Vizcaya-Ruiz, J. Muñoz-Saldaña, Influence of HVOF parameters on HAp coating generation: An integrated approach using process maps, Surf. Coat. Technol. 358 (2019) 299–307. doi:10.1016/j.surfcoat.2018.11.029.

[51] H. Nascimento dos Santos, R. Neumann, C.A. Ávila, Mineral Quantification with Simultaneous Refinement of Ca-Mg Carbonates Non-Stoichiometry by X-ray Diffraction, Rietveld Method, Minerals. 7 (2017) 1–14. doi:10.3390/min7090164.

[52] M. Auenue, N. Jersey, Structural refinements of dolomite and magnesian calcite and Implications for Dolomite Formation in the Marine Environment, Am. Mineral. 62 (1977) 772–783.

[53] W. Xia, C. Lindahl, C. Persson, P. Thomsen, J. Lausmaa, H. Engqvist, Changes of Surface Composition and Morphology after Incorporation of Ions into Biomimetic Apatite Coatings, J. Biomater. Nanobiotechnol. 1 (2010) 7–16. doi:10.4236/jbnb.2010.11002.

[54] D. Yi, C. Wu, X. Ma, H. Ji, X. Zheng, Preparation and in vitro evaluation of plasma-sprayed bioactive akermanite, Biomed. Mater. 7 (2012) 1–9. doi:10.1088/1748-6041/7/6/065004.

[55] J. Ma, H. Wong, L.B. Kong, K.W. Peng, Biomimetic processing of nanocrystallite bioactive apatite coating on titanium, Nanotechnology. 14 (2003) 619–623. stacks.iop.org/Nano/14/619.

[56] J.M. Sadowska, F. Wei, J. Guo, J. Guillem-Marti, Z. Lin, M.P. Ginebra, Y. Xiao, The effect of biomimetic calcium deficient hydroxyapatite and sintered β-tricalcium phosphate on osteoimmune reaction and osteogenesis, Acta Biomater. 96 (2019) 605–618. doi:10.1016/j.actbio.2019.06.057.

[57] V. Sergo, O. Sbaizero, D.R. Clarke, Mechanical and chemical consequences of the residual stresses in plasma sprayed hydroxyapatite coatings, Biomaterials. 18 (1997) 477–482. doi:10.1016/S0142-9612(96)00147-0.

[58] H. Li, K.A. Khor, P. Cheang, Thermal sprayed hydroxyapatite splats: nanostructures , pore formation mechanisms and TEM characterization, Biomaterials. 25 (2004) 3463–

3471. doi:10.1016/j.biomaterials.2003.10.051.

[59] J. Weng, Q. Liu, J.G.C. Wolke, X. Zhang, K. De Groat, Formation and characteristics of the apatite layer on plasma-sprayed hydroxyapatite coatings in simulated body fluid, Biomaterials. 18 (1997) 1027–1035. doi:10.1016/S0142-9612(97)00022-7.

[60] B. Feng, J.Y. Chen, S.K. Qi, L. He, J.Z. Zhao, X.D. Zhang, Carbonate apatite coating on titanium induced rapidly by precalcification, Biomaterials. 23 (2002) 173–179. doi:10.1016/S0142-9612(01)00093-X.

[61] Y.. Gu, K.. Khor, P. Cheang, In vitro studies of plasma-sprayed hydroxyapatite/Ti-6Al-4V composite coatings in simulated body fluid (SBF), Biomaterials. 24 (2003) 1603–1611. doi:10.1016/S0142-9612(02)00573-2.

[62] S.W.K. Kweh, K.A. Khor, P. Cheang, An in vitro investigation of plasma sprayed hydroxyapatite (HA) coatings produced with flame-spheroidized feedstock, Biomaterials. 23 (2002) 775–785. doi:10.1016/S0142-9612(01)00183-1.

[63] S. Ha, R. Reber, K. Eckert, M. Petitmermet, C. Baerlocher, Chemical and Morphological Changes of Vacuum-Plasma-Sprayed Hydroxyapatite Coatings during Immersion in Simulated Physiological Solutions, J. Am. Ceram. Soc. 81 (1998) 81–88. doi:10.1111/j.1151-2916.1998.tb02298.x.

[64] J.N. Barry, D.P. Dowling, Comparison between the SBF response of hydroxyapatite coatings deposited using both a plasma-spray and a novel co-incident micro-blasting technique, in: Key Eng. Mater., 2012: pp. 483–488. doi:10.4028/www.scientific.net/KEM.493-494.483.

[65] Y. Otsuka, D. Kojima, Y. Mutoh, Prediction of cyclic delamination lives of plasma-sprayed hydroxyapatite coating on Ti–6Al–4V substrates with considering wear and dissolutions, J. Mech. Behav. Biomed. Mater. 64 (2016) 113–124. doi:10.1016/j.jmbbm.2016.07.026.

[66] Y. Wang, X. Liu, T. Fan, Z. Tan, Z. Zhou, D. He, In vitro evaluation of hydroxyapatite coatings with (002) crystallographic texture deposited by micro-plasma spraying, Mater. Sci. Eng. C. 75 (2017) 596–601. doi:10.1016/j.msec.2017.02.119.

[67] Z. Strnad, J. Strnad, C. Povýšil, K. Urban, Effect of Plasma-Sprayed Hydroxyapatite Coating on the Osteoconductivity of Commercially Pure Titanium Implants, Int. J. Oral

Maxillofac. Implant. 15 (2000) 483–490.

[68] R.S. Lima, K. a. Khor, H. Li, P. Cheang, B.R. Marple, HVOF spraying of nanostructured hydroxyapatite for biomedical applications, Mater. Sci. Eng. A. 396 (2005) 181–187. doi:10.1016/j.msea.2005.01.037.

[69] J. Fernández, M. Gaona, J.M. Guilemany, Effect of Heat Treatments on HVOF Hydroxyapatite Coatings, J. Therm. Spray Technol. 16 (2007) 220–228. doi:10.1007/s11666-007-9034-7.

[70] G.F. Dias, F.B.T. Alves, D.M. Samways, F.A. dos Santos, Mineral exchange between dentin pre-tretament with Dolomite powder on demineralized dentin in deciduous molars, Brazilian Dent. Sci. 21 (2018) 341. doi:10.14295/bds.2018.v21i3.1592.

[71] E.D. Eanes, S.L. Rattner, The Effect of Magnesium on Apatite Formation in Seeded Supersaturated Solutions at pH 7.4, J. Dent. Res. 60 (1981) 1719–1723. doi:10.1177/00220345810600091401.

[72] M.H. Salimi, J.C. Heughebaert, G.H. Nancollas, Crystal Growth of Calcium Phosphates in the Presence of Magnesium Ions, Langmuir. 1 (1985) 119–122. doi:10.1021/la00061a019.

[73] T. Aoba, E.C. Moreno, S. Shimoda, Competitive adsorption of magnesium and calcium ions onto synthetic and biological apatites, Calcif. Tissue Int. 51 (1992) 143–150. doi:10.1007/BF00298503.

[74] H.M. Kim, T. Himeno, T. Kokubo, T. Nakamura, Process and kinetics of bonelike apatite formation on sintered hydroxyapatite in a simulated body fluid, Biomaterials. 26 (2005) 4366–4373. doi:10.1016/j.biomaterials.2004.11.022.

[75] R.B. Heimann, Plasma-Sprayed Hydroxylapatite-Based Coatings: Chemical, Mechanical, Microstructural, and Biomedical Properties, J. Therm. Spray Technol. 25 (2016) 827–850. doi:10.1007/s11666-016-0421-9.

[76] A.M. Vilardell, N. Cinca, S. Dosta, I.G. Cano, X. Nogués, J.M. Guilemany, In-vitro comparison of hydroxyapatite coatings obtained by cold spray and conventional thermal spray technologies, Mater. Sci. Eng. C. (2019) 110306. doi:10.1016/j.msec.2019.110306.

[77] A.K. Lynn, D.L. DuQuesnay, Hydroxyapatite-coated Ti–6Al–4V Part 1: the effect of

coating thickness on mechanical fatigue behavior, Biomaterials. 23 (2002) 1937–1946. doi:10.1016/s0142-9612(01)00321-0.

[78] A. Cattini, Coatings of bioactive glasses and hydroxyapatite and their properties, Univesité de Limoges, 2013.

[79] G. Brunello, H. Elsayed, L. Biasetto, Bioactive Glass and Silicate-Based Ceramic Coatings on Metallic Implants: Open Challenge or Outdated Topic?, Materials (Basel). 12 (2019) 2929. doi:10.3390/ma12182929.

CONCLUSIONS

The present contribution was focused on the use of alternative biomaterials with enhanced characteristics for their use in the fabrication of thermally sprayed coatings. The main aim was to develop and analyze the structure, microstructure, and bioactivity of radiopaque BHAp/BG45S5+Bi_2O_3 coatings obtained by thermal spray following the fabrication and properties of the feedstock materials and the gradual deposition of the combined coating. Several conclusions regarding the feedstock powders characteristic, coatings performance and architecture were addressed from this research and are presented as follows:

- Biological Hydroxyapatite (BHAp) was obtained with a proper particle size distribution and remarkable microstructural and structural properties to use it as feedstock for thermal spray coatings fabrication. BHAp presents characteristics of carbonated B type apatite, ($Ca_{10-(x+y)}Mg_y(PO_4)_{6-x}(CO_3)_x(OH)_{2-x}.Mg$). This confers biomimetic properties to the feedstock powder with enhanced bioactivity in comparison with conventional stoichiometric HAp used in the fabrication of coatings by thermal spray.
- Amorphous bioactive glass (BG45S5) was successfully fabricated by using the melt and fast quenching method in two laboratory facilities. This demonstrates that the selected precursors, powders preparation, decarbonization, and heat treatments were properly chosen. The lab-made bioactive glass bioactivity, structural characteristic, oxides composition, and physical and thermal properties, agree with the BG45S configuration. In addition, it is worth mentioning that the amorphous glass fabrication was widely described and understood to propose and explain the effect of the addition of Bi_2O_3 and to compare its effect on thermally sprayed coatings.
- Lab-made BG45S5 samples with different additions of Bi_2O_3 were prepared by melt and fast quenching. The addition aimed to seek the quantity of bismuth oxide that maximizes the radiopacity and maintains the structural and thermal characteristics of the feedstock powders. The radiopacity of the samples was monitored following the norm ISO 13116/2014. The results show that to add 15 - 20 wt. % of Bi_2O_3 to the precursors' mixture during the lab-made BG45S5 fabrication, increases the radiopacity of the glass by 4.5 to 9 times, approximately. Nevertheless, changes in T_c and T_m allows concluding that the obtained BG is modified and crystallized in another type of glass with such quantities. On the other hand, the addition of 10 wt. %, increased the lab-made BG45S5 radiopacity by 2 times compared to previously reported BG45S5 with 20 % of Bi_2O_3 obtained by flame spray

pyrolysis. This quantity increased the BG45S5 radiopacity by 3.6 times, representing slight changes in the thermal properties of the glass and negligent structural changes according to the XRD analysis. Finally, it should be taken into account that the addition of Bi_2O_3 higher than 10 wt. % increases the crystallization tendency of the glass during heat treatments, which can affect the material bioactivity.

- Bovine derived Ca-deficient and mainly B-type 100% HAp powder was deposited by APS and HVOF thermal spray processes leading to thicknesses of 56.6 ± 11.9 µm and 75± 4.7 µm, respectively. Comparing the structure, microstructure and bioactive behavior of the coatings deposited with both processes let to conclude that the crystalline phase of the APS coating surface structure is 100 % HAp. On the contrary, the crystalline phase content of the HVOF coating is composed of HAp (51.25 %) and dolomite (48.75 %) phases. Regarding the Ca/P ratio of this crystalline phase, ratios of 1.48 and 1.42 were measured in the structure of the APS and HVOF coating, respectively. The reduction in the ratio is due to the decomposition of the HAp phase in amorphous calcium phosphate (ACP), dolomite, and Ca-sites substitutions. The formation of the dolomite on HVOF coating was due to (1) the carbonization of the BHAp and (2) the available Mg^{2+} from bovine-derived hydroxyapatite in the feedstock powder.

  According to the bioactivity analysis of the coatings, the characteristic polyhedral structure of the apatite layer was evidenced in both HVOF and APS coatings after 3 days of immersion in simulated body fluid (SBF). Nevertheless, the typical apatite morphology was more evident in APS coating and its crystals were bigger after 5 and 10 days of immersion. However, the grown apatite layer in HVOF coating was delaminated after 5 days followed by the growth of a new apatite layer after 10 days of immersion in SBF.

  After immersion in SBF, the Ca/P ratio in APS coating showed a typical tendency during the growth of the apatite layer. The Ca/P ratio tendency in HVOF coating is similar to APS coating. However, the ratio is lower in all the evaluated days. In addition, the Ca and P uptake is higher in APS coating due to its higher bioactivity compared to HVOF during immersion in SBF. The reduction of Mg in the HAp phase of HVOF caused by the formation of the dolomite phase promotes the Mg uptake during the first days of immersion. The Mg uptake in APS coating starts at the expected time of immersion. Finally, APS thermal spray parameters stand of distance, SOD = 10 cm, current intensity, I = 450 A, and powder feed rate, PFR = 10 g/min were selected as a proper parameter combination to spray gradual coatings of BHAp/BG+10Bi_2O_3 given the lower HAp phase decomposition.

- Lab-made BG45S5+ 10 wt. % Bi_2O_3 feedstock powder was plasma sprayed and its structure, microstructure, and bioactivity were compared with a coating made with commercial BG45S5 powder. From the results, it was concluded that lab-made BG45S5+10 wt.% Bi_2O_3 coating showed similar microstructure and amorphous structure in comparison with the coating plasma-sprayed using commercial BG45S5 feedstock powder without Bi_2O_3. However, BG45S5 +10 wt. % Bi_2O_3 coating showed a lower rate of apatite layer formation, and delamination was observed between 5 and 10 days of immersion in SBF. Hence, Bi_2O_3 delays the formation of the apatite layer in the coating sprayed using lab-made BG45S5 +10 wt. % Bi_2O_3.
- The graded BHAp/BG45S5 + 10 wt. % Bi_2O_3 coating was obtained by the preparation of the feedstock powders mixtures using a mechanical mixing and the plasma spraying of separate layers with a single powder feeder and plasma spray parameters: SOD = 10 cm, I = 450 A and PFR = 10 g/min. The graded coating showed a lower rate of apatite layer formation compared to commercial BG45S5 single coating and a similar rate of apatite layer formation until 5 days compared to single BG45S5+10 wt. % Bi_2O_3 coating. In contrast, the graded coating showed a higher apatite layer formation after 10 days of immersion in SBF compared to single BG45S5 + 10wt % Bi_2O_3 coating. These results show that the graded configuration and the use of the BHAp lead to an increase in the stability of BHAp/BG + 10 wt. % Bi_2O_3 coatings given the detection of no delamination and the apatite formation on the surface of the coating after 10 days of immersion in SBF.